VILNIUS GEDIMINAS TECHNICAL UNIVERSITY

Alexey A TYSHKO

DEVELOPMENT OF NUCLEAR MAGNETIC RESONANCE DOWNHOLE LOGGING TOOL FOR HYDROCARBONES SEARCH

DOCTORAL DISSERTATION

TECHNOLOGICAL SCIENCES,
ELECTRICAL AND ELECTRONIC ENGINEERING (01T)

VGTU
LEIDYKLA
TECHNIKA
Vilnius 2016

Doctoral dissertation was prepared at Vilnius Gediminas Technical University in 2015–2016.

Supervisor

Prof. Dr Habil. Saulius BALEVIČIUS (Vilnius Gediminas Technical University, Electrical and Electronic Engineering – 01T)

The Dissertation Defense Council of Scientific Field of Electrical and Electronic Engineering of Vilnius Gediminas Technical University:

Chairman

Prof. Dr Habil. Romualdas NAVICKAS (Vilnius Gediminas Technical University, Electrical and Electronic Engineering – 01T).

Members:

Prof. Dr Kęstutis ARLAUSKAS (Vilnius University, Physics – 02P),
Prof. Dr Habil. Arturs MEDVIDS (Ryga Technical University, Electrical and Electrical and Electronic Engineering – 01T),
Assoc. Prof. Dr Dainius UDRIS (Vilnius Gediminas Technical University, Electrical and Electronic Engineering – 01T),
Prof. Dr Vytautas URBANAVIČIUS (Vilnius Gediminas Technical University, Electrical and Electronic Engineering – 01T).

The dissertation will be defended at the public meeting of the Dissertation Defense Council of Electrical and Electronic Engineering in the Senate Hall of Vilnius Gediminas Technical University at 1 p. m. on 27 January 2017.

Address: Saulėtekio al. 11, LT-10223 Vilnius, Lithuania.
Tel.: +370 5 274 4956; fax +370 5 270 0112; e-mail: doktor@vgtu.lt

A notification on the intend defending of the dissertation was send on 23 December 2016.

A copy of the doctoral dissertation is available for review at the VGTU repository http://dspace.vgtu.lt/ and at the Library of Vilnius Gediminas Technical University (Saulėtekio al. 14, LT-10223 Vilnius, Lithuania) and Lithuanian Academic Electronic Library ELAB , CPST Saulėtekio al. 3, LT-10223 Vilnius, Lithuania.

VGTU leidyklos TECHNIKA 2402-M mokslo literatūros knyga

ISBN 978-609-457-993-6

© VGTU leidykla TECHNIKA, 2016
© Alexey A. Tyshko, 2016
atyshko01@comcast.net

VILNIAUS GEDIMINO TECHNIKOS UNIVERSITETAS

Alexey A TYSHKO

BRANDUOLINIO MAGNETINIO REZONANSO ĮTAISO ANGLIAVANDENILIŲ ŽVALGAI GILUMINIUOSE GREŽINIUOSE KŪRIMAS

DAKTARO DISERTACIJA

TECHNLOGIJOS MOKSLAI,
ELEKTROS IR ELEKTRONIKOS INŽINERIJA (01T)

VGTU
LEIDYKLA
Vilnius TECHNIKA 2016

Disertacija rengta 2015–2016 metais Vilniaus Gedimino technikos universitete.

Vadovas

prof. habil. dr. Saulius BALEVIČIUS (Vilniaus Gedimino technikos universitetas, elektros ir elektronikos inžinerija – 01T).

Vilniaus Gedimino technikos universiteto Elektros ir elektronikos inžinerijos mokslo krypties disertacijos gynimo taryba:

Pirmininkas

prof. habil. dr. Romualdas NAVICKAS (Vilniaus Gedimino technikos universitetas, elektros ir elektronikos inžinerija – 01T).

Nariai:

prof. dr. Kęstutis ARLAUSKAS (Vilniaus universitetas, fizika – 02P),
prof. habil. dr. Arturs MEDVIDS (Rygos technikos universitas, elektros ir elektronikos inžinerija – 01T),
doc. dr. Dainius UDRIS (Vilniaus Gedimino technikos universitetas, elektros ir elektronikos inžinerija – 01T),
prof. dr. Vytautas URBANAVIČIUS (Vilniaus Gedimino technikos universitetas, elektros ir elektronikos inžinerija – 01T).

Disertacija bus ginama viešame Elektros ir elektronikos inžinerijos mokslo krypties disertacijos gynimo tarybos posėdyje 2017 m. sausio 27 d. 13 val. Vilniaus Gedimino technikos universiteto senato posėdžių salėje.

Adresas: Saulėtekio al. 11, LT-10223 Vilnius, Lietuva.
Tel.: (8 5) 274 4956; faksas (8 5) 270 0112; el. paštas doktor@vgtu.lt

Pranešimai apie numatomą ginti disertaciją išsiųsti 2016 m. gruodžio 23 d.

Disertaciją galima peržiūrėti VGTU talpykloje http://dspace.vgtu.lt/ ir Vilniaus Gedimino technikos universiteto bibliotekoje (Saulėtekio al. 14, LT-10223 Vilnius, Lietuva) ir Lietuvos akademinėje virtualioje bibliotekoje, FTMC, (Saulėtekio al. 3, LT-10223 Vilnius, Lietuva).

Abstract

This thesis presents a new development in the design of Nuclear Magnetic Resonance (NMR) downhole logging tools for the oil and gas industry and operates in a high temperature environment. Two main improvements of this tool is suggested and analyzed in this thesis. They are a new NMR antenna containing a Faraday shield placed between the antenna coil and the analyzed fluid and an improved NMR transmitter operating at 175 °C ambient temperature. This is based on multi-module, multilevel topology, which combines the outputs of several identical power modules, which operate at a 50% duty cycle at its fundamental frequency.

The NMR antenna equipped with Faraday shield decreases the resonant frequency shift to less than 1%, which makes it possible to perform measurements without engaging a special tuning system for the compensation of antenna detuning. It was shown experimentally that the implementation of the Faraday shield makes the NMR echo signal less dependant on the type of the well fluid being measured. For the multi-module NMR transmitter, a method of DC/AC conversion based on the multi-vector synthesis of the sinusoidal voltage with sequential elimination of the higher harmonics in the output voltage was used. This was done in order to decrease the power dissipation occurring in the resonant loads.

The present study reevaluates the prior investigations of a silicon MOSFET's drain-to-source resistance (R_{dson}) in a temperature range of up to 200 °C as a function of the temperature and the drain current (I_d). An improved R_{dson} behavioral model in which R_{dson} and power index (P) of R_{dson} dependence on the temperature proposed as a function of I_d was tested and validated for the temperature range from 25 °C to 200 °C.

The multilayer X7R type capacitors, used as the high power NMR transmitter's filters, were investigated for excessive losses and ways to mitigate these losses were suggested. It was demonstrated that these capacitors behave as piezoelectric resonators when biased with DC voltage and that their mechanical resonances increase the capacitors' losses and propability of failure.

The multimodule NMR transmitter, which uses a combination of the fixed phase shift method for the cancellation of the higher harmonics an increase of the NMR tool signal to noise ratio and NMR transmitter life expectancy. The higher harmonics cancelation in the multimodule NMR transmitter was validated experimentally by testing transmitters with different topologies.

Reziumė

Šiame darbe pateikiamas naujas branduolinio magnetinio rezonanso (BMR) įtaisas, skirtas giluminei naftos ir dujų paieškai, veikiantis aukštose temperatūrose. Pasiūlyti ir išanalizuoti du pagrindiniai šio įtaiso patobulinimai. Tai – nauja BMR antena, sudaryta iš Faradėjaus ekrano, sumontuoto tarp antenos ritės ir analizuojamos aplinkos, ir BMR siųstuvo DC/AC keitiklis, veikiantis iki 175 °C aplinkos temperatūros. Šis keitiklis turi daugelio modulių topologiją, kuri sujungia keletą identiškų maitinimo modulių, veikiančių 50% darbo ciklu nuo savo pagrindinės dažnių harmonikos.

Faradėjaus ekranas, įrengtas BMR antenoje, sumažina rezonansinio dažnio pokytį iki 1 %, todėl matavimus galima atlikti, nenaudojant specialios derinimo sistemos, atliekančios šios antenos išsiderinimo kompensaciją. Eksperimentiškai buvo parodyta, kad Faradėjaus ekrano panaudojimas daro BMR atsako signalą mažiau priklausomą nuo gręžinio aplinkos elektrinių savybių. Tobulinant daugelio modulių BMR siųstuvo keitiklį, buvo naudojama kelių sinusoidinės įtampos vektorių sintezė, leidžianti panaikinti išėjimo įtampos aukštesniasias harmonikas. Tai buvo atlikta, siekiant sumažinti energiją, išsiskiriančią įtaiso rezonansinėje apkrovoje.

Tyrimai, atlikti šiame darbe, leido iš naujo įvertinti silicio MOSFET tranzistorių santakos-ištakos varžos (R_{dson}) jautrumą temperatūros pokyčiams aukštose (iki 200 °C) temperatūrose ir ištakos srovės (I_d) vertei. Pasiūlyta nauja empyrinė R_{dson} priklausomybė nuo temperatūros (intervale nuo 25 °C iki 200 °C), kurioje įskaityta jog R_{dson} ir šios priklausomybės laipsninės funkcijos indeksas (P) priklauso nuo I_d.

Ištirti daugiasluoksnių X7R tipo kondensatorių, naudojamų galingų BMR siustuvų filtruose, elektriniai nuostoliai ir pasiūlyti būdai, kaip šiuos nuostolius sušvelninti. Buvo parodyta, kad X7R tipo kondensatoriai elgiasi kaip pjezoelektriniai rezonatoriai, jeigu prie jų yra prijungiama pastovi įtampa. Šis mechaninis rezonansas padidina kondensatorių suirimo tikimybę.

Daugelio modulių BMR siųstuvo keitiklis, kuris naudoja fiksuoto fazės poslinkio metodą, sumažinantį aukštesnių harmonikų įtaką išėjimo signalui, leidžia padidinti signal-triukšmo santykį ir BMR įtaso darbo trukmę. Aukštesniųjų harmonikų įtakos sumažinimo galimybė daugelio modulių BMR siųstuvo keitiklyje buvo patvirtinta eksperimentiškai, tiriant įvairių topologijų BMR siųstuvus.

Notations

Symbols

α_{m} – is a total phase shift of module number *m*;
α_{n} – is a phase shift angle needed to cancel harmonic number *n*;
A_{cm2} – is the surface area in cm sq. of the component;
B_0 – is the induction of the permanent magnet in the sensitive area;
B_1 – is the high frequency magnetic field used for proton tipping;
c_{m} – is the binary code assigned to module m, it equals module number m minus one;
E_{A} – is the apparent activation energy;
f_{L} – is the Larmor frequency;
γ – is the gyromagnetic parameter;
I_{d} – is the value of the drain current;
I_{n} – is the value of the current of harmonic number *n*;
I_{t} – is the value of the test current;
k – is Boltzmann's constant;
K_{r} – is the ratio of R_{dson} measured at 150°C to R_{dson} measured at 25°C;
M_0 – is the magnetic moment of the polarized protons in sensitive volume;
M_{r} – is the normalized drain current;
m – is the module number in the multimodule transmitter;
n – is the number of the harmonic;
N_{e} – is the number of experiments used for statistical averaging;
P_{d} – is the power index in expression of R_{dson};
P_{noise} – is the power of the noise in NMR receiver;
P_{mW} – is the power in mW dissipated by componenet;
P_{signal} – is the power of echo signal in the NMR receiver;

P_{sw} – is the power dissipated in MOSFET switch of the NMR transmitter due to conduction losses;
P_r – is power in K_r *vs*. maximum drain voltage rating dependence;
P_t – is the total porosity;
R_{dson} – is the MOSFET drain-to-source resistance;
R_{th} – is thermal resistance K/W;
τ_0 – is the duration of the tipping pulse;
t_v – is the expected lifetme;
θ – is the resulting tipping angle at the end of the tipping pulse;
T_1 – is the longitudinal relaxation time;
T_2 – is the transverse relaxation time;
T_{Hann} – is the duration of the Hann pulse;
T_A – is the ambient temperature;
T_j – is the MOSFET junction temperature;
Q – is the quality factor of the antenna resonant tank;
V_a – is the antenna peak voltage;
V_b – is the bulk volume;
V_d – is the drain-to-source voltage drop;
V_g – is the grain volume;
V_B – is the bus voltage of the transmitter power modules;
V_{md} – is the MOSFET maximum drain voltage rating;
$V_{1,k}$ – is the value of the fundamental harmonic after cancelling of first *k* higher harmonics;
V_n – is the amplitude of harmonic number *n*;
$\vec{V}_{lag}$ – is the lagging vector;
$\vec{V}_{lead}$ – is the leading vector;
$\vec{V}_{out}$ – is the combined;
φ – is a variable angle between leading and lagging vectors;
φ_{ref} – is phase shift between the reference and resulting output signal;
Φ_n – is the vector array phase shifts.

Abbreviations

ADC – Analog-to-Digital Converter;
AF – Accelerator Factor;
CPMG – Carr-Purcell-Meiboom-Gill series of 90 deg tipping and 180 deg refocusing pulses used in spin-echo NMR;
DC/AC – Direct Current to Alternating Current;
EMI – Electromagnetic Interference;

ESR – Equivalent Series Resistance characterizing total losses in the capacitors;
FID – Free Induction Decay;
FFT – Fast Fourier Transform;
LTSpice – Linear Technology electrical schematic simulation software;
LWD – logging while drilling
MOSFET – Metal Oxide Field Effect Transistor;
NMR – Nuclear Magnetic Resonance;
PAPS – Phase Alternative Pulse Sequence;
PWM – Pulse-Width Modulation;
RMS – Root-mean-square, effective value of voltage or current;
SP-PWM – Phase-Shift Pulse Width Modulation;
TE – time between refocusing 180° (π) pulses in CPMG series;
TW – the polarization time;
ZVS – zero voltage switching;
X7R – type of ceramic used for multilayer capacitors widely used for filters.

Contents

INTRODUCTION 1
Problem Formulation 1
Importance of the Thesis 2
The Object of Research 3
The Aim of the Thesis 3
The Tasks of the Thesis 3
Research Methodology 4
Scientific Novelty 4
Practical Significance of Achieved Results 5
The Defended Statements 5
Approval of the Results 6
Structure of the Dissertation 6

1. LITERATURE SURVEY ON NUCLEAR MAGNETIC RESONANCE OIL AND GAS WELL LOGGING TOOLS 9
1.1. Hydrocarbon Exploration and Reservoir Evaluation 9
1.2. Nuclear Magnetic Resonance Technology 11
1.2.1. Nuclear Magnetic Resonance Basics 12
1.2.2. Nuclear Magnetic Resonance Pulse Sequences 14
1.2.3. Nuclear Magnetic Resonance Signal Processing 15
1.2.4. Nuclear Magnetic Resonance Results Interpretation 16

1.3. Nuclear Magnetic Resonance Tool Block Diagram and Operation 17
1.4. Nuclear Magnetic Resonance Tool Antenna 19
1.4.1. External Field Antenna 20
1.4.2. Internal Field Antenna 22
1.5. Nuclear Magnetic Resonance Transmitter 25
1.5.1. Switch Mode Transmitter Harmonics 27
1.5.2. Power Transistors 30
1.5.3. Capacitors 33
1.6. Conclusions of Chapter 1 and Formulating Tasks for the Dissertation 36

2. IMPROVEMENT OF THE INTERNAL NUCLEAR MAGETIC RESONANCE ANTENNA THROUGH THE USE OF A FARADAY SHIELD 37
2.1. The Effects of Well Fluid on the Nuclear Magnetic Resonance Antenna Resonant Frequency 37
2.2. The Internal Nuclear magnetic Resonance Antenna with a Faraday Shield 40
2.3. Conclusions of Chapter 2 46

3.SILICON MOSFET DRAIN-TO-SOURCE RESISTANCE BEHAVIOR AT HIGH TEMPERATURES 47
3.1. Correlation Between Drain Voltage Rating Value and Drain Resistance Temperature Coefficient 48
3.2. Silicon MOSFET Experimental Test Setup 49
3.3. Silicon MOSFET Test Results 51
3.4. Conclusions of Chapter 3 55

4. INVESTIGATION OF X7R CERAMIC CAPACITORS 57
4.1. Setup for the Investigation of X7R Capacitors' Eqivalent Series Resistance 57
4.2. Eqivalent Series Resistance Dependence on the DC Bias 59
4.3. Conclusions of Chapter 4 62

5. NUCLEAR MAGNETIC RESONANCE TRANSMITTER WITH CANCELLED HIGHER HARMONICS 63
5.1. The Multimodule Topology of the Nuclear Magnetic Resonance Transmitter 64
5.2. Spectrum of the Output Current 72
5.3. Signal to Noise Ratio Improvement by Decreasing the Per Pulse Energy Consumption 74
5.4. Increasing of Nuclear Magnetic Resonance Transmitter Life Expectancy 75
5.5. Test and Evaluation of Transmitter with the Cancelled Third Harmonic 78
5.6. Conclusions of Chapter 5 84

GENERAL CONCLUSIONS 87

REFERENCES 91

LIST OF PUBLICATIONS BY THE AUTHOR ON THE TOPIC OF THE DISSERTATION 97

SUMMARY IN LITHUANIAN 99

ANNEXES[1] 115
Annex A. Agreement of co-authors to provide published material in the doctoral dissertation 117
Annex B. Copies of scientific publications by the autor on the topic of the dissertation 119

[1]The annexes are supplied in the enclosed compact disc

Introduction

Problem Formulation

The depletion of shallow light oil and gas land deposits as well as increased consumption of these valuable energy resources has led to higher prices on the world market, despite the fluctuations that are motivated by political factors. The present intention of replacing fossil fuels with reneweables is facing difficulties, however. Thus the sharp increase of the cost of drilling, especially from platforms at sea and from special ships, requires an increase of the drilling speed as well as the speed and accuracy of the measurements taken of the parameters of perspective oil/gas fields, which is called “well logging”. The main task of such “logging” is to determine the presence and locations of hydrocarbons and their characteristics such as viscosity and rock formation porosity. This is used for the evaluation of the total field, the determination of the extractible oil/gas deposits and the expected productivity of such wells. The classic method of evaluating rock formation samples makes sense only in exceptional cases because of their lengthy retrieval process and resulting high cost. Therefore, the use of indirect, mainly electro-physical methods, which are more reliable and accurate, is preferred.

Significant advances have been made recently in application of Nuclear Magnetic Resonance (NMR) technology for the exploration and evaluation of oil

and gas fields. These NMR downhole logging tools are capable of detecting and differentiating formation fluids, such as free water and oil. They can also differentiate gas from oil in hydrocarbon bearing reservoirs. This method is useful when other methods fail to give complete answers. However, the application of NMR technology requires the development of unique power electronic devices able to operate at high ambient (up to +175 °C) temperatures and at pressures over 2,000 atm in formations having a wide range of electrical properties. For this reason, there is a need for a tool capable of performing direct, continuous flow downhole NMR measurements, which can be used to enhance the quality and reliability of the formation evaluations, that previously had been obtained using other techniques.

Importance of the Thesis

Usually the NMR tools used for well logging operate within a gradient field. This means that the volume which responds to the antenna excitation at Larmor frequency is only a thin layer inside the formation. With an increase of temperature, the magnet flux of permanent magnets decreases and corresponding Larmor frequency layer simply moves closer to the magnet. As a result, the total volume being registered by spin-echo NMR signal is very small. In order to increase this volume, it has been suggested that the fluid samples passing through the central dielectric tube surrounded by the strong permanent magnet, which creates a homogeneous field in the tube, be analyzed. As the homogeneous permanent field and proper antenna would be able to excite the whole volume of the sample, this would provide a significantly higher signal to noise ratio and thus increased accuracy. In such case, however, changes in the electrical parameters of formation can unpredictably affect the tuning of the RF antenna, which needs to be in resonance with the spin-echo NMR signal. For this reason, it is necessary to use special means in order to compensate for the detuning of the antenna.

A very important part of such NMR downhole logging tools is a transmitter, which is high frequency DC to AC converter loaded with a resonant NMR antenna. Due to the harsh conditions (high temperature and pressure) that are experienced, the increased power dissipation in the transmitter itself and the limited heatsinking capabilities of the high-pressure housing in which it needs to be mounted, all these add significant challenges for developers of such NMR transmitters. The temperature increase of the power components (mainly MOSFET transistors) decreases their lifetime expectancy and total tool reliability. Moreover, this also affects the accuracy of the tool because the increase of

the per-pulse energy depletes capacitive energy storage faster and decreases the maximum number of the tests that are achievable.

In the present work, it is suggested that the detuning effect of RF antenna be limited by means of the Faraday shield placed between the antenna coil and the sample fluid. This makes it possible to minimize the deviation of the antenna loss factor and the resonant frequency. The removal of the higher harmonics from the output current of the DC/AC converter my means of special topologies and control methods enables a decrease of the power dissipation in the NMR transmitter and an increase of the tool's life expectancy. As a result, a breakthrough technology capable of delivering important information as to the characteristics of the fluids present in the well under real well conditions and in real time has been developed.

The Object of Research

The object of the research described in the present work is the antenna and the DC/AC converter used in the construction of the NMR downhole logging tool used for the determination of the presence, location and characteristics of hydrocarbons in deep wells.

The Aim of the Thesis

The main aim of the present work is to investigate ways for improving the NMR downhole logging tool antena and its DC/AC converter in order to increase the accuracy and operational life of this tool.

The Tasks of the Thesis

In order to achieve the objective, the following problems had to be solved:

1. To review techniques used for the search of hydrogen containing materials (hydrocarbons and water) based on the Nuclear Magnetic Resonance (NMR) method.
2. To investigate the possibilities of using the Faraday shield between the internal NMR tool antenna coil and the formation fluid in order to limit the effects of any variations of the fluid parameters on the NMR antenna resonant frequency.

3. To investigate the sensitivity of drain-source resistance to changes of temperature of high voltage (600V to 900V rated) silicon MOSFETs along a range of temperatures up to 200°C.
4. To investigate the behaviour of the X7R ceramic capacitors used in NMR oil and gas well logging tools as transmitter filters under DC bias due to their unexpected overheating and failure in such high current regime.
5. To investigate how the cancellation of the higher harmonics in the multimodule transmitters used in NMR oil and gas well logging tools enables an increase of their life expectancy and accuracy.

Research Methodology

To investigate the *object*, the following *research methods* are chosen:

- Theoretical analysis of the multimodule NMR transmitter, which employs the Chireix-Doherty outphasing principle for amplitude control, Fast Fourier Transform analysis of the module's output voltage and current harmonics using LTSpice software.
- Experimental investigation of the sensitivity of the drain-source resistance to temperature of high voltage (600V to 900V rated) silicon MOSFETs and of higher harmonic cancellation in multi-module NMR transmitters.

Scientific Novelty

The scientific novelty aspects of the theoretical and experimental investigation of a NMR antenna mounted with a Faraday shield and a multi-module NMR transmitter are as follows:

1. It was first time demonstrated that instalation of Faraday shield, placed between the solenoid and the formation fluid, in NMR oil and gas well logging tool produces a significantly higher stability of the antenna resonance frequency and the quality factor and is less subject to changes of the conductivity and permeability of the fluid being analized. This decreases the dimensions of the tool enables it to perform in-citu laboratory analysis of the fluids contained in the rock formations of deep wells.
2. The new multimodule, multilevel topology of the DC/AC converter, which combines outputs of several identical power modules, opera-

ting with 50% duty cycle at the fundamental frequency, provides the-cancellation of the higher harmonics and improves the life time and accuracy of NMR well logging tools operating at 175°C.

Practical Significance of Achieved Results

The investigations presented in this thesis were developed as part of the leading edge technologies which were successfully created and implemented in the production tools by the Halliburton Energy Services Company. They allowed it to sign a three year, $400 million total value contract with BP (British Petroleum) in 2003 to provide it with products and services for its exploration and drilling activities in the Gulf of Mexico and the lower 48 states.

Halliburton L&P's MRILab(TM) tool utilizes this Nuclear Magnetic Resonance technology to continuously monitor the level of filtrate contamination in the fluid being extracted in order to minimize the time required to obtain a clean sample. Information from the MRILab tool is further used to provide important fluid parameters such as the hydrogen density, fluid viscosity and gas/oil ratio (GOR) as well as to enhance the formation evaluation provided by the MRIL-Prime(TM) logging tool (Halliburton, 2003).

The investigation results and practical solutions have being patented: „Magnetic Resonance Fluid Analysis Apparatus and Method" US6737864, US716426, EP1393096 incorporate Faraday shield in the NMR antenna and „Enhanced Transmitter and Method for a Nuclear Magnetic Resonance Logging Tool" US9405035 as well as „Multi-Vector Outphasing DC to AC Converter and method" US 20160301327, 04 14, 2014. Patent Application was intended for higher harmonics cancellation in output of NMR tramsmitter.

The Defended Statements

The following statements based on the results of present investigation may serve as the official hypotheses to be defended:

1. The Faraday shield, placed between the Nuclear Magnetic Resonance (NMR) antenna coil and fluid sample, decreases the resonant frequency shift up to the level (no more than 1%) which allows the NMR oil and gas well logging tool to operate without the special system used for the compensation of the detuning of the antenna resonant frequency.
2. The empirical expression of high voltage silicon MOSFET transistors drain-to-source resistance dependence on temperature, in which

the influence of drain current is taken into consideration, correctly describes (with correlation coefficient 0.991–0.999) the behaviour of silicon MOSFET in the temperature range from 25 °C to 200 °C.

3. Biasing of X7R capacitors, which are widely used in NMR oil and gas well logging tools transmitter as filters, by DC voltage increases the capacitor‘s Equivalent Series Resistance value (16 times at 100V) due to piezoelectric resonance effect. It increases power losses and probability of X7R capacitors failure.
4. The multimodule transmitter of NMR oil and gas well logging tool, based on silicon MOSFETs, which uses a combination of the fixed phase shift and outphasing methods, allows the generation of output voltage without higher harmonics. An increase of the number of modules from 2 to 8 increases the transmitter‘s life expectancy from 4 year to 10 year. It also in 20% increases the signal to noise ratio of the NMR tool.

Approval of the Results

The author has made 5 articles in scientific journals, 3 presentations at 3 international scientific conferences and 5 patents:

- The IEEE 34th International Conference, Electronics and Nanotechnology (ELNANO), *Multi-Vector Outphasing Provides High Power, Low Harmonics.* [ed.] IEEE Digital Library ELNANO-2014. Kiev, Ukraine .
- The IEEE 35th International Conference, Electronics and Nanotechnology (ELNANO), *DC to AC 3 Phase Modular Multilevel Conversion Using Chireix Outphasing Method.* Kiev, Ukraine 2015.
- The IEEE 36th International Conference on Electronics and Nanotechnology (ELNANO), *Specifics of the X7R Capacitors Application in the High Frequency Inverters.* Kiev, Ukraine 2016.

Structure of the Dissertation

The dissertation is structured around five main chapters.

Chapter 1 reviews the Nuclear Magnetic Resonance (NMR) method, used for the search for hydrogen containing materials (hydrocarbons and water), the processing of the NMR signal and the interpretation of the measurement results. It also presents the block diagram and operation of a typical well logging NMR

tool, the NMR antenna and the transmitter. In this chapter, the main problems related to the reliability of high voltage silicon MOSFET transistors and X7R ceramic capacitors are discussed.

Chapter 2 provides the results of the research on the effects of the well fluid on the internal NMR antenna's resonant frequency, and a method for improving the stability of the antenna resonant frequency by the implementation of a slotted Faraday shield between the antenna coil and the well fluid.

Chapter 3 presents the experimental investigation of the drain-to-source resistance, which defines the conductive losses of the high voltage silicon MOSFET transistors in a temperature range up to 200°C as a function of temperature and drain current.

Chapter 4 presents the investigation of multilayer X7R capacitors, used in the high power NMR transmitters as filters. For this purpose, the capacitor Equivalent Series Resistance *vs*. the DC bias dependence was investigated along a voltage range from 0V to 100V when the frequency changes up to 0.1 MHz at maximum capacitor voltage rating. Ways of mitigating excessive losses in these capacitors are also discussed.

Chapter 5 describes the design of the new NMR transmitter, operating at 175 °C ambient temperature. Its multi-module, multilevel topology, which combines the outputs of several identical power modules, operating at a 50% duty cycle at fundamental frequency, provides the versatility needed for both low harmonic sine voltage synthesis and amplitude control. Cancellation of the higher harmonics of the output voltage is achieved by creating fixed relative phase shifts between the individual modules of the multi-module converter. The amplitude control employs the Chireix-Doherty outphasing modulation principle. The possibilities of a 20% increase of the tool signal to noise ratio (SNR), as compared to that of a two-module transmitter, as well as the significant increase of the tool's life expectancy is demonstrated in this chapter.

General conclusions as well as recommendations for further research complete the present study. These are followed by an extensive list of references and a list of 13 publications by the author on the topic of this dissertation.

1

Literature Survey on Nuclear Magnetic Resonance oil and gas well logging tools

This Chapter reviews material on Nuclear Magnetic Resonance (NMR) method, used for hydrogen containing materials (hydrocarbons and water) search, NMR signal processing and interpretation of the measurement results. It also presents the operation of the typical well logging NMR tool, NMR antenna and transmitter. The main problems related with reliability of high voltage silicon MOSFET transistors and X7R ceramic capacitors are also discussed in this chapter.

1.1. Hydrocarbon Exploration and Reservoir Evaluation

The most versatile fossil fuels are hydrocarbons. Oil and gas deposits not only provide fuel for energy production and transportation, but also raw materials for chemical industries producing plastics, fertilizers and other products. Despite the high volatility of prices on the international market in which the mechanisms of

supply and demand are subjected to immense political pressure, hydrocarbon production continues to increase. In 2015, more than 96 million barrels of oil per day were produced (Mills, 2012; Total, 2015; Energy, 2014; Oil, 2014). Although a predicted switch to renewable sources is predicted, this faces innumerable problems unless more reliable energy storage technology is created (Trainer, 2014).

Most new deposits of oil and gas are found on ocean bottoms and ocean shelfs, which makes their search and development extremely expensive (Clanton, 2010; Nurmi, *et al*. 1997) The platforms and ships that are used for this purposes cost hundreds of millions US dollars and the costs of access to such wells for purposes of drilling and "logging" can sometimes exceed $1M per day. This makes the old, but most reliable petrophysical methods used for of the evaluation of hydrocarbon bearing formation, based on the extraction of test samples, simply unaffordable.

Modern geophysical methods use sensors based on multiple physical principles to "log" wells. This is done by remote means to obtain information as to the presence of hydrocarbons in the formation (Nurmi, et at. 1997; Aki, 2012; Bloch, 1946; Coates, et. al. 1999). Thus when one run of a tool string containing several sensors is made over a perspective rock formation; this provides a complete description of the well. This is called a well "log", which contains reliable data as to the type of formations that exist at different depths and the characteristics of the fluids present in them.

In order to evaluate an oil or gas field and thus to make a correct business decision as to its productivity, the following information has to be obtained using such logging tools: 1) whether the pore (liquid deposit) in the formation contains water or hydrocarbons, 2) if it is hydrocarbons, is it oil or gas, 3) how much of such hydrocarbons by volume does the reservoir contain and where it is (precise depth and location, 4) what type of rock makes up the formation and what are its properties. Based on such data obtained from a few pilot wells and the results of other geological surveys, the oilfield (gas field) can be properly evaluated for commercial development. Since only one third of the oil (gas) present in any such formation is recoverable without the use of special enhancing methods which greatly increase the costs of production, the accuracy of such assesments is important, as a one percent error in measurement of the formation's porosity can create a several percent error when estimating the total production that can be recovered from such a formation.

Modern logging tools use indirect methods for the evaluation of such oil deposits. These measure the electrical resistivity of these formations, the acoustical wave propagation velocities inherent to them, their natural radioactivity and neutron scattering, their chemical composition pecular as determined by means of Gamma spectrometers, as well as their optical properties, pressures and tem-

peratures. As none of these methods and tools used alone can provide direct answers as to the types of fluid contained in such formations, the total porosity within the formation, the distribution of its porosity and the fluid viscosity of the deposits in such formations, geologists have had to rely on the extensive databases that had been obtained when "logging" similar formations using the above mentioned tools, which had then been verified by physically analyzing rock samples obtained through the process of drilling test wells. The final evaluations are thus usually grounded on searches for the similarity of various combinations of multiple parameters contained in well logs indicating the presence of hydrocarbons and the data obtained for the formation being analyzed. This data is then used to describe the reservoir.

New tools thus need to enhance such searches. One of these is the Nuclear Magnetic Resonance (NMR) tool which is able to provide all those answers even when used alone. Its uniqueness is that it detects only the hydrogen in the free liquid or gas and it does not measure any of the hydrogen contained in formation solids (Nurmi, *et al*. 1997). This is done by measuring the relaxation time of the spin-echo signal. Thus the total amount of hydrogen contained in the formation pores (liquid deposits) can determined, the types of fluids contained (gas, oil or water), the pore sizes (deposit sizes) and their distribution in the formation, also the viscosity of the fluid present. The latter parameters are important for estimating the productivity of the well.

1.2. Nuclear Magnetic Resonance Technology

The Nuclear Magnetic Resonance (NMR) method used for the search of hydrogen containing materials (hydrocarbons and water) is based on the gyromagnetic properties of the hydrogen nuclei. The capability of the protons to react to an applied magnetic field when they are in a gas or liquid media (oil or water) makes it possible to measure only the hydrogen based fluids which can be removed (Aki, 2012; Kenyon, *et al.* 1995).

Some elements such as hydrogen, carbon or sodium have nuclei which have uncompensated spins. These nuclei can be considered as small rotating magnets, which are chaotically oriented in the absence of an external magnetic field (Fig. 1.1) As the hydrogen nuclei have only one proton and relatively large magnetic moments compared to other elements, their presence can thus be detected using the pulse-echo method (Coates*, et al*. 1999).

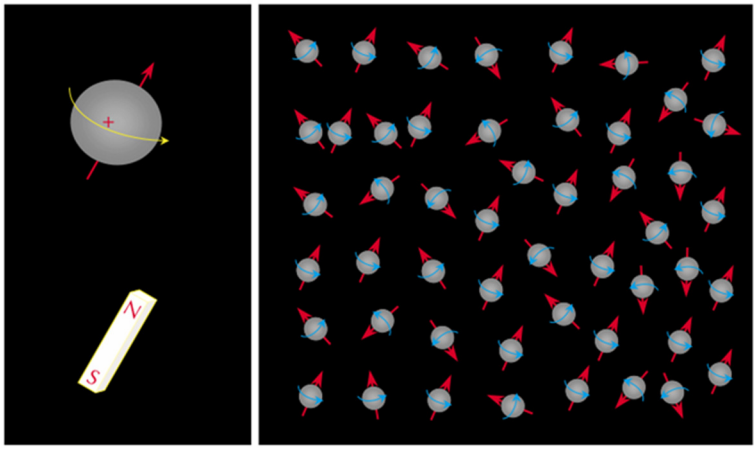

Fig. 1.1. The proton as a rotating magnet. The protons' chaotic orientation in the absence of an external magnetic field (Coates, *et al.* 1999)

1.2.1. Nuclear Magnetic Resonance Basics

The NMR tool operates in the following manner: the nuclei are first aligned by a strong magnetic field and are then perturbed out of alignment by an additional magnetic field directed perpendicular to the primary field which had been used for their original alignment. As the misaligned nuclei then precess in the field, this causes a small return signal to appear which can then be detected. This signal provides information as to the nuclear environment existing in the formation, which can be used for the search of the hydrogen nuclei present in it.

When an external magnetic field having induction B_0 is applied to a material in a gaseous or liquid state containing hydrogen (see Fig. 1.1), the chaotically oriented magnetic moments of the hydrogen protons begin to rotate slowly, thus changing their orientation to that of the magnetic field. This precession frequency, called the Larmor frequency (f_L), is proportional to the proton gyromagnetic parameter γ and B_0 and is described by the following equation:

$$f_L = \frac{\gamma B_0}{2\pi} \tag{1.1}$$

Here the parameter $\gamma = e \cdot g/2m$, e is the particle charge, g is the unitless proportionality factor related to the angular momentum of the system's intrinsic magnetic moment and m is mass of the particle. The f_L is different for different nuclei as it depends on the mass of the particle. For hydrogen nuclei (protons), f_L is 42.58 MHz/Tesla.

In a magnetic field sample of protons in a state of thermal equilibrium, the sample contains more protons spinning in a lower energy (spin-up) state. The ratio of the number of protons in the higher energy state (N_-) to the lower energy state (N_+) is $N_-/N_+ = \exp(-\Delta E/kT)$, where k is the Boltzmann constant and $\Delta E = \hbar\omega_0$ ($\omega_0 = 2\pi \cdot f_L$) is the energy difference between the spin-up and spin-down states. The difference between the number of protons in these states results in equilibrium magnetization M_0 of the total proton assamble in the direction of B_0. The process in which all the nuclear magnetic moments become orientated along the external magnetic field and thus create magnetic moment M_0 is called polarization.

If the pulse of a magnetic field oscillating with Larmor precession frequency f_L is then oriented perpendicular to the direction of B_0 onto a sample with M_0 magnetization, the magnetic moments of the protons are tipped to some angle θ (Coates, *et al.* 1999):

$$\theta = \gamma B_1 \tau_0 \tag{1.2}$$

where B_1 is the amplitude of the magnetic pulse and τ_0 is the pulse duration. The application of B_1 forces the protons to precess in phase with one another. As M_0 precesses, its dipole field precesses with it. This precession can be detected as an alternating voltage being induced in the receiver coil surrounding the sample. In some apparatuses, the drive coil is made separate from the receiver coil used to detect this Larmor precession. There are apparatuses, however, in which one coil is used to perform both functions. In them, the B_1 field perpendicular to B_0 is created by a special coil (antenna), which is excited by a high power RF transmitter. The tip angle θ which results is proportional to the amplitude B_1 and duration τ_0 of the magnetic pulse.

After the application of the magnetic pulse which causes the tipping of M_0 at $\theta = 90°$ angle (also named $\pi/2$) and the transfer of its energy into tipping, the protons are caused to process in phase in transverse planes (relative to B_0), thereby losing their energy and phase stability. This decreases the total magnetization, which then consists of two magnetization vectors: the longitudinal and the transverse. The relaxation of the nuclei population to the thermodynamic state in the magnet is called, "spin-lattice" or *longitudinal relaxation*. During this process, which has characteristic time T_1, the longitudinal magnetization vector grows to M_0. T_1 refers to the mean time it takes for an individual nucleus to return to its thermal equilibrium state of spin. In the contrary case, the transverse magnetic moment component decreases, thereby returning the net magnetization vector to that of a non-precessing field. This is called T_2 or *transverse relaxation*. Because of the difference in the actual relaxation mecha-

nisms that are involved, T_1 is usually longer than T_2. This decrease of magnetization is measured in the traverse direction by the receiver coil which had been used previously as the transmitter coil, but which is now used to detect the decaying signal. This decay is usually exponential and is called Free Induction Decay (FID). The FID time constant is very short and is only a few tenths of ms (Coates, et al. 1999). The main reason for the resultant decay is the magnetic field inhomogeneity which causes defocusing when the nuclei move (diffuse) to another layer with different B_0 and the energy losses due to their collisions with other atoms or the surfaces of solid boundaries.

1.2.2. Nuclear Magnetic Resonance Pulse Sequences

The proton magnetization vector can be refocused in the transverse plane when a $\theta = 180°$ pulse is applied (Figure 1.2). The additional angle speeds up the return of the magnetic moments back to the original alignment and at some moment τ, the amplitude of the detected signal, called the spin echo, reaches maximum. Another $\theta = 180°$ pulse is then needed to refocus protons. The time between the refocusing pulses is 2τ (Coates, *et al*. 1999). Figure 1.3 shows a typical series of refocusing 180° pulses, known as Carr-Purcell-Meiboom-Gill (CPMG) sequences, separated by time TE, the so-called pulse train, which is used to obtain a small, but measurable spin-echo train echo with maximum amplitude somewhere near the center of the refocusing pulses. The blue line shows the amplitude of the received signals of the spin-echo train proportional to the transverse magnetization, which is decaying at time constant T_2.

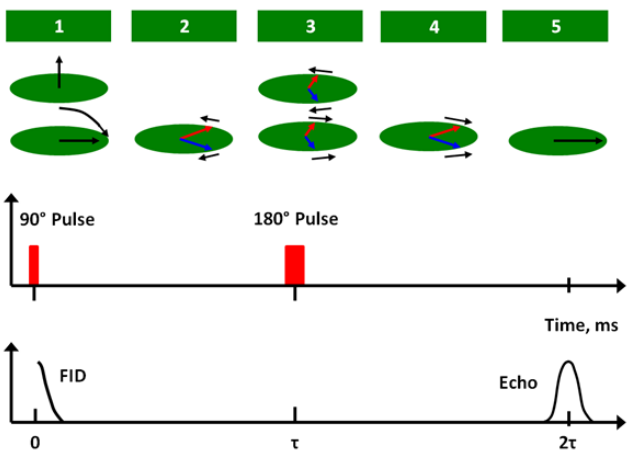

Fig. 1.2. Refocusing pulses and resulting spin echo signal (Coates, *et al*. 1999)

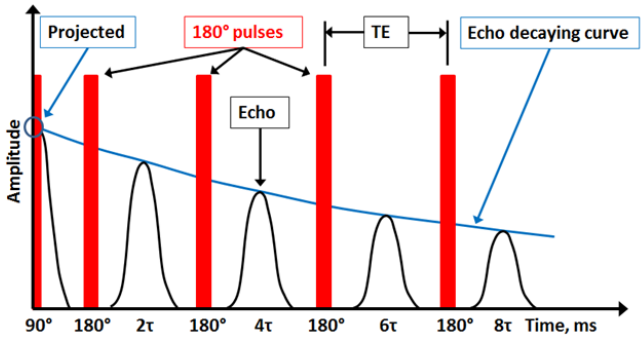

Fig. 1.3. Refocusing pulses and the decaying echo signal (Coates, *et al*. 1999)

After multiple refocusing pulses are received, the echo signals finally decay to noise level and the measurement process stops to allow the B_0 static field to restore polarization to the maximum value M_0. The amplitude of the received echo signals, measured between the refocusing pulses, is used for the calculation of the density of the hydrogen in the pores (liquid deposits) of the rock formation. This is based on the projected starting point of the Echo decaying curve, as shown in Figure 1.3. The dynamics of the echo pulses' amplitude decay also contains information as to the structure and the pore size distribution in the rock formation.

1.2.3. Nuclear Magnetic Resonance Signal Processing

As it was noted before, in most cases the same antenna is used for the generation of the B_1 field and for the reception of the NMR spin echo signal which usually is extremely low with amplitudes of less than 1μV. The calibration of such NMR tools is performed using special water tanks. Such tanks represent 100% total porosity $P_t = 1\text{-}V_g/V_b$, here V_g and V_b are the grain and bulk volumes respectively. This produces maximum signal amplitude at definite Larmor frequency. In a rock formation, as only a fraction of total volume is filled with water, oil or gas, the NMR signal amplitude is proportionally less.

Due to the low amplitude of the NMR echo signals, a resulting low signal to noise ratio (SNR) is achieved. To increase the SNR, the following methods are used: 1) linear summing (stacking) of the echo signals, 2) the application of a specially shaped window (often a Hann pulse) to the received signal in the process of converting it from analog to digital in order to funnel the maximum signal energy while limiting noise, 3) synchronous measurement of the signal within a narrow band determined by the excitation pulse envelope (usually a

Hann pulse) (Akkurt, et al. 2001), 4) using a pulse to pulse phase switching technique (PAPS) to cancel out any of the system's synchronous noise (Coates, et al. 1999; Sigal, *et al*. 1999).

1.2.4. Nuclear Magnetic Resonance Results Interpretation

The NMR signal train decay speed (relaxation time) in rock pores (liquid deposits) depends on three main mechanisms: 1) the surface relaxation due to contact with a solid surface, which affects both polarization T_1 and relaxation T_2, 2) bulk fluid relaxation of the fluid itself, which affects both polarization and relaxation T_2, also the diffusion of the excited molecules in the gradient field from the volume being affected to adjacent volumes with different Larmor frequencies affected only by the T_2 relaxation. The fluid in different rock formations reacts differently to NMR pulses and the echo signals decay with the different time constants. This makes it possible to measure multiple parameters after the signal is processed.

The relaxation curves shown in Figure 1.4 illustrate the effects of pore size (sizes of the liquid deposits) on the relaxation times and the complexity of the resulting relaxation curves (Coates, et al. 1999). Fluids located adjacent to solid

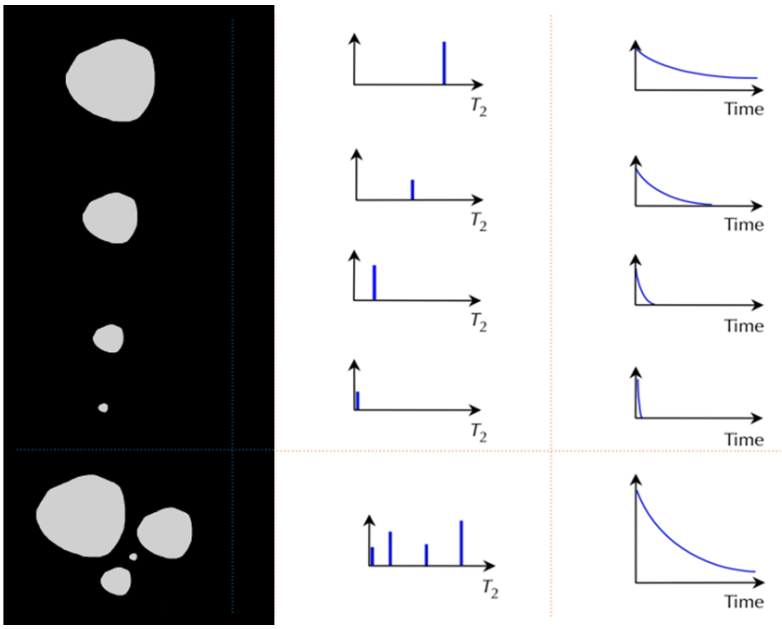

Fig. 1.4. Relaxation time for different pore size (Coates, *et al*. 1999)

surfaces transfer their energy extremely fast and their contribution to the echo train signal being measured is negligible. Thus these unrecoverable fluids have low visibility as NMR signals. When the pores (liquid deposits) increase in size, the NMR signals response from the rock formation, both as to their amplitude and relaxation times, become measurable and available for processing. Methods used to improve the signal-to-noise (SNR) and to properly process the data being acquired are described in (Harris, 1978; Blackman, et al. 1958; Menger, 2003; Freedman, 2006). Multiple relaxation processes when combined make up the exponent-like function, consisting of multiple components, all having different starting amplitudes and different time constants. The decomposition of the relaxation / decaying curve into its original exponents is called inversion. By varying the parameters of the experiment such as the polarization time *TW* and the time between the refocusing pulses *TE*, the NMR tool can be "fine-tuned" to recognize certain types of formation fluids, based on their expected relaxation times.

1.3. Nuclear Magnetic Resonance Tool Block Diagram and Operation

A block diagram of a typical well logging NMR tool is shown in Fig. 1.5 and waveforms of the antenna voltage pulses and transmitter output current pulses are provided in Fig. 1.6. The Uphole module, located on the surface, provides power for the tool through a standard 600VDC line via the cable for the Wireline tools. For logging while drilling (LWD) tools power is provided by a local 12 V to 36 V battery. The Low Voltage Power Supply provides the tool modules with all the voltages needed by their digital and analog circuitries.

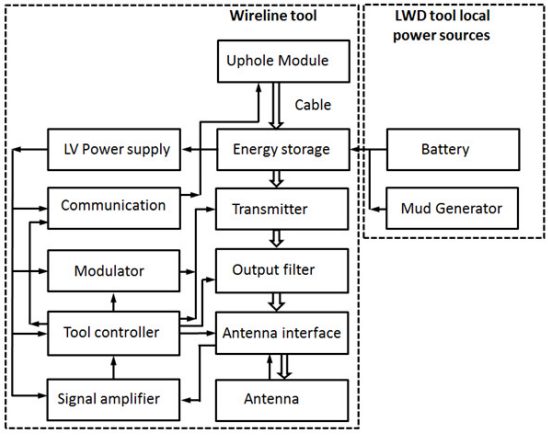

Fig. 1.5. Block diagram of NMR tool

The capability of the cable delivering power is limited by the resistance of the cable itself (50Ω to 150Ω total) and cannot support the generation of even a tenth of the kVA pulses needed for the excitation of the NMR antena. Thus capacitive energy storage is used as the local buffer. The Tool controller via the Modulator operates the Transmitter and directly switches Output filter. This then redirects via the Antenna interface the RF power pulses generated by the Transmitter to the Antenna or, when in its receiving mode, allows the NMR echo signal that is picked up by the Antenna to enter into the input of the Signal amplifier. This NMR analog signal after amplification is then converted into a digital signal and is processed using the tool‘s firmware. The operation of the system is corrected using the antenna temperature sensors and, if needed, information obtained from the other tools in the string. The Communication module provides the capability of exchanging information between the tools in the string and the Uphole module via the same cable.

The Transmitter, being a high frequency switch mode DC/AC converter, produces pulse–width modulated (PWM) rectangular voltage (Figure 1.7) with the first harmonic components restored as antenna voltage after passing through the filter in the antenna‘s parallel resonant tank. (Chireix, 1935; Doherty, 1936; Dent, 1998; Perreault, 2011). The antenna current is Q times (Q is quality factor of the antenna) greater than the transmitter output current due to parallel resonance.

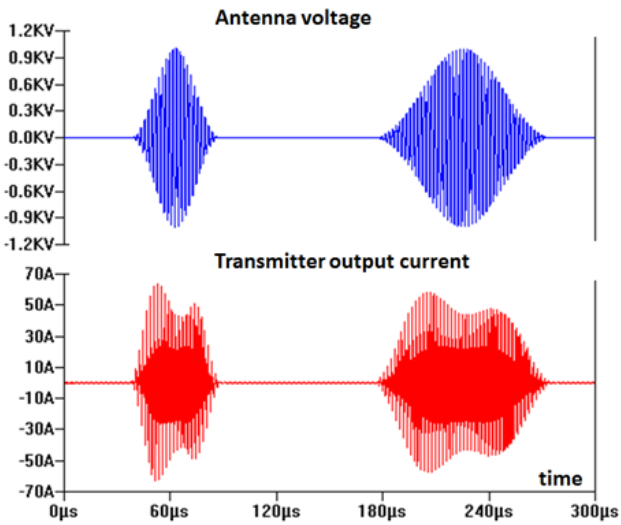

Fig. 1.6. NMR antenna voltage and the transmitter output current for 90 deg tipping (left) and 180 deg refocusing (right) pulses

The Modulator provides a set of control signals to the transmitter input, which form the envelope of the antenna voltage (and the resulting current) and create the B_1 magnetic field. The operational frequency, equal to the Larmor frequency, together with other necessary signals are provided by the Tool controller.

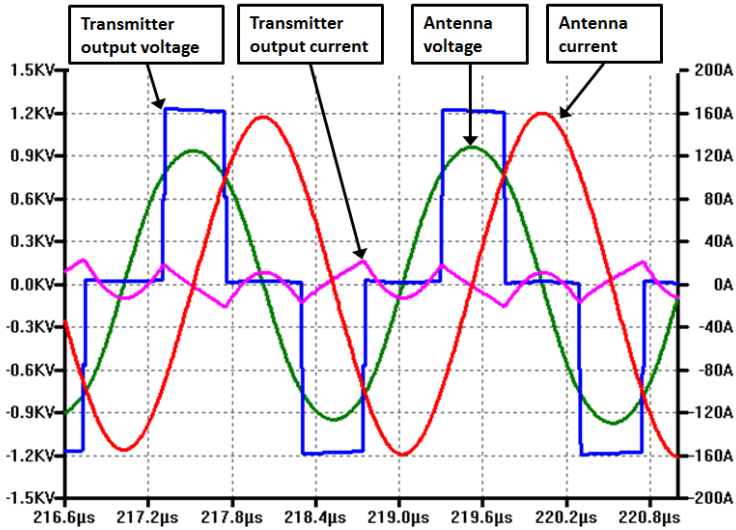

Fig. 1.7. Waveforms of transmitter and antenna signals

The Output filter limits the peak value of the Transmitter output current and uses switcheable capacitors to tune its resonance to the antenna frequency. The Antenna interface directs the transmitter output current to the resonant antena, thus exciting in it voltages of over 1000V peak and antenna currents of a few hundred amps peak. When the pulse generated by the Transmitter ends, the Transmitter shuts down and Antenna interface dissipates the residual energy stored in the resonant system. It then redirects the NMR echo signal picked up by the antenna coil to the input of the Signal amplifier. This amplifier is needed to increase the NMR echo signal amplitude from fractions of microvolts to ~1 V for processing by the ADC of the Tool controller.

1.4. Nuclear Magnetic Resonance Tool Antenna

The main purpose of the NMR logging tool is to map the per layer distribution of the oil or gas contained in the formation vs. its depth with the highest possible accuracy in order to identify its most productive layers. This is needed to plan

correctly the optimal sequence of the engagement of the layers for maximum productivity and total reservoir use. The sensitive volume of the NMR tool has to be located inside the rock formation not being invaded by the drilling mud.

Another type of NMR tool is used for the analysis of the well fluid produced by the prospective formation layers in real time and under real well conditions to determine the possible well productivity. This fluid analyzer has a sensitive volume inside the tool and operates by redirecting the well fluid flow to an internal antenna. In both cases, the NMR antenna uses permanent magnets to create static magnetic field B_0 and a coil or set of coils for oscillating field B_1 and for picking up the NMR echo signal.

1.4.1. External Field Antenna

The first successful pulsed NMR logging tool (Taicher, et al. 1988) was introduced by the small Pennsylvania-based startup company NUMAR in 1992. Two years later, the giant energy service company Schlumberger brought to the market its CMR tool (Kleingerg, et al. 1986). The difference between those two tools is the antena design. NUMAR took the cylindrical sensitive volume approach (NUMAR Prime tool, US Pat. Nos. 4,710,713; 5,212,447; 5,376,884; 6,023,164) in which the cylindrical volume is located deep inside the formation and the tool‘s position in the well does not affect the accuracy of the tool. The configuration of the sensitive volume is shown in Figure 1.8 left.. The CMR sensitive zone of the Schlumberger tool is smaller (Figure 1.8) right (US Pat. US 5,023,551, US 5,376,884) and the tool needs a centralyzer to press the sensitive side of the antenna to the formation‘s wall to prevent receiving a NMR signal from the mud. Each approach has its own anvantages and disadvantages (Akkurt, *et al*. 2009). The Schlumberger side-looking tool is more compact, cheaper and requires less power for the tipping and refocusing pulses than the NUMAR cylindrical volume tool, but the drawback is its lower logging speed. On the other hand, the huge antenna used in the NUMAR Prime tool requires a tenth of kVA of the RF power to produce tipping field B_1 deep in the formation (Miller, 1990).

The NUMAR Prime Tool‘s cylindrical sensitive volume, located deep in the rock formation, provides reliable data while avoiding the registry of any effects caused by well washouts at different depths from the tool antenna surface.

The magnetic field B_0 of the permanent magnent closer to the surface of the antenna is stronger and its Larmor frequency f_1 is higher than the f_2 in layers, located at distances r_1 (closer) and r_2 (further) from the center of the tool. This is shown in Fig. 1.9. The gradient field B_0 allows the tool to excite and to receive echo signals from different sensitive volumes (layers) independently by using different excitation frequencies. The layer thicknesses that are produced are only

~1mm (for the NUMAR Prime tool) and the generated NMR have low amplitudes and low SNRs.

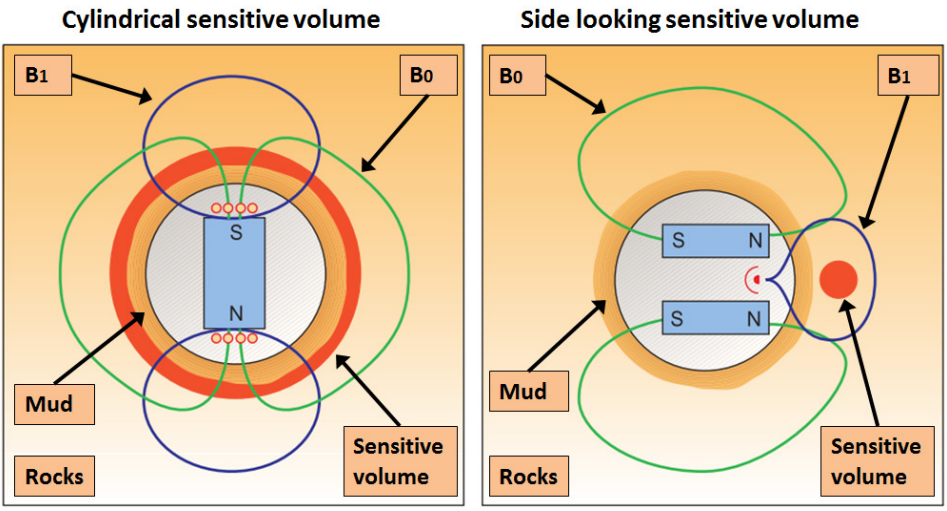

Fig. 1.8. Sensitive volume of cylindrical and side looking anntenas (Kenyon, *et al*. 1995)

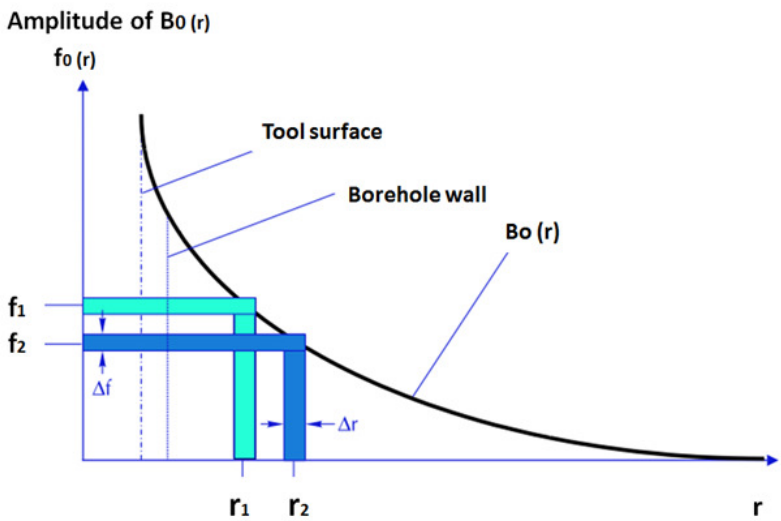

Fig. 1.9. Magnetic field inductance *vs*. distance from antenna surface and corresponding Larmor frequencies (f_1 and f_2), (Coates, *et al*. 1999)

The thickness of the formation‘s volume being sensed is proportional to the bandwidth of the excitation pulse and is reversely proportional to the duration of the pulse. As a result, the shorter the excitation pulse, the wider the bandwidth and the greater the responding volume, which in turn produces higher amplitude echo signals. A decrease of the B_0 gradient also increases the volume being sensed. The ultimate situation is when the permanent magnetic field is highly homogenuous in a particular volume and RF field is orthogonal to B_0 in the whole of this volume, which makes it similar to laboratory equipment picking a NMR echo signal from the whole volume.

Thus the cylindrical sensitive volume NMR antenna provides the highest logging speed, looks deep and is less sensitive to well washouts, but to generate tipping pulses in high volumes, it needs a transmitter capable of generating tenths of kilovolt-amp pulses at Larmor frequency. This is a challenging task for power electronics, operating at high temperatures in high pressure housings.

1.4.2. Internal Field Antenna

A separate and extremely important task when evaluating the produceability of an oil field is the analysis of the fluid in its natural environment in a well as the fluid is being produced from a certain layer of the formation. Analysis of such downhole fluid samples is desirable for many oil industry applications. This is typically done by bringing up samples to the surface using sealed containers and then sending these samples for measurement at laboratories. A number of technical and practical limitations, however, are associated with this approach and their cost and the time that needs to be spent are often unexceptable.

The main concern is also that the sample(s) brought up to the surface may not be representative of the downhole geologic formation due to the fact that only limited sample materials from a limited number of downhole locations can be extracted and taken to the surface. Thus the taking of samples to the surface is impractical when the purpose is to measure the fluid in a dense grid of sample points. Therefore, by necessity, such measurements will provide only an incomplete picture of the downhole conditions sought to be analized. The temperature of the the fluid in a dense grid containing oil (gas) significantly affect the fluid viscosity and the assessed well produceability.

In addition, such samples frequently contain highly flammable hydrocarbon mixtures under pressure. Depressurization of these containers frequently also leads to the loss of their gas content. Thus the handling of such test samples can be hazardous and costly. Further significant problems are caused by fluid phase changes during retrieval and transport, also by diffculties in recreating reservoir conditions and the signifcant time delays that are associated with such laboratory analysis.

It is thus apparent that ideally such fluid sampling and analysis should be preceded or even entirely replaced by remote downhole fluid analysis of as many samples as is desired, with the final results being made instantaneously available at the well site. Nuclear magnetic resonance (NMR) technology is well suited for this purpose since it enables the user to determine many properties of the in-situ formation fluid without extracting numerous samples. These properties include the hydrogen density, self-diffusivity, and the relaxation times *T1* and *T2*. NMR devices, methods and pulse sequences used in logging tools are described, for example, in US. Pat. Nos. 4,350,955, 5,557,201, 4,710,713, 4,717,876, 4,717,877, 4,717,878, 5,212,447, 5,280,243, 5,309,098, 5,412,320, 5,517,115, 5,557,200, 5,696,448, 5,936,405, 6,005,389, 6,023,164 and 6,051,973. Direct downhole measurement of certain fluid properties is well known and several commercially available tools can be used for ths purpose. These include the RDTTM tool manufactured by Halliburton, the Reservoir Characterization Instrument (RCITM) manufactured by Western Atlas, and the Modular Formation Dynamics Tester (MDTTM) made by Schlumberger. These tools have modular designs which allows them to be reconfgured at the well site. Typically, these tools provide pressure-volume measurements, which can be used to differentiate liquids from gases, and are also capable of providing temperature, resistivity and other mechanical or electrical measurements. However, these tools do not generally provide NMR measurements, as discussed above.

The use of NMR measurements to determine the properties of downhole formation fluids is also known in the field. The first application of this method was described in US. Pat. No. 6,111,408, which discloses a method and apparatus for making direct downhole NMR measurements of formation fluids. The device presented in this patent, however, requires that a portion of the fluid be diverted from the main flow line and be held stationary for the duration of the measurement, which may take about a minute. A concern about the use of this device for this purpose is the occurrence of possible fluid phase separation due to its diversion from the main flow line and separation due to gravity once the sample has been separated and allowed to settle. Also depending on the relative concentrations obtained, the sample chamber may contain only a subset of the phases present in the flow line.

This first in-situ well fluid analyzer (MRILab) has two sets of permanent magnets. One of these located in the polarization section provides spin orientation while the fluid flows through the internal tube as shown in simplified Fig. 1.10. In the resonance section, permanent magnets provide an extremely homogeneos magnetic field, which creates the tipping and refocusing at the same Larmor frequency of the nuclei at all their internal values (Doty, 2007).

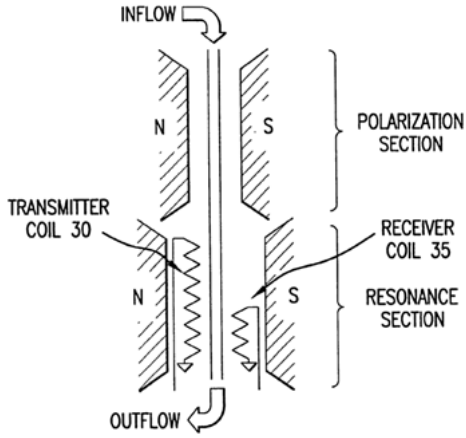

Fig. 1.10. Cross section of MRILab fluid identification tool antenna (Prammer, *et al.* 2002)

The transmitter coil covers the full length of the resonance section and excites the passing fluid, while the receiving coil in the lower part of the resonant coil picks up the echo signal from the fluid in the lower part of the resonance section.

The accuracy of this in-situ fluid analyzer is affected by one unpredictable factor, which causes the antenna electrical resonant frequency to change, thus mismatching the Larmor frequency. The antenna's resonance frequency (4.25 MHz) is defined by the coil inductance and the total tank capacitance. This includes the set of temperature compensating capacitors, the stray capacitance C_t between the coil wire turns and the extra capacitance consisting of C_i through the tube dielectric and C_f through the well fluid shunted with the fluid resistance R_f as shown in Fig. 1.11. The well fluid, passing through the isolated tube, used as the antenna coil mandrel, may be either crude oil with the dissolved gas, or water or a mix. The dielectric parameter for oil $\varepsilon = 2.4$ and for water $\varepsilon = 80$, while the actual fluid may be a mix of unknown proportions (Petroleum, 2008). With dielectric constant of the analyzed fluid changing up to 33 times, it is difficult to design a resonant antenna operating stable enough to maintain tool accuracy. Attempts to add a special tuning system, based on switching or variable capacitors, sensors etc. were technically complicated, decreased the sensor reliability and required more space.

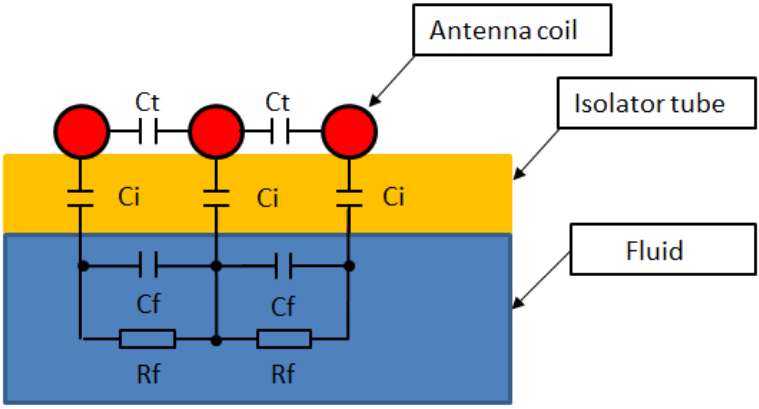

Fig. 1.11. Stable C_i and variable C_f, R_f distributed parameters of NMR antenna

Thus there is a need for the development of a simpler method for decreasing the dependence of the NMR antenna resonant frequency on the well fluid dielectric properties, which does not require a complicated tuning system.

1.5. Nuclear Magnetic Resonance Transmitter

The transmitter in the NMR tool is a high frequency DC to AC converter loaded with a resonant LC tank (NMR antenna). In the process of measurement, a sequence of multiple identical excitation pulses is generated, forming a so-called pulse train (Fig. 1.12). Energy from local capacitive storage is then converted into RF pulses and dissipated in the antenna and transmitter. All the sine waveform shaping methods developed for 50Hz – 60Hz industrial applications, based on the use of multiple times higher carrier frequency modulation, cannot be used for this, due to their unacceptable switching losses.

A simplified schematic of the currently used transmitters is shown in Fig. 1.13. The RF pulse amplitude modulation is based on the Chireix-Doherty out-phasing method (Chireix, 1935; Doherty, 1936), which combines two identical amplitude V0 voltages with controlled symmetrically opposite phase shifts as shown in the phasor diagram Fig. 1.14. This modulation method was originally designed for operation with sinusoidal voltages, generated by the vacuum tube-based output stages of radio transmitters. Progress in the development of high voltage, high current, fast-switching MOSFETs, however, makes it possible to fit such NMR transmitters in high pressure housings and to operate them at the elevated temperatures found in the depths of oil and gas fields.

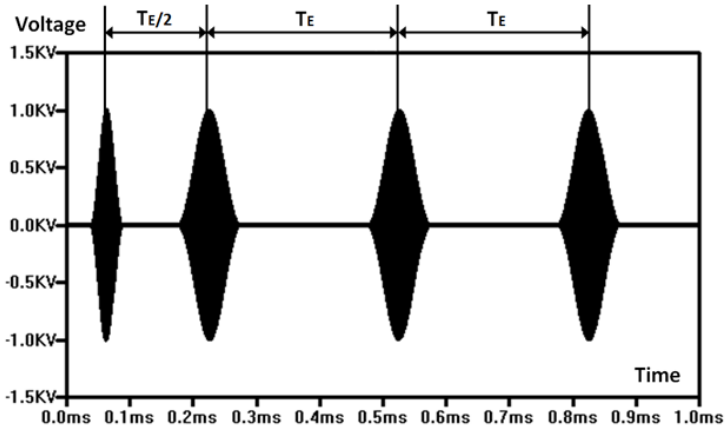

Fig. 1.12. CPMG RF pulse train at NMR antenna

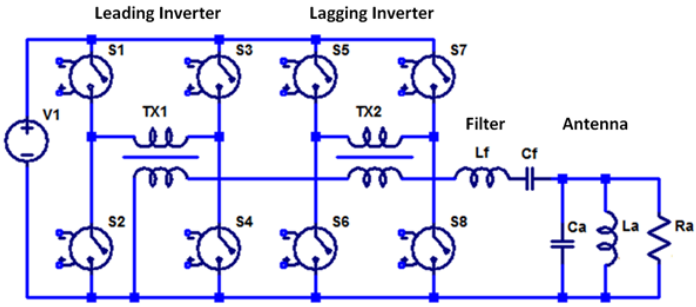

Fig. 1.13. NMR transmitter power stages, filter and antenna

To decrease the transmitter (Figure 1.13) power dissipation, all the power components (MOSFETs S1 – S8) were operated as switches with low drain-to-source resistance R_{dson}, (Mohan, *et al*. 2003; Dent, 1998). The transmitter included two full bridge inverters, named the leading and lagging, two combining transformers *TX1* and *TX2*, the transmitter output filters L_f and C_f and a resonant load antenna C_a, L_a, R_a.

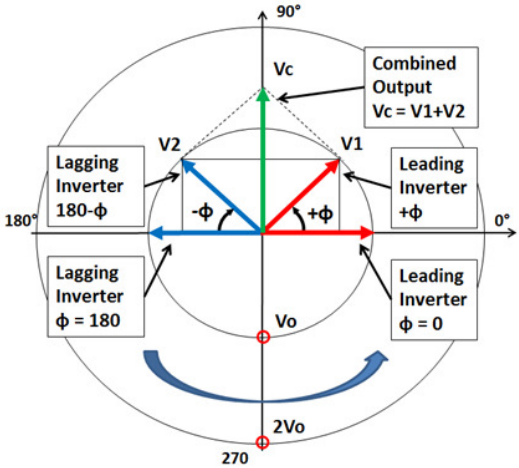

Fig. 1.14. Chireix-Doherty outphasing modulation phasor diagram

To achieve maximum efficiency and output power, each inverter produced 50% duty cycle pulses, providing the maximum value of the first harmonic. When the two output voltages from *TX1* and *TX2* were combined in phase (zero phase shift, $\varphi = 0$), the resulting output voltage doubled producing maximum antenna voltage. When the signals having opposite phase shifts ($\varphi = \pi$) were combined, the resulting voltage was zero. The first harmonic peak voltage, restored at the antenna parallel resonant tank as V_a, depended upon the power bus voltage V_B and the phase shift φ which can be described as:

$$V_a = \frac{8}{\pi} V_B \sin \varphi \tag{1.3}$$

The operation of the output stages at 50% duty cycles is beneficial not only for maximum power output, but also provides enough time for recharging the gate drivers. This is also needed for the operation of the output stages in their soft switching mode, thereby decreasing switching losses, and to store enough energy in the magnetics for lossless commutation of the output transistors.

1.5.1. Switch Mode Transmitter Harmonics

Such switch mode operation, when operating at 50% duty cycles, minimizes the power dissipation of the components and also produces multiple harmonics in the output voltage of each converter. (Fig. 1.15). Only the fundamental harmonic

is used for NMR antenna excitation. The amplitude of each produced harmonic V_n at 50% duty cycle is defined as:

$$V_n = \frac{4}{\pi n} V_B \tag{1.4}$$

where n is the hamonic number and V_B is the full bridge bus DC voltage.

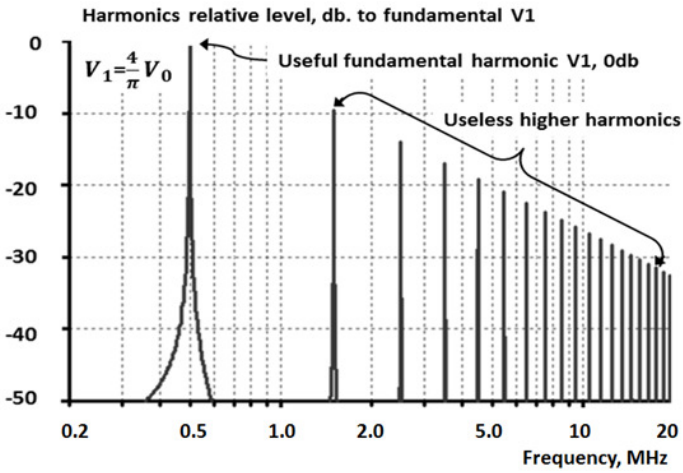

Fig. 1.15. Spectrum of a 50% duty cycle signal

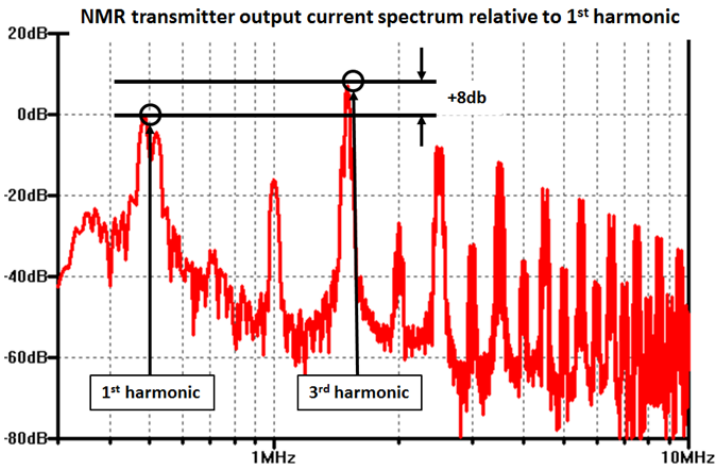

Fig. 1.16. NMR transmitter output current spectrum

The NMR antenna is a parallel resonant tank with maximum impedance at the resonant frequency. For higher harmonics, the load impedance is low and transmitter output current harmonics are limited only by the series LC filter.

The filter with the antenna tank form a fourth order resonant system with a so-called saddle transferring characteristic and low input impedance at series resonance above the first harmonic. The output current of the transmitter was analyzed and the resulting signal spectrum or harmonic distribution of the re-focusing pulses is shown in Fig. 1.16. The third harmonic was found to be +8db the level of the fundamental one, which means that the energy dissipated by the third harmonic current was 6.3 times higher than that by the fundamental one.

The high content of the higher harmonics in the transmitter output current produces excessive heat dissipation by all current carrying components. This includes the output transistors, the local ceramic capacitors and the magnetic windings.

To decrease or to eliminate the unwanted higher harmonics from the switch mode converter output signal, multiple approaches have been developed starting with Pulse Width Modulation, which uses multiple control methods (Patel, *et al*., 1973; Rodriguez, *et al*., 2002; Rodriguez, *et al*., 2007; Rodriguez, *et al*., 2012; Li, *et al*., 2000; Carrara, *et al*., 1992; Cendelci, *et al*., 1998). But due to the high fundamental frequency, only the natural frequency (fundamental frequency) switching of the multiple individual modules forming a “ladder style” combined output voltage is suited for use in Nuclear Magnetic Resonance transmitters. This is shown in Fig. 1.17 (Cendelchi, *et al*., 1998; Baker, *et al.,* 1974; Bhagwat, *et al.,* 1981; Tolbert, *et al*., 1999; Ilves, *et al*., 2011; Ilves, *et al*., 2015; Du, *et al*., 2004; Lai, *et al*., 1996; Kang, *et al*., 2012; Konstantinou, *et al*., 2010; Li, *et al*., 2015; Dahidah, *et al*., 2014; Darus, *et al*., 2014; Antunes, *et al*., 1999) The Phase Shift PWM method appears to be promising for this application as it is based on Multiple Module Converters (MMC), operates with the fundamental frequency and combines their output voltages using high frequency output transformers. In the frequency range 0.5 MHz to 1 MHz, these combining RF transformers are relatively small, fit the high pressure housings and are reliable for high temperature applications.

The behaviour of the main power dissipating components, such as the MOSFET switches and capacitors, thus have to be evaluated for operation at elevated temperature, which exceed in some cases their manufacturers‘ specifications.

This power dissipation increases the components‘ temperature and thereby reduces their reliability (life expectancy). Operation in the confined space of a high pressure housing, made of mechanically strong material like Inconel with low thermal conductivity, also creates problems in providing it with a reliable heat-sink passage from the electronic module to the ambient. Operation in deep

wells with ambient temperatures up to 175 °C exaggerates these heat-related problems. This increased power dissipation per pulse also depletes the main capacitive energy storage or battery faster and decreases the number of experiments that can be conducted per layer, resulting in losses of accuracy.

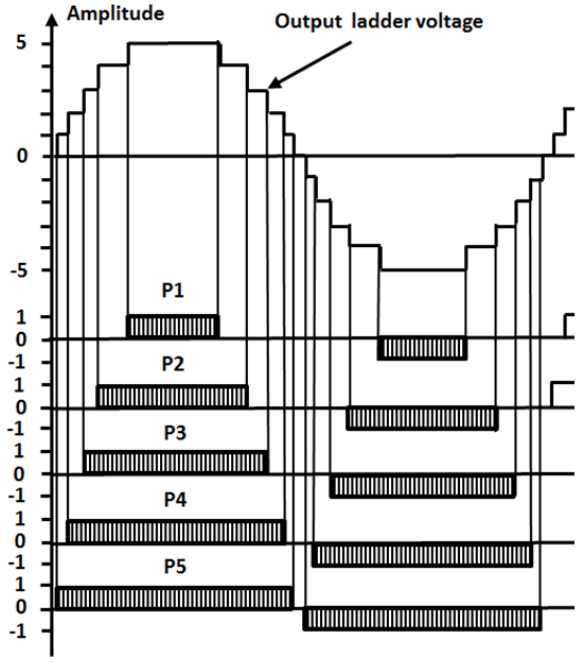

Fig. 1.17. Ladder style voltage formed by multimodule converter

Thus special means and methods need to be developed to remove the higher harmonics from the transmitter output current or to decrease the higher harmonics content.

1.5.2. Power Transistors

The most important components of the switch mode DC/AC converter, used as NMR transmitters, are the power switches. For the referred to frequency range of a few hundred kilohertz to one megahertz, which is typically used in the multifrequency cylindrical antenna, the transmitter needs to produce an over 1000 V peak output with a current capability of a few tenth of amps and minimal internal power dissipation.

The wireline tool DC power line standard is 600V and for the battery powered ones, this varies from 200V to 400V depending on the designer‘s approach. The voltage rating for the switch thus should be higher than the DC bus, plus any expected overvoltage spikes up to 100–200 V. This means that 600 V to 1000 V rated switches are needed for use in the NMR transmitter output stages. Only MOSFET transistors, however, can switch tenths of amps in less than 100ns with low losses. All other high power solid state switches, such as thyristors, IGBT or silicon bipolar transistors, are too slow for use in NMR transmitter applications (Mohan, *et al*. 2003).

The MOSFET transmitter switch dissipates power due to the conductive losses. This is proportional to the RMS value of the passing current and the drain-to-source resistance R_{dson} of the transistor. The drain leakage losses and the switching losses are proportional to the operating frequency and MOSFET output capacitance. The gate recharging losses are also proportional to the operating frequency.

During low frequency and high current operation, the dominant component of the MOSFET power dissipation is the result of conduction losses. Dissipated power is converted into heat and channeled from the transistor die to the ambient (well fluid) via thermal resistance (R_{th}), which includes the thermal resistance die to the package, resistance of the package to the heatsink and resistance of heatsink to the ambient. The total value of R_{th} can be varied in wide range (Mohan, *et al.* 2003; Singh, *et al*. 2001). The lower the R_{th}, the less is the temperature difference between the ambient and the transistor die. To decrease power dissipation, multiple transistors may be connected in parallel to share current and thus to reduce the total and per switch conductive losses.

To properly design the transmitter output stages and to determine the optimal number of parallel switches that would be needed for current sharing, the MOSFET R_{dson} behaviour or the voltage drop can be described as a function of both the current and the temperature along an expected temperature range. It is known that at higher temperatures, the drain to the source voltage drop (V_d) increases significantly as shown on Fig.1.18 for the IRF330 and APT40SM120J. At the same time, V_d depends on the drain current (Locher, 1988; Mohan, *et al.* 2003; Singh, *et al*. 2001; Tyshko, *et al*. 2012).

Manufacturers provide MOSFET datasheets containing important reference data, which include the V_d measured at a certain test current (I_t) and maximum pulse and maximum continuous currents at temperatures ranging from 25°C to 150°C. This data is usually packed with a set of graphics, which show the output drain characteristics, such as the drain current I_d *vs*. the drain voltage V_d with a static drain-source resistance at 25 ºC and 150 ºC. This is shown in Fig. 1.19 for the IPB60R099 transistor (IPB60R099, 2009). The green box shows the area, which should not be exceeded at high temperatures. It is known that for the same

die size the V_d significantly increases with the drain voltage rating (Singh, *et al.* 2001). Thus, one and the same model can not be used for the MOSFETs with the different voltage ratings.

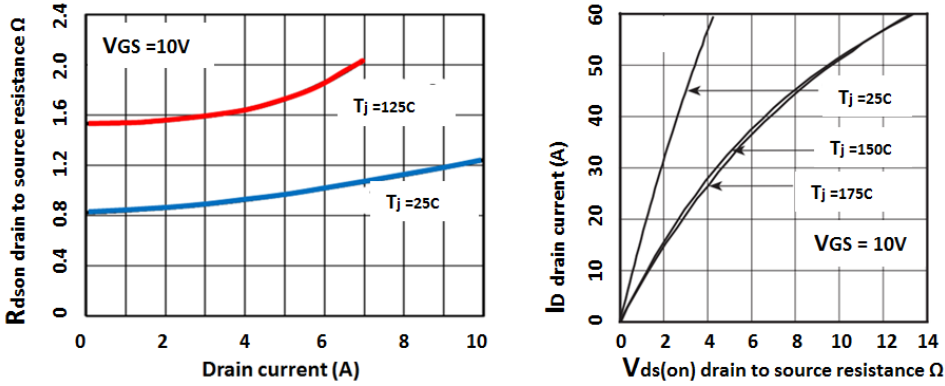

Fig. 1.18. R_{dson} *vs.* I_d for IRF330 transistor (left) and the I_d *vs.* V_d for APT40SM120J transistor (right) at different temperatures (Locher, 1988)

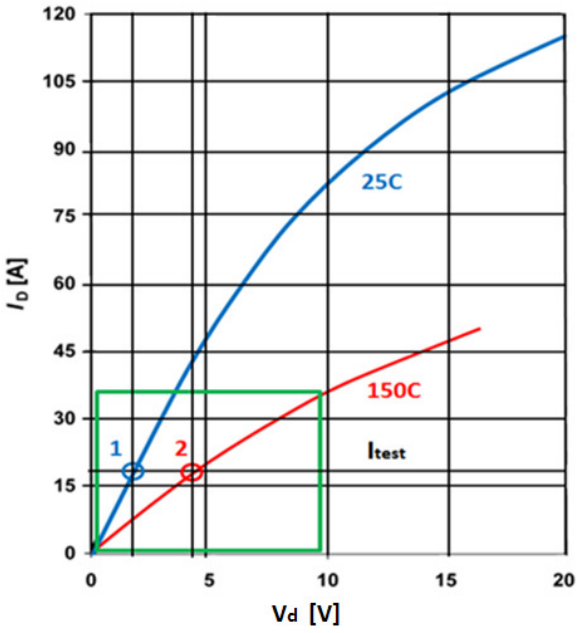

Fig. 1.19. I_d *vs.* V_d of MOSFET at 25 °C and 150 °C (IPB60R099, 2009)

The positive coefficient of the drain-to-source resistance is due to the electron and hole mobility decrease with the increase of temperature. In (Locher, 1988) the dependence of the R_{dson} *vs*. temperature was estimated using the following equation:

$$R_{dson}(T) = R_{dson,25°C} \cdot (\frac{T}{300})^{2.3} \tag{1.5}$$

where T is the absolute temperature and $R_{dson,\ 25\ °C}$ is drain-to-source resistance value at 25 °C.

Another polynomial equation for R_{dson} *vs*. temperature (T) dependence was proposed in (AN9010, 2000; Divins, 2007):

$$R_{dson}(T) = R_{dson,25°C} \cdot (aT^2 + bT + c) \tag{1.6}$$

Here a, b and c are empyrical coefficients.

Different transistors have different drain voltage and current ratings and respectively different Itests. In the NMR transmitter, the MOSFET is used as a switch and its drain current is a parameter, which is determined by the other components and conditions, while its drain voltage is a function to be defined / calculated to determine both its momentary and average power dissipation. Known expressions for R_{dson} do not include extended temperature ranges and do not include its dependency on the drain current. Thus for the NMR transmitter design, research has to be conducted in order to develope a new model, which describes the R_{dson} as a function of both its temperature and current and which verifies its usability in temperature ranges up to 200 °C.

1.5.3. Capacitors

The transmitter currents, switched by the power MOSFETs, pass through the local energy storage units, which are based on low ESR capacitors. Those capacitors have to operate in a temperature range over 175 °C and have to be able to carry high AC current, including all the harmonics of the transmitter output current with low losses to prevent capacitor overheating (Zakis, *et al*. 2012).

Of the wide assortment of "off the shelf" capacitors, only a few types can operate at temperature ranges of 175 °C to 200 °C and can be used in NMR tools. Multilayer X7R ceramic capacitors, known for their maximum energy density and high stability COG/NPO appear to be suited for this purpose as NMR transmitters mostly rely on X7R capacitors for use as local DC filters.

In the data available from the manufacturers (AVX, 2015, TDK Product, 2015, TDK Equivalent, 2015, Ceramic, 2016, Multilayer, 2016, KEMET, 2016, Voltage coefficient, 2016, AVX, X7R, 2016, AVX Advanced, 2016) and from research papers (Tura, *et al*. 1996; Fortunato, 2012) on X7R capacitors, two main parameters, the capacitance and equivalent series resistance (ESR), are characterized as useable in the full temperature range up to 150C and a maximum rated DC operating voltage in the frequency range over 10MHz.

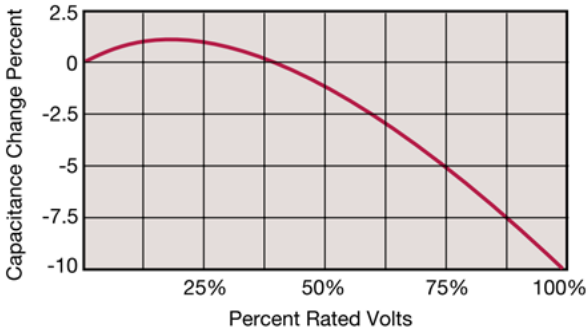

Fig. 1.20. Capacitance value change (in %) *vs*. DC voltage bias for AVX X7R capacitors (AVX, 2015)

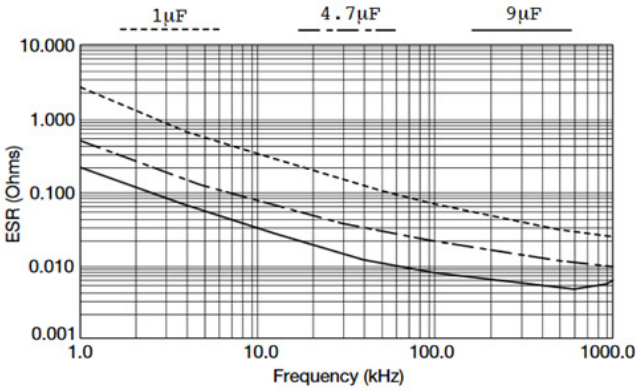

Fig. 1.21. Typical ESR *vs*. frequency dependence for AVX XM04 type capacitors. (TDK Product, 2016)

Multilayer Ceramic Chip Capacitors

Commercial Grade (Mid Voltage (100 to 630V)) / C5750 series (3/3)

Circuit Diagram

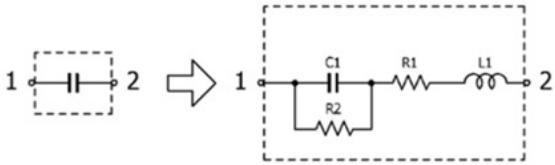

Part No.	C1[pF]	L1[nH]	R1[ohm]	R2[Gohm]
C5750JB2A155K230KA	1,500,000	0.650	0.0047	0.333
C5750X7R2A475K230KA	4,700,000	0.650	0.0025	0.106
C5750X7S2A106K230KB	10,000,000	0.650	0.0034	0.0500

Fig. 1.22. Equivalent schematic of multilayer X7R capacitors recommended by manufacturer (TDK Product, 2016)

The data presented in Figs. 1.20 to 1.22 appeared to be sufficient for use in simulation models of the NMR transmitter design. The temperature rise ΔT was calculated based on power dissipated in the capacitor using formula (1.7), (Magnetics, 2015):

$$\Delta T = \left(\frac{P_{mW}}{A_{cm2}}\right)^{0.833} \tag{1.7}$$

where ΔT is the component temperature rise over ambient temperature (no forced air flow), P_{mW} is the component dissipated power in mW and A_{cm2} is the component surface area. However, the testing of the high power converter, which ended in failure, showed that X7R multilayer ceramic capacitors, operating in DC filters, had a significantly higher temperature rise ΔT than the values that were provided in the manufacturer's equivalent schematic for the capacitor shown in Fig. 1.22 (Tyshko, *et al.,* 2016).

The mechanisms responsible for mechanical failures in the ceramic capacitors due to the electrical fields were investigated in (Dineva, *et al.* 2014). Thus the unexpected X7R ceramic capacitors failures and the resultant overheating question the validity of the standard X7R ceramic based capacitor model, and requires new analysis as to the actual behavior of such DC biased X7R capacitors.

1.6. Conclusions of Chapter 1 and Formulating Tasks for the Dissertation

The literature review and analysis of the NMR tools focused on the few main problems affecting the accuracy and reliability of these downhole logging tools. They include the following:

1. The internal NMR antenna is subjected to detuning due to the different dielectric parameters of the investigated well fluids. A simpler method thus needs to be developed to mitigate such detuning effects without involving additional hardware and software, which can increase the complexity of the tool and result in higher costs and lesser reliability;
2. The transmitter output current's higher harmonics exceed significantly the useful fundamental one and produce excessive power dissipation, which increases the transmitter temperature and decreases the tool's reliability. The transmitter design needs to be reanalyzed and changed in order to decrease or to cancel out the higher harmonics eminating from the transmitter output voltage;
3. The high voltage power MOSFETs, used in the transmitter output stages, operate in a high temperature range, thus exceeding the standard ratings provided by the manufacturers. MOSFET drain-to-source resistance R_{dson}, which defines the conductive power losses, needs to be investigated and behavioral models created, which provide verified Rdson dependence on the temperature and the drain current.
4. High energy density X7R ceramic capacitors need to be investigated to determine the reasons for their abnormal behavior, compared to that provided in the standard data sheets. These cause the X7R capacitors to overheat and fail.

2

Improvement of the Internal Nuclear Magetic Resonance Antenna through the Use of a Faraday Shield

This chapter provides the results of research on the effect of well fluids on the internal NMR antenna's resonant frequency. It also decribes a method for improving the stability of the antenna's resonant frequency by means of a slotted Faraday shield placed between antenna coil and the well fluid (Patents: US 7,164,267, 2004; EP1393096 EU, 2003; US 6,737,864, 2002)

2.1. The Effects of Well Fluid on the Nuclear Magnetic Resonance Antenna Resonant Frequency

To assess the possible detuning of the NMR antenna by different types of well fluids, a test setup was disigned. Fig. 2.1 shows a simplified block diagram of the actual test setup (Fig. 2.2). The test setup consisted of a shortened version of the NMR antenna coil (inductance *L1*) wounded over the plastic tube (*reservoir with formation fluid*). Inside this tube was then placed the fluid to be tested. The *generator* with low internal capacitance was then connected directly to the an-

tenna coil and the 5V *Laboratory DC power supply*. The *oscilloscope* was used for the measurement of the generator output frequency, which is defined by resonance frequency of tank consisting of the antenna (inductance *L1* = μH) and reservoir capacitance *C1* depending upon the type of fluid placed in the plastic tube. The oscilloscope voltage probe was connected to the separate low impedance output of the *generator*.

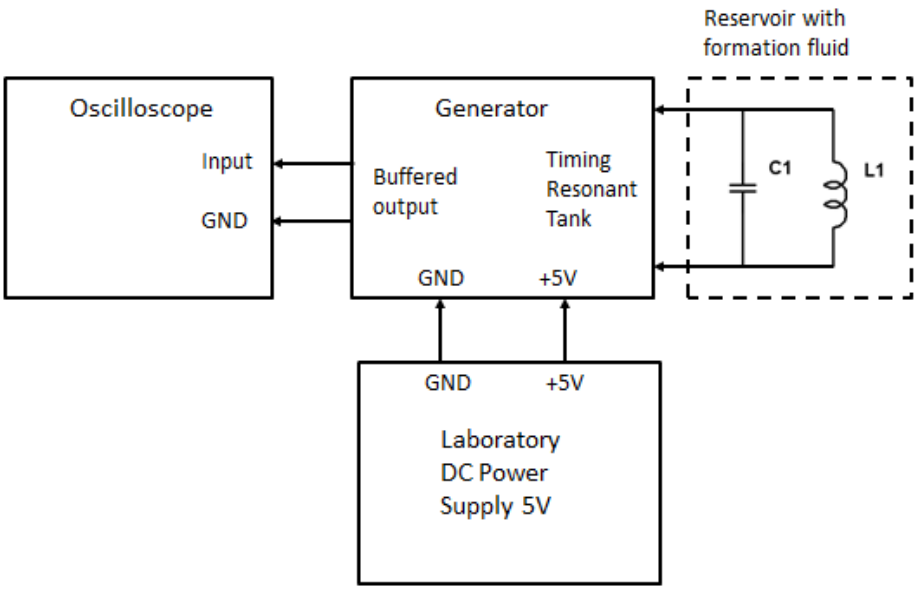

Fig. 2.1. Block diagram of the Antenna cell resonance test setup

The test setup (Fig. 2.2) was designed as following: the antenna cell was placed vertically onto the printed circuit board and the bottom of the tube was sealed with epoxy to facilitate fluid replacement. The generator's vertical board was placed as close as possible to the antenna to minimize the length of the wire, which itself adds inductance and parasitic capacitance. The 400MHz bandwidth oscilloscope WaveSurfer 44MXS-B was used to monitor generator operation and to measure the frequency of the generator. A 5VDC power supply provided the power for generator.

The plastic tube was filled with various well fluids and the resonance frequencies were measured for Air (no liquid), Oil, Mixed (50% oil + 50% water), Water (non-conductive) and Brine (highly conductive salt water). As antenna inductance was *L1* = 1μH the measured resonance frequencies provided to

calculate the equivalent tank capacitance *C1*. For calculation the well known Tomson formula $f_R = 1/2\pi\cdot(LC)^{1/2}$ was used.

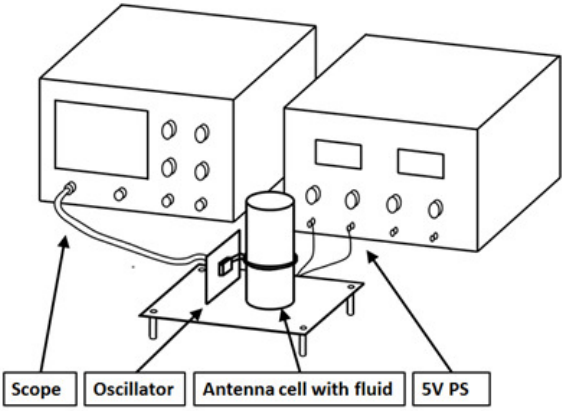

Fig. 2.2. Test setup with the antenna cell

Table 2.1. Antenna resonance frequency f_R and fluid equivalent tank capacitance *C1*

Fluid in test setup	Resonance frequency, MHz	Capacitance, pF
Air	65,7	5,8
Oil	58,7	7,3
Mix (50% oil, 50% fresh water)	47,1	11,3
Water (non-conductive)	40,4	15,4
Brine (highly conductive salt water)	40,0	15,7

The antenna setup test results showed significant variations of the resonant frequencies and changes of the capacitances by almost 3 times, which affect the tuning of the NMR antenna. The capacitance variations shown in Table 2.1 thus needed to be significantly decreased to prevent the detuning of the NMR antenna with a resultant decrease of the NMR tool's accuracy when measuring the characteristics of different well fluids. The date of *C1* presented in Table 2.1 were used as a reference for simulation of the electric field distribution in the antena with Faradey shield by ANSYS sofware.

2.2. The Internal Nuclear magnetic Resonance Antenna with a Faraday Shield

A simple solution which allows a decrease of the dependence of the NMR antenna resonant frequency on the electrical properties of the well fluid has been proposed (Prammer, *et al*. 2002; Prammer, *et al.* 2004). The electrical field generated by the windings of the coil can be terminated at the surface of a slotted copper tube, a Faraday shield, placed in an isolating tube between coil and fluid (Fig. 2.3, Fig. 2.4). This Faraday shield slot was parallel to the longitudinal direction of the coil as shown in Fig. 2.4. In this improved Antenna, the capacitive currents flowing through C_i (Fig. 2.3) were terminated by the Faraday shield and did not enter the well fluid. Thus only its longitudinal magnetic component entered the fluid during excitation and emanated from the fluid, thereby inducing the NMR echo signal in the receiver coil.

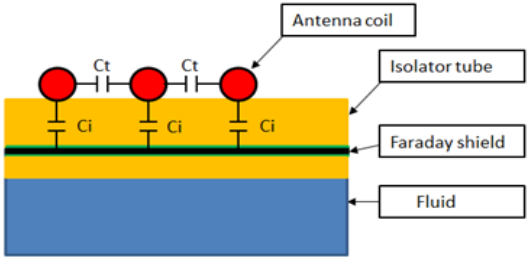

Fig. 2.3. Simplified diagram of NMR antena with Faraday shield

To verify the effectiveness of this proposed solution, the previously tested antenna was modified by adding to it a Faraday shield, a copper foil cylinder slotted in the vertical direction, which was fitted inside the tube and was isolated with Kapton tape to prevent its contact with the liquid. This cylinder was then connected to the ground.

The resonance frequency was then measured for five different fluids that had been placed in the tube Fig. 2.2. The results of this test are provided in Table 2.2.

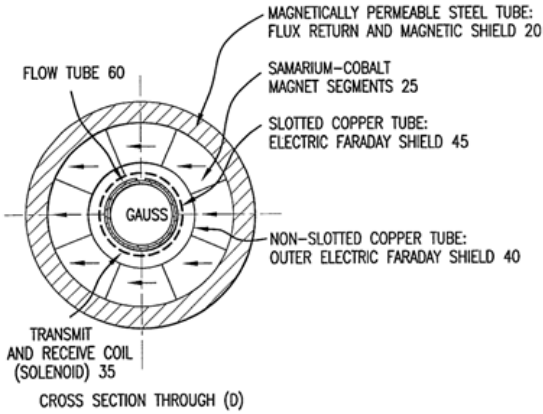

Fig. 2.4. MRILab sensor cross section with a slotted Faraday shield

Table 2.2. Resonance frequency f_R and fluid equivalent tank capacitance *C1* for antenna with a Faraday shield.

Fluid in test setup	Resonance frequency, MHz	Capacitance, pF
Air	39	16.5
Oil	38.4	17.1
Mix (50% oil, 50% fresh water)	38.2	17.2
Water (non-conductive)	38.1	17.3
Brine (highly conductive salt water)	38.0	17.4

The addition of the Faraday shield decreases the dependence of the antenna capacitance on the fluid. The cross section of the final configuration of this modified MRILab antenna is provided in Fig. 2.5. The well fluid enters the internal volume of the test cell from the top through flowtube 60 and then passes through diffusor 5, which slows its speed due to the greater cross-section of the internal tube compare to the upper opening of the flowtube.

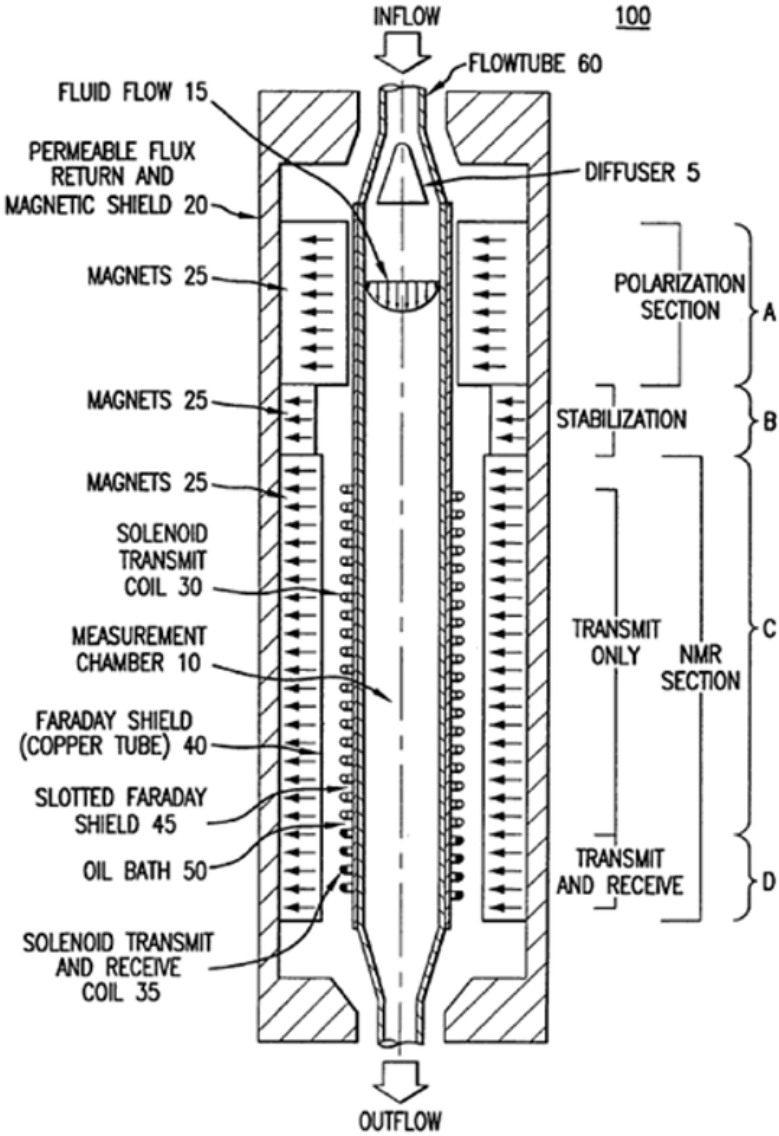

Fig. 2.5. Cross section of MRILab antenna with Faraday shield

The fluid passes through Polarization Section A with magnets 25, which provide a magnetic field significantly higher than that in the NMR section. This strong magnetic field quickly polarizes the fluid's proton magnetic moments. Thus when the fluid enters NMR sections C and D, its polarization is already at

saturation level and does not depend upon the velocity of the fluid flow. Magnets 25 in NMR sections C and D form the homogenous B_0 field 0.1T, orthogonal to the longitudinal direction of the antenna. The excitation RF pulses generated by the transmitter (shown in Fig. 2.7) are then applied to solenoid transmit coil 30 and the solenoid transmit and receive coil 35, creating in them RF magnetic field B_1 pointed in the longitudinal direction. This produces the proton tipping. The slotted Faraday shield 45 is located in the flowtube between the coils and the fluid. Additionally, external solid Faraday shield 40 is located between the coils and surface of magnets 25. This external shield stops the RF pulses from exiting the small space surrounding coils and prevents the external electromagnetic noise generated by the other logging tools from entering the Receive coil and interfering with the small NMR echo signal. The space between the magnets and coil flowtube 60 is filled with oil and the pressure difference between the well fluid and internal oil is maintained at a low level by means of a pressure equalizer. The tool pressure rating is 1800 atm.

The fluid slowly moving in the NMR sections is thus subjected to tipping pulses from the combined transmit and receive coils, while the NMR echo signal is picked up only by the receive coil from the lower fraction of section D. The purpose of this approach is to guarantee that the total volume of the fluid in section D had been properly tipped in section C before the fluid enters section D at any possible fluid flow speed.

By processing the NMR signal's decay and decomposition and by inverting this data into a time distribution function, it is possible to analyze the well fluid in real time.

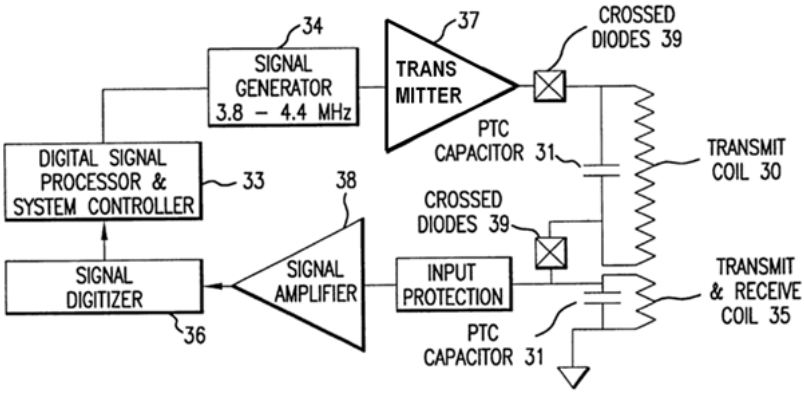

Fig. 2.6. Block diagram of the MRILab system

For testing the NMR antenna improved with the Faraday shield, the following apparatus was used (its block diagram is shown in Fig. 2.6). The operating frequency of 4.26 MHz allows the use of ADC and DSP for processing the signal. Variable frequency source 34, controlled by a processor, sends its signal to transmitter 37, which in turn drives transmitter antenna 30. All the timing functions, including widths and acquisition windows, are fully programmable. On the receive side, the signal from receiver antenna 35 is amplified, synchronously demodulated and integrated. The tool also performs its own calibration. All pertinent calibration factors are stored in the tool itself and after calibration, the echo amplitudes are reported on a scale of 0–2 V, which are suitable for use by the analog circuitries.

More specifically, as is shown in Fig. 2.5, the two coils 30 and 35 of the device were connected to resonating capacitors 31. These capacitors were of the COG/NPO type (zero temperature coefficient) and the PTC type (positive temperature coefficient), shunted in parallel, as shown. Their resultant temperature characteristic is such that with an increase of temperature and when the static magnetic field weakens (typically 1% per 100 °C) (Material, 2016), the capacitance increases at twice the normal rate (typically 2% per 100 °C). The resultant LC circuit resonant frequency thus drops to half the capacitor rate (1% per 100 °C) and as it follows the NMR resonance, this makes it unnecessary to retune the circuit.

In the transmit mode, controller 33 instructs the signal generator 34 and the power amplifier 37 of the apparatus to produce a radio frequency pulse in both coils. The high voltage applied causes all crossed diodes 39 to conduct, thereby connecting the two coils. In their receive mode, the crossed diodes stop conducting and the signal is received only from lower coil 35. The signal is then amplified, digitized and fed into digital signal processor 33 for demodulation and further processing.

Examples of the T_1 distributions obtained for some of the fluids tested, using the NMR antenna, improved with a Faraday shield, are shown in Fig. 2.7 and Fig. 2.8 (Prammer, *et al*. 2002). The horizontal axis, "time," in Fig. 2.7 denotes the time elapsed between the saturation pulse and the readout sequence, the vertical axis indicates the signal amplitude in arbitrary units. These results are easier to interpret after inversion (Coates, *et al*. 1999) from the time domain to a T_1 domain, which is shown in Fig. 2.8. The single, sharp peak at 2–3 s is characteristic of water, the rounded peak in the "oil window" at 0.5–1 s indicates oil.

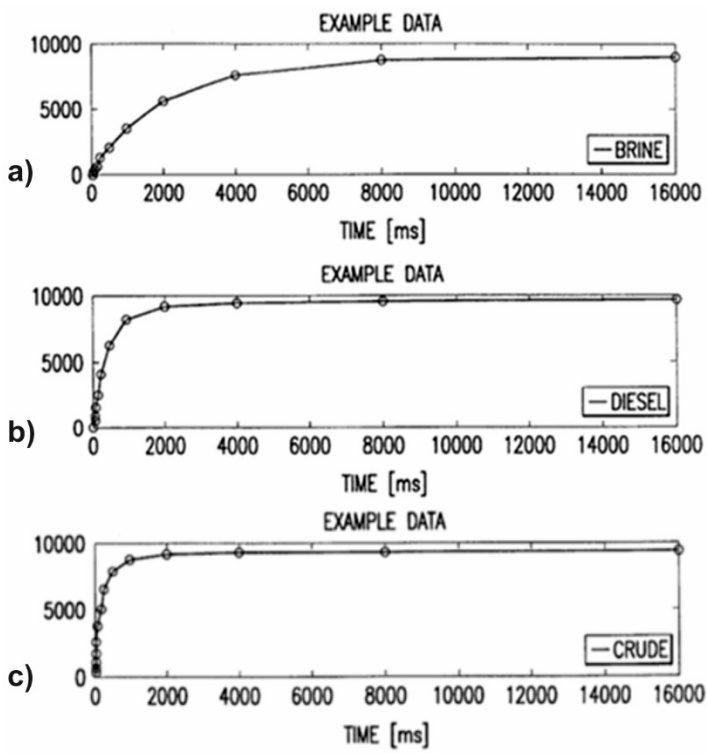

Fig. 2.7. Relaxation time T1 of different fluids measured in MRILab; a) brine, b) diesel, c) crude

The broad response from the crude oil in the bottom panel is characteristic for complex hydrocarbons. Shown in Fig. 2.8 are examples of the T_1 saturation-recovery data for three different fluids: brine, Diesel oil and crude oil. The positions of the spikes in the T1 distribution characterize the composition of the well fluid and its other parameters, and allow fast identification of the fluid's content by its so-called NMR signature. The implementation of the Faraday shield makes the NMR echo signal less dependant on the type of well fluid being tested. The high stability of the resonant frequency of the receive antenna, tuned to the Larmor frequency and combined with a high Q, increases the amplitude of the NMR echo signal and its resulting accuracy.

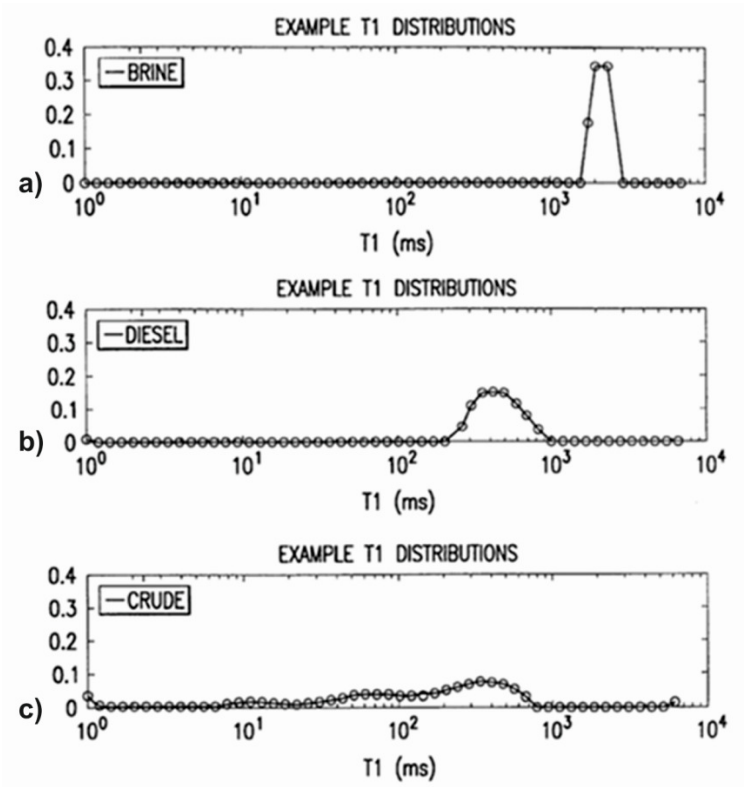

Fig. 2.8. MRILab test results for the T1 distribution in different fluids

Thus the NMR fluid analyzer MRILab can be successfully used for the testing of a wide spectrum of well liquids such as highly conductive salted water (brine), crude oil and diesel fuel.

2.3. Conclusions of Chapter 2

1. The placement of a slotted Faraday shield between the NMR antenna coil and the analyzed fluid decreases the resonant frequency shift to less than 1%.
2. This makes it possible to perform measurements without the use of a special tuning system to provide compensation for any detuning of the antenna.
3. This allowed the development of the first commercial in-well NMR fluid analyzer MRILab™.

3

Silicon MOSFET Drain-to-Source Resistance Behavior at High Temperatures

Silicon MOSFETs are the most commonly used power switches in high frequency power equipment. For specific applications, however, such as when they are intended to be used in NMR transmitters, manufacturer's specifications that are available do not cover temperature ranges over 150–175 °C, which is data that is very important for the development of NMR transmitters that need to operate at 175 °C ambient temperatures. Moreover, the drain-to-source resistance R_{dson}, which defines their conductive losses, is treated as a linear resistance with values, provided by the datasheet noted in Subchapter 1.5.2. In this chapter, the R_{dson} of such MOSFETs was investigated in temperature ranges of up to 200 °C as a function of temperature and drain current (Tyshko A., 2014; Tyshko A. *et. al.*,2013).

3.1. Correlation Between Drain Voltage Rating Value and Drain Resistance Temperature Coefficient

Commonly, the R_{dson} dependence on temperature is exponential with power index $P = 2.3$ (see Equation 5) for different power MOSFETs. To verify the applicability of this expression for MOSFETs with different maximum drain voltage ratings (V_{md}), the commercially available MOSFET database was analyzed.

For this purpose, the R_{dson} values for 25°C and 150°C were taken from each MOSFET datasheet and the ratio $K_r = R_{dson,150°C} / R_{dson,25°C}$ was calculated. Figure 3.1 shows the scatter plot of K_r and P_r against MOSFET maximum drain voltage rating V_{md}. The left vertical axis in this figure represents ratio K_r and right vertical axis represents the corresponding power index P_r based on Equation 1.5 and calculated as:

$$P_r = \frac{\log(K_r)}{\log(423/300)} = 6.7 \cdot \log(K_r) \tag{3.1}$$

where 423 and 300 are the test temperatures in Kelvin.

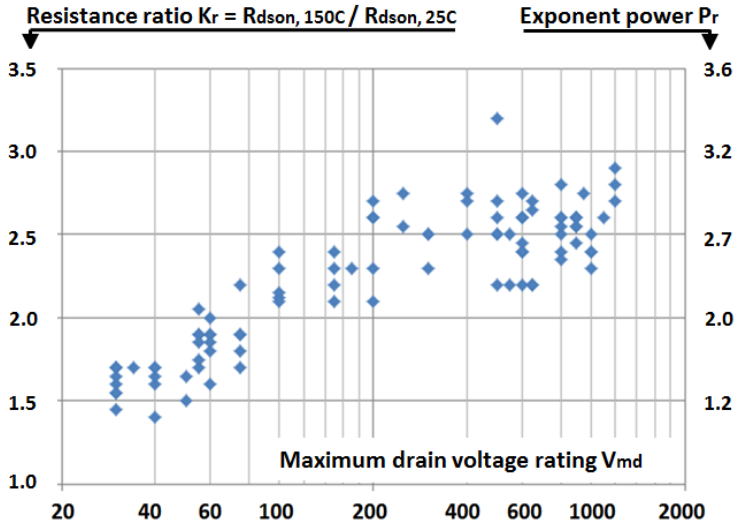

Fig.3.1. Scatter plot of K_r and P *vs*. MOSFET drain maximum voltage rating V_{md}

The data trend clearly indicates that K_r and exponent power P_r depend on the MOSFET maximum drain voltage rating V_{md} and that P_r changes from ~1.2 for low voltage transistors to ~3.0 for those transisters rated as having the highest drain voltage. The power value P_r in Equation 1.5. is close to 2.3 only

for certain MOSFETs with rated drain voltage V_{md} in the range from 200 V to 600 V. For practical reasons for the design of NMR transmitters operating in the 400 V to 600 V power bus range, the group of interest was narrowed down to the maximum drain voltage range of 600 V to 900 V.

3.2. Silicon MOSFET Experimental Test Setup

In this section, the experimental test setup used for the investigation of the drain-to-source voltage drop as a function of the drain current and the temperature in the extended range 25 °C to 200 °C in several MOSFETs is presented. The obtained results were used to calculate R_{dson} and to verify or update the currently used model (Locher, 1988). In order to decrease errors related to local heating by test currents, very short pulses with low duty cycles were used.

To measure simultaneously the pulsing drain current and the drain-to-source voltage, which is needed for the calculation of R_{dson}, the following test setup was designed and built. A block diagram of this setup is shown in Fig. 3.2. It consisted of a test heatsink (Fig. 3.3) onto which were installed 10 MOSFET units (*Q1–Q10*) with gate resistors *R1*, *R3* per each and a common non-inductive load resistor *R2* =1.0Ω for measuring the drain current with 1% accuracy. All assembly of these resistors and MOSFETs was placed in the oven. Because the testing temperature was at 200°C, all these components were capable of operating at high temperatures. The harness used Teflon isolated wires, SMT and wire-wound resistors and filter capacitors, which were tantalum wet slugs 220uF, 50V rated to 200°C and X7R ceramic capasitors 22 uF, 25 V. All the soldering was done using high temperature solder (SN-95). The

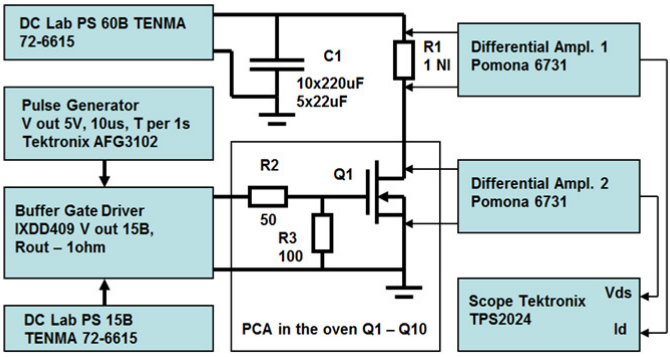

Fig. 3.2. Test setup for measuring the drain-to-source voltage drop *vs*. the drain current

differential voltage probes allowed for high accuracy measurements to be taken in the presence of high common mode signals in the harness. The test setup also contained a harness, a thermocouple and filtering capacitors *C1*, two laboratory DC Power Supplies TENMA 72-6615, pulse generator Tektronix AFG3102, gate driver IXDD409 IC, two differential voltage probes (Pomona 6731) and a 4 channel digital Scope TPS2024. These were used for measuring the drain voltage and drain current differentially.

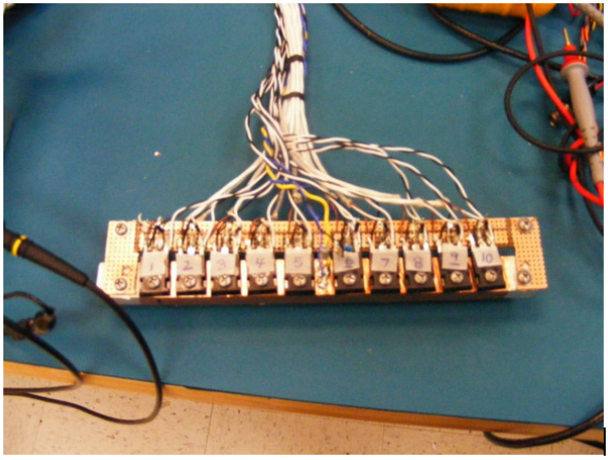

Fig. 3.3. Test heatsink with installed transistors

The test setup operated in the following way: The pulse generator produced 5 V logic level pulses of 10us duration and periods of 1s. This was done to keep the MOSFET dissipated power at minimal and to minimize the related die temperature rise over the temperatures measured by the thermocouple. The logic level pulse operated gate driver chip IXDD409, which was powered by the 15 V laboratory DC power supply and provided 15V gate pulses to the rotary switch used as the MOSFET selector (not shown). The 10 outputs of the rotary switch were connected to the harness and delivered pulses to the gates of the chosen MOSFETs. To prevent the harness from ringing all the gates, it had terminating resistors *R1* and *R3*. All the drains were connected in parallel and were powered through the wire-wound, non-inductive burden resistors *R2*, 1Ohm, 1%. Local filter *C1*, which included the electrolytic and ceramic capacitors, provided power to the MOSFETs being tested in the oven. Between pulses, this filter was charged from the regulated output of the same power supply.

When the gate pulse turned the MOSFET on, voltage from filter *C1* was applied to the burden resistor connected in series with the MOSFET, thus generating current.

The drain-to-source and the burden resistor voltages were then measured at the end of the 10us pulses, when transients settled (see Fig. 3.4). These were then averaged for 16 pulses per each of the 10 MOSFETs, and were then additionally averaged to produce one set of readings to minimize statistical deviation.

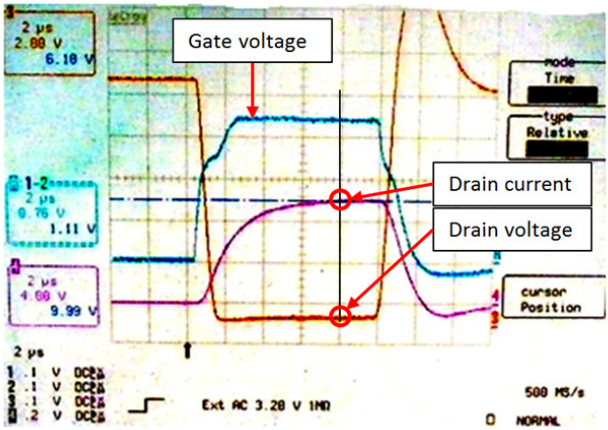

Fig. 3.4. Drain-to-source voltage, gate voltage and drain current waveforms

The heatsink with the mounted MOSFETs and other components, including the thermocouple, were then placed in the oven and soaked for 1 hour before the test at each temperature to maintain +/–1 °C accuracy.

3.3. Silicon MOSFET Test Results

Five types of power MOSFETs with drain voltage ratings V_{md} from 600 V to 900 V (IPB60R099, IPW90R120, STP11N80, SPP17N80 and the IXFH24N90P used for high temperature applications) were tested following this procedure. The resulting drain-to-source voltages V_d *vs*. two parameters: the drain currents I_d in amps and temperatures in degrees C are provided in Table 3.1 for the two MOSFETs with voltage ratings of 600 V and 900 V. The left column represents drain current I_d in amps and the top row represents the test temperatures in deg-

rees C. The values in the cells of Table 3.1 represent the measured drain-to-source voltages V_d in volts, which were needed for the calculation of the drain-to-source resistance $R_{dson} = V_d/I_d$. The crossed (X) cells correspond to either data, which could not be obtained because of the limited capabilities of the test setup or indicate obviously unacceptable voltage drops of the resulting power dissipation in the NMR transmitter.

Table 3.1. The drain voltage (in V) *vs*. drain current and temperature for the IPB60R099 and IPW90R120 MOSFETs

	IPB60R099,600V,0.099Ω						IPW90R120,900V.0.12Ω					
A\°C	**25**	**100**	**150**	**175**	**185**	**200**	**25**	**100**	**150**	**175**	**185**	**200**
5	**0.4**	**0.76**	**1.4**	**1.16**	**1.25**	**1.34**	**0.40**	**0.79**	**1.16**	**1.33**	**1.38**	**1.55**
10	**0.8**	**1.55**	**2.15**	**2.48**	**2.64**	**2.81**	**0.84**	**1.65**	**2.39**	**2.73**	**3.00**	**3.33**
15	**1.2**	**2.40**	**3.32**	**3.88**	**4.13**	**4.38**	**1.29**	**2.63**	**3.74**	**4.39**	**4.62**	**5.19**
20	**1.6**	**3.25**	**4.59**	**5.39**	**5.73**	**6.11**	**1.77**	**3.55**	**5.18**	**5.96**	**6.55**	**7.26**
25	**2.1**	**4.17**	**5.92**	**7.03**	**7.45**	**7.97**	**2.28**	**4.55**	**6.70**	**7.87**	**8.40**	**9.33**
30	**2.6**	**5.16**	**7.48**	**8.91**	**9.47**	**10.2**	**2.81**	**5.58**	**8.34**	**9.87**	**10.43**	**11.43**
35	**3.0**	**6.12**	**9.17**	**11.0**	**11.8**	**12.6**	**3.31**	**6.63**	**10.0**	**11.9**	**12.6**	**13.9**
40	**3.5**	**7.35**	**11.0**	**13.4**	**14.3**	**15.5**	**3.86**	**7.67**	**11.9**	**14.1**	**15.2**	**16.8**
45	**4.0**	**8.58**	**13.1**	**16.2**	**17.2**	**18.1**	**4.42**	**8.93**	**13.8**	**16.5**	**17.8**	**19.7**
50	**4.6**	**9.99**	**14.4**	**X**	**X**	**X**	**5.03**	**10.2**	**15.9**	**19.2**	**20.8**	**23.3**

This experimental data shown in Table 3.1 was used for the calculation of the normalized $R_{dson,n} = R_{dson}/R_{dson,25°C}$ where the reference drain-to-source resistance ($R_{dson,25°C}$) value was measured for the test currents listed in the MOSFET manufacturer's datasheets. For the IPB60R099 (IPB60R099, 2009) transistors, the test current 18 A was rounded to the closest 20 A. For the IPW90R12 (IPW90R120C3, 2009), the test current 23 A was rounded to 25 A. The results of these calculations are provided in the cells of Table 3.2 for both MOSFETs in a manner similar to that in Table 3.1.

Fig. 3.5. shows the values of the normalized $R_{dson,n}$, plotted against the drain current. The reference value of R_{dson} at 25 °C (circled) was obtained at drain test current 25 A. The trend line shows that the deviation from linear dependency is mostly less than 2%, which means R_{dson} *vs*. I_d dependence is very close to linear. In order to express this dependence as a mathermatical formula instead of an

actual drain current I_d, a normalized drain current $M_r = I_d/I_t$ was introduced. The value of test current I_t and the corresponding drain-to-source resistance $R_{dson,}$ at I_t at 25 °C are available from the manufacturer's datasheets. This formula is presented as:

$$R_{dson}\ (I_d) = R_{dson,It} \cdot [1 + a \cdot (M_r - 1)] \tag{3.2}$$

where M_r is the normalized drain current and a is the slope of the linear trend line. Equation 3.2 is valid at this one temperature. Fig. 3.6 shows how the normalized R_{dson} depends on I_d at different temperatures in a range from 25 °C to 200 °C. It thus can be seen that not only that the slope a, but also the starting point of each curve changes significantly with temperature.

Table 3.2. $R_{dson,n}$ *vs.* temperature and drain current

IPB60R099,600V,0.099Ω, test 18A							IPW90R120,900V.0.12Ω, test 25A					
A\°C	**25**	**100**	**150**	**175**	**185**	**200**	**25**	**100**	**150**	**175**	**185**	**200**
5	**0.94**	**1.79**	**2.45**	**2.73**	**2.94**	**3.15**	**0.88**	**1.74**	**2.55**	**2.92**	**3.03**	**3.41**
10	**0.98**	**1.82**	**2.53**	**2.92**	**3.11**	**3.31**	**0.92**	**1.81**	**2.63**	**3.05**	**3.30**	**3.66**
15	**0.99**	**1.88**	**2.60**	**3.04**	**3.24**	**3.44**	**0.95**	**1.93**	**2.74**	**3.22**	**3.38**	**3.80**
20	**1.00**	**1.91**	**2.70**	**3.17**	**3.37**	**3.59**	**0.97**	**1.95**	**2.85**	**3.27**	**3.60**	**3.99**
25	**1.01**	**1.96**	**2.79**	**3.31**	**3.51**	**3.75**	**1.00**	**2.00**	**2.95**	**3.46**	**3.69**	**4.10**
30	**1.02**	**2.02**	**2.93**	**3.49**	**3.71**	**4.00**	**1.03**	**2.04**	**3.05**	**3.62**	**3.82**	**4.19**
35	**1.03**	**2.09**	**3.08**	**3.70**	**3.97**	**4.25**	**1.04**	**2.08**	**3.15**	**3.75**	**3.97**	**4.39**
40	**1.04**	**2.16**	**3.23**	**3.95**	**4.22**	**4.55**	**1.06**	**2.11**	**3.27**	**3.90**	**4.18**	**4.63**
45	**1.06**	**2.24**	**3.42**	**4.24**	**4.50**	**4.73**	**1.08**	**2.18**	**3.38**	**4.04**	**4.36**	**4.83**
50	**X**	**X**	**X**	**X**	**X**	**X**	**1.11**	**2.24**	**3.50**	**4.22**	**4.57**	**5.14**

This is a result of power index P_r, which also depends on I_d. Thus in order to correct the starting point according to the temperature, power index P_d was modified by adding to it a component with normalized current M_r. This is shown in the following equasion:

$$P_d = b + c \cdot M_r \tag{3.3}$$

where b is a coefficient close to the original value 2.3 (Locher, 1988). The final corrected expression for R_{dson} as a function of the drain current and temperature,

based on the empirical formulas contained in Equations 3.2 and 3.3 is as follows:

$$R_{dson}(T, I_d) = R_{dson,It}\left[1 + a\left(\frac{I_d}{I_t} - 1\right)\right] \cdot \left(\frac{T}{300}\right)^{b+\frac{cI_d}{I_t}} \tag{3.4}$$

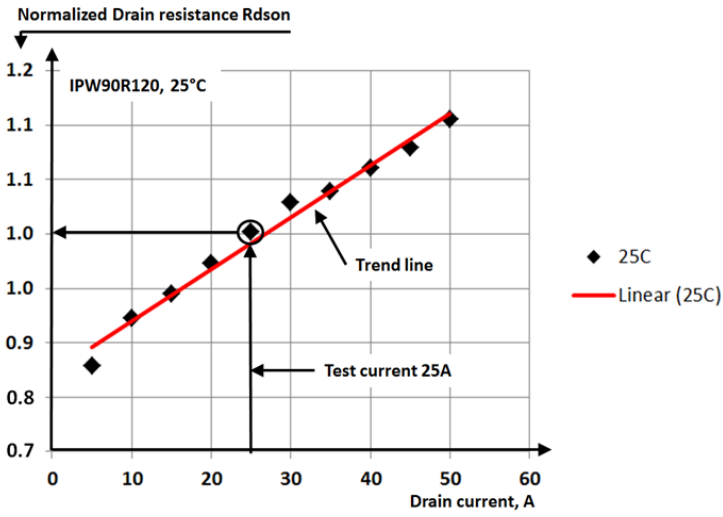

Fig. 3.5. Normalized R_{dson} dependency *vs*. drain current for IPW90R120 at 25 °C

All the coefficients, i.e. *a*, *b*, and *c*, can be obtained from the measured MOSFET data and then used in the transmitter design for calculating its conduction power dissipation.

For the validation of Equation 3.4, a fitting process, based on the maximum correlation between the actual measured data and the model data, was performed. The model coefficients were adjusted for minimum statistical deviation, using the weighted relative (σ_{rel}), calculated as the difference between the actual data X_i and the model predicted Y_i, divided by the average measured data. The final values of coefficients *a*, *b*, *c*, the correlation coefficient (*R*) and relative deviation are provided for all 5 MOSFETs in Table 3.3.

Fig. 3.7 illustrates the fitting results for two MOSFETs, one rated to 600 V (IPB60R099) and second to 900 V (IPW90R120), where the dots represent the measurement results and the smooth lines represent the simulated results according to Equation 3.4 and the coefficients from Table 3.3.

Table 3.3. Parameters obtained after fitting procedure using formula (3.4)

MOSFET	V_{dm}, V	I_t, A	R_{dson}, Ω	a	b	c	R	σ_{rel}
IPB60R099	600	18	0.09	0.07	2.6	0.32	0.999	0.017
STP11N80	800	5.5	0.35	0.04	2.6	0.32	0.991	0.059
SPP17N80	800	11	0.29	0.05	2.4	0.34	0.998	0.027
IXFH24N90	900	12	0.42	0.03	2.7	0.15	0.999	0.023
IPW90R120	900	26	0.12	0.08	2.7	0.35	0.999	0.025

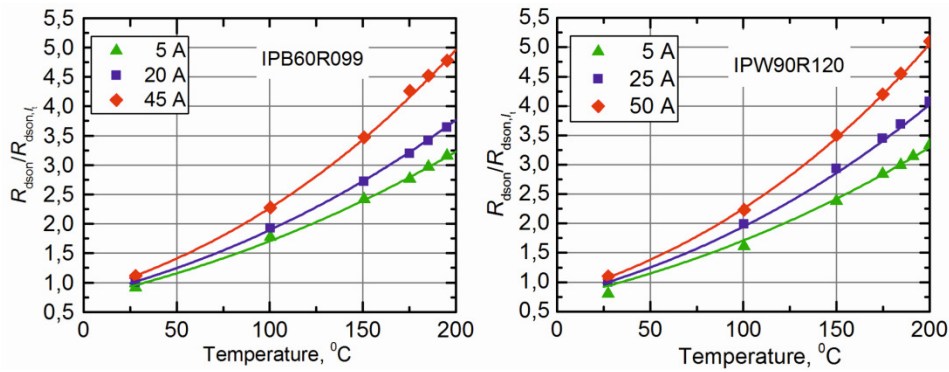

Fig. 3.7. Ratio R_{dson}/ $R_{dson,It}$ dependence *vs*. temperature and I_d current: measured (dots) and simulated (solid lines)

3.4. Conclusions of Chapter 3

1. This investigation demonstrates that the drain-to-source resistance R_{dson} of silicon MOSFETs depends significantly on the temperature and drain current and that at 200 °C, this can exceed its value at 25 °C by 3 to 5 times, depending on their voltage rating and the values of the drain current.
2. The improved R_{dson} behavioral model in which the two MOSFETs parameters (R_{dson}) and P were proposed to be a function of I_d was tested in the temperature range of 25 °C to 200 °C. It was proven that this model is valid with a correlation factor of better than 0.99 for the 5 different types of power MOSFETs.

4

Investigation of X7R Ceramic Capacitors

In this chapter, the multilayer X7R capacitors, which are used in these high power NMR transmitters as filters, were investigated for excessive losses and for ways to mitigate them. For this purpose, these capacitors' Equivalent Series Resistance (ESR) *vs*. their DC bias dependence was investigated along a voltage range from 0 V to 100 V, to their maximum capacitor voltage rating, and to the frequency range 0.1 MHz (Tyshko, A. and Balevicius, S., 2016).

4.1. Setup for the Investigation of X7R Capacitors' Eqivalent Series Resistance

The setup used for the investigation of these capacitors' ESR consisted of impedance analyzer WK 6500B and a standard 0 to 100 V DC power supply, which provided the test setup with the DC bias (shown in the schematic in Figure 4.1.) The two capacitors *C1* and *C2* were connected in series and the DC bias voltage was provided *via* resistors *R*1 and *R*2.

These multilayer X7R (CKG57NX7R2A106M500JH) ceramic capacitors 10 uF, 20%, 100 V, ESR 3.4 mΩ were tested at 100 kHz frequency and the maximum DC voltage rating 100V. These capacitors were choosen because of the wide use of this type of capacitor in high current converters, including NMR transmitters. Resistors RN55 100k, 1% were used as the bias resistors *R*1 and *R*2. The capacitors were placed in the low inductance test fixture of the impedance analyzer as shown in Figure 4.2. In the converter, all the AC currents are redirected along either path to the local capacitor energy storage. The generated heat was proportional to the capacitor ESR and the square of the AC current's RMS value.

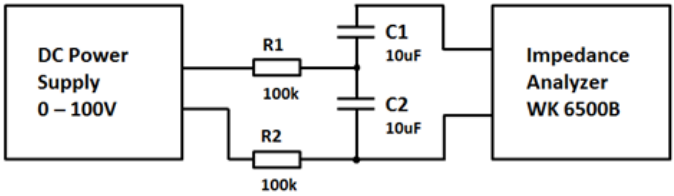

Fig. 4.1. Schematic of the test setup used for investigation of capacitors

Fig. 4.2. Outside view of capacitor test setup

The impedance analyzer WK 6500B was capable of measuring and displaying the two parameter *C* value and the ESR *vs*. frequency dependence along a frequency range of up to 20 MHz. The frequency range of interest for

the discussed application was limited to a 2 MHz maximum due to the fast decay of the amplitude of their higher harmonics.

4.2. Eqivalent Series Resistance Dependence on the DC Bias

It was observed that at zero DC bias, the ESR *vs*. frequency dependence (Fig. 4.3) was similar to that presented in Fig. 1.21. The measured ESR value 10 mΩ (encircled) was a sum of ESR of the two capacitors connected in series and the values of resistors R1 and R2, which provide the bias voltage from the DC power supply.

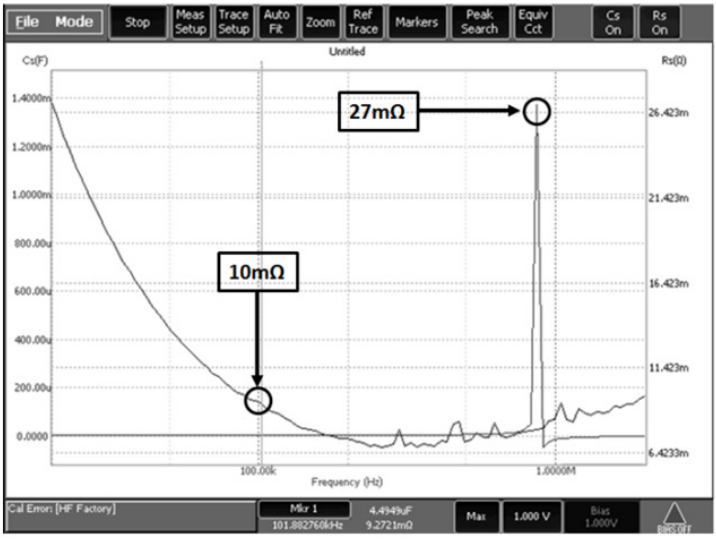

Fig. 4.3. ESR *vs*. frequency for CKG57NX7R2A106M500JH capacitors (no DC bias).

The capacitor model shown in Figure 1.22 predicted a single resonance of the lead inductance $L1$ with capacitance $C1$ at ~2 MHz. According to Fig. 1.22, this indicated that the capacitor ESR value had to be the same for all the harmonics in the range up to 1 MHz. However, the measured single resonance occurred at ~0.95 MHz instead of at 2 MHz, which can be explained as gue to the added lead inductance.

Application of the bias voltage significantly changed the behavior of the capacitance, which manifested itself by the appearance of additional ESR spikes at certain frequencies, such as at ~316 kHz, 398 kHz, 465 kHz and ~1 MHz. For

the capacitors measured at 465 kH, the ESR increased from 10 mΩ at 0 V DC to 26 mΩ at 20 V DC and to 62 mΩ at 50 V (Fig. 4.4) and up to 126 mΩ at 90 V (Fig. 4.5). This increase of the ESR, measured at 465 kHz, *vs*. applied DC bias voltage, is shown in Fig. 4.6. Close to the maximum rated voltage, the ESR of the capacitors increases by 16 times when compared to their original values at zero bias. This induces an increase of the power dissipation and a rise of capacitor temperature.

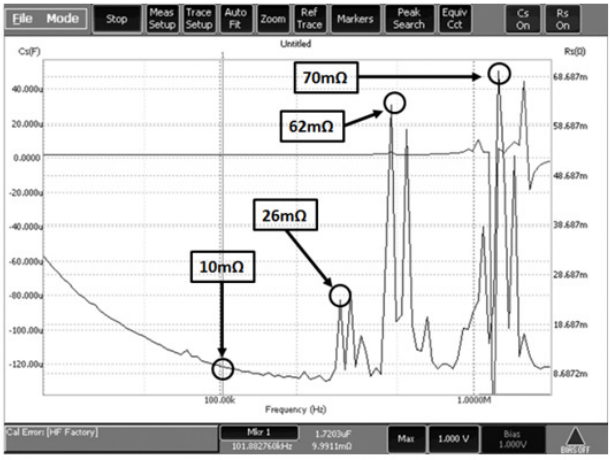

Fig. 4.4. ESR *vs*. frequency for CKG57NX7R2A106M500JH capacitors at 50V bias

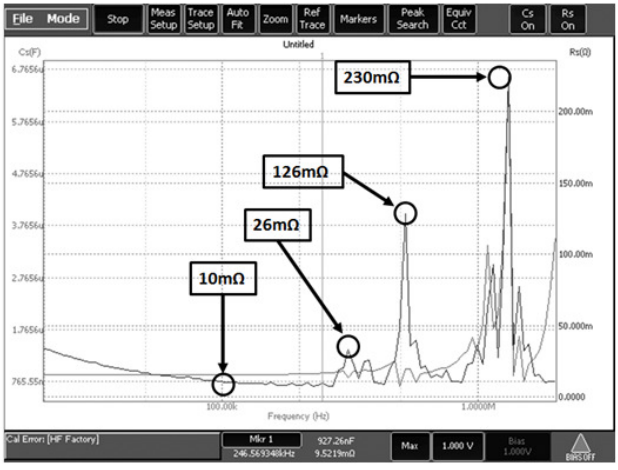

Fig. 4.5. ESR *vs*. frequency for CKG57NX7R2A106M500JH capacitors at 90V bias

The excessive heating of the X7R multilayer ceramic capacitors, which was observed during the mockup tests, can be explained by the polarization effect of the DC bias on the capacitors' BaTiO3/PbZrO3 PZT based material, which turned these capacitors into piezo-elements having multiple resonant frequencies. These were defined by the capacitor dimensions and their mechanical vibration modes.

These electromechanical losses occur when the AC current harmonics in the spectrum of the current flowing through the capacitor coincide with the resonant frequencies of the capacitor functioning as an electromechanical resonator. They are proportional to the DC bias voltage.

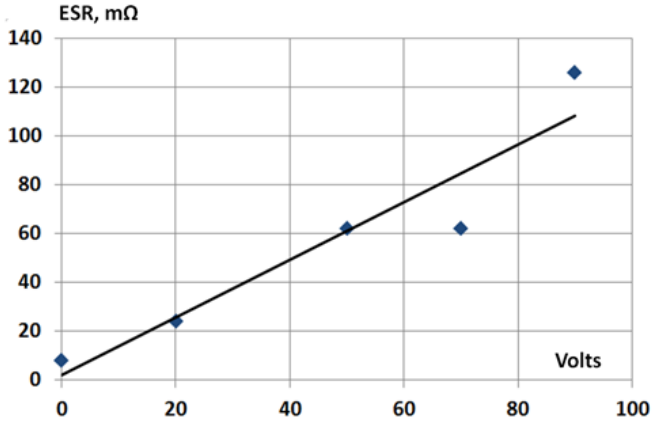

Fig. 4.6. ESR of CKG57NX7R2A106M500JH capacitors measured at 465 kHz *vs*. DC bias voltage

The following test was conducted to prove the mechanical vibration nature of the observed losses. The capacitors being tested were wrapped with tungsten filled silicon rubber, the material used to dampen these acoustic vibrations. This resulted in the resonant spikes being decreased by ~40%. At these resonant frequencies, the capacitors' ESR may be more than an order of magnitude higher than that indicated in the datasheet and the resulting losses can cause the capacitors to overheat and to produce thermal or mechanical failure (Tyshko*, et al.* 2016). This effect may also cause electromechanical failures (Dineva, *et al.* 2014) or, in the case where they are made of pre-polarized ceramic (with "frozen" electrical fields), they can be used for converting electrical energy into mechanical, such as in sensors, resonators, transformers and motors (Tichy, *et al*. 2010; Cho*, et al.* 2015; Sharapov, *et al.* 2014, Lavrinenko, 1975).

4.3. Conclusions of Chapter 4

1. It was observed that widely used X7R capacitors behave as piezoelectric resonators when biased with DC voltage. The tungsten filled silicon rubber dampened these acoustic vibrations up to ~40%. Such mechanical resonance increases these capacitor's losses and the probability of their failure.
2. The ESR of the capacitors increases by 16 times when compared to their original values at zero bias. For this reason it was recommended that multiple identical capacitors connected in parallel for AC current sharing could be used in order to mitigate the overheating and failures.

5

Nuclear Magnetic Resonance Transmitter with Cancelled Higher Harmonics

This chapter describes the design of a new NMR transmitter, operating at 175 °C ambient temperature. Its multi-module, multilevel topology, which combines the outputs of several identical power modules operating with 50% duty cycle at the fundamental frequency, provides the transmitter with the versatility needed for both low harmonic sine voltage synthesis and amplitude control (Tyshko, A., 2014). The cancellation of the higher harmonics of the output voltage is achieved by creating fixed relative phase shifts between the individual modules of the multi-module converter. The amplitude control employs the Chireix-Doherty outphasing modulation principle. The possibilities of a 20% increase of the tool signal to noise ratio (SNR), as compared to that of the two-module transmitter, has also demonstrated along with a significant increase in the tool's life expectancy.

The following is based on the author's original research, which was conducted at Halliburton, the leader in NMR technology for logging tools. During such research, it was found that the elimination of the third harmonic reduces from 3% to 10% the energy supplied to the transmitter (Tyshko, 2012). This re-

search also included simulations of such a transmitter's power dissipation, which were performed using expanded multi-module topologies and a simple phase shift as the control method. Three models of different complexity were used for this analysis. The simplest two-module transmitter (Case A) was used as the reference. The four-module (Case B) and eight-module (Case C) transmitters were used to investigate how the numbers of modules that are used influence the high harmonic effects (Tyshko, A. *et. al*., 2016). These results were then evaluated to determine the improvement of the transmitter's life expectancy and metrological capabilities *vs*. the transmitter's increased complexity.

5.1. The Multimodule Topology of the Nuclear Magnetic Resonance Transmitter

This analysis covers the results of the power switch dissipation related only to the conduction losses of the current measured at the transmitter output. Other internal power module losses, including those resulting from MOSFET switching and gate control, were outside the scope of this research.

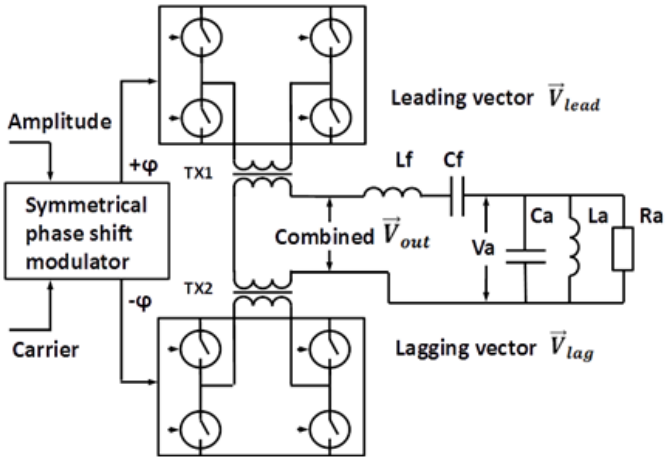

Fig. 5.1. Simplified schematic diagram of the reference transmitter (Case A)

The simplest NMR transmitter (Case A), shown in Fig. 5.1, was used as a reference and consisted of two power modules loaded with a resonant *LC* tank, representing the NMR antenna, and a modulator (Dent, 1998). Each of two modules produced 50% duty cycle pulses for a maximum value of the fundamental harmonic (F_0 = 500 kHz), which was used for the excitation of the antenna. The

shapes of the envelopes and amplitudes of the antenna excitation pulses (shown in Fig. 1.6) were controlled by means of a symmetrical phase shift +/–φ between the modules, which was induced according to the Chireix-Doherty outphasing method (Chireix, 1935; Doherty, 1936; Perreault, 2011).

The parameters used in the simulations of the transmitter Fig.5.1 were: operational frequency was 500 kHz, pulse envelope as determined by the Hanning function, duration was 100 us, DC bus voltage ranged from 450V to 600 V, antenna voltage was 1 kV peak, duty cycle was 20%, antenna inductance L_a = 1uH, capacitance C_a = 50 nF, filter L_f = 2 uH and C_f = 100 nF. The parallel resistor R_a was used for the simulation of the antenna's losses, defined by the expression $Q = R_a/\omega L_a$. For non-magnetic rock formations, Q depends upon the electrical conductivity of such formations, which can be calculated using simulation packages such as ANSYS, etc. (Doty, 2007). For most formations, Q is in a range from 10 to 100, and the R_a simulation values are 30 Ω for Q = 10, 90 Ω for Q = 30 and 300 Ω for Q = 100 (Tyshko, 2014). The transmitter (Case A) consisted of two full bridge modules, leading and lagging, and two combining transformers *TX1* and *TX2*. Each of the eight switches, forming two full bridge converters, were made of four paralleled MOSFETs with R_{dson} 0.1 Ω at 25 °C. Total number of used MOSFET switches was 32. At high temperature, the MOSFET R_{dson} of the IPW90R120 operating at 200 °C increased significantly and exceeded the 25 °C reference value by 4 times (see Fig. 3.7).

A block diagram of the proposed fully regulated, multimodule outphasing sine voltage DC/AC converter/transmitter is presented in Fig. 5.2. Transmitters Case B and Case C, which were based on the multimodule topology, employed a simple method for the sequential cancellation of their multiple higher harmonics, which combined the fixed α and variable φ phase shifts between two sets of individual modules, which are marked in Fig. 5.2 as Mod A (leading) and Mod B (lagging).

The "ladder" style output voltages of both the leading $\vec{V}_{lead}$ and lagging $\vec{V}_{lag}$ converters are shown in Fig. 5.3 as *V1* for Case A, *V2* for Case B and *V3* for Case C. Those output voltages were formed by combining 50% duty cycle module voltages using fixed phase shifts α_n for cancelling the higher harmonics.

To cancel the single higher harmonic number n from the combined output voltage of two modules, which produce identical pulses, these output voltages have to be shifted by the angle or delay time $\alpha(n)$ that is equal to the half period of this harmonic.

$$\alpha_{(n)} = \frac{\pi}{n}. \tag{5.1}$$

The amplitude V_n of harmonic n of the discussed 50% duty cycle output voltage of the full bridge modules, operating from DC bus V_B, can be described as:

$$V_n = \frac{4V_B}{\pi n}. \tag{5.2}$$

Such cancelling of the higher harmonics should be started with the lowest number, the 3rd, then the 5th and then the 7th if needed, as they are carrying significant power, sometimes exceeding the power of the fundamental frequency due to the resonances in the output circuitries.

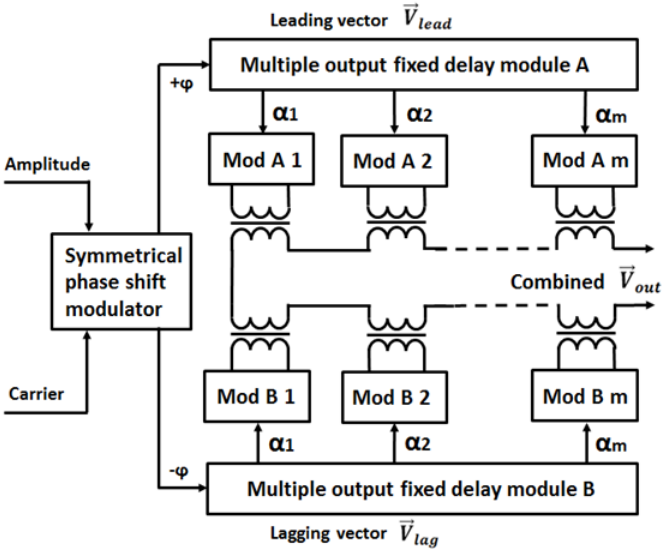

Fig. 5.2. Block diagram of the multimodule outphasing sine voltage DC/AC transmitter

The number M of the modules required to cancel the total K harmonics from the combined output is:

$$M = 2^K. \tag{5.3}$$

This means that when $K = 1$ (corresponding to $M = 2$), the 3rd harmonic is cancelled. If $K = 2$ (corresponding to $M = 4$), the 3rd and 5th harmonics are cancelled, and if $K = 3$ (corresponding $M = 8$), the 3rd, 5th, 7th harmonics are cancelled. An example of the formation of a ladder style voltage with cancelled 3rd, 5th and 7th harmonics based on the use of eight modules is shown in Fig. 5.3.

The multi-module transmitter combined output voltage vector $\vec{V}_{out}$ of the fundamental harmonic is then the sum of the vectors of the leading set of modules $\vec{V}_{lead}$ and the lagging set of modules $\vec{V}_{lag}$.

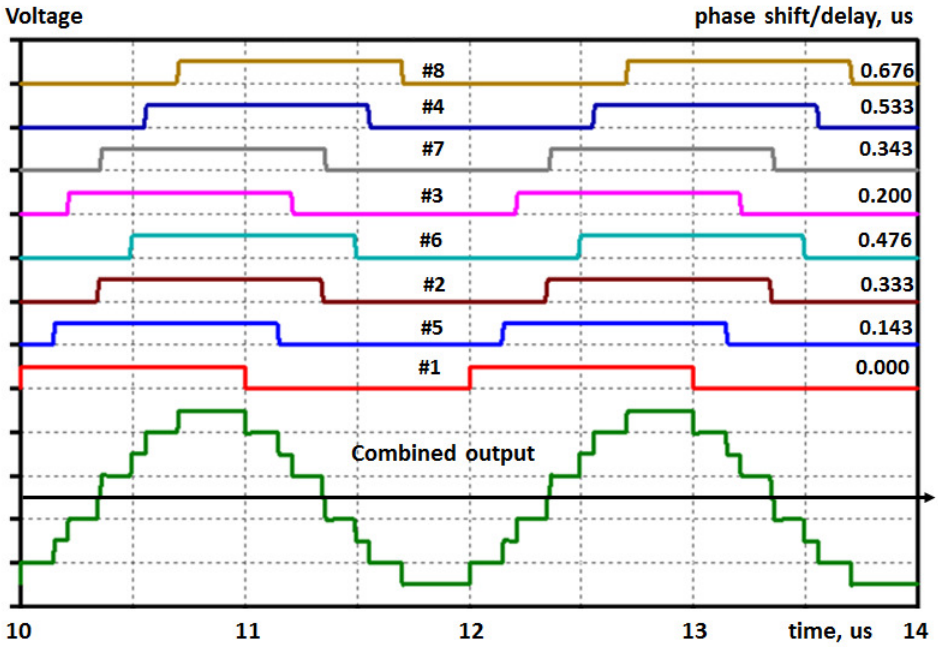

Fig. 5.3. Output voltages from eight properly phase shifted inverters which form the ladder style combined output

$$\vec{V}_{out} = \vec{V}_{lead} + \vec{V}_{lag}. \tag{5.4}$$

A detailed expression based on the individual module output vectors for the fundamental harmonic is:

$$\vec{V}_{out} = V_1 e^{j\omega t}\left(e^{+j\varphi}\sum_{m=1}^{m=k} e^{-j\alpha_m} + e^{-j\varphi}\sum_{m=1}^{m=k} e^{-j\alpha_m}\right) \tag{5.5}$$

where V_1 is the output amplitude of the first harmonic of each module, α_m is the individual module fixed phase shift in reference to the carrier signal, φ is the variable phase shift between leading lagging vectors used for amplitude control and ω is the frequency. The calculated fixed-phase shift α_m for each module is the inner product of the module assigned binary code c_m and array Φ_n containing the fixed phase shifts required for the elimination of the K harmonics:

$$\alpha_m = [c_m] \cdot [\Phi_n] \tag{5.6}$$

where m is the module number, c_m is the module assigned the binary code (actual module binary number ranging from 0 to $m - 1$) and n is the eliminated harmonic number. Matrix c_m range is $m \cdot K$. Fig. 5.4 shows this calculation algorithm in a graphic form for 8 modules and for the boxed simpler topologies (from original Case A to Case B with cancelled 3rd harmonic to Case C with cancelled 3rd and 5th harmonics).

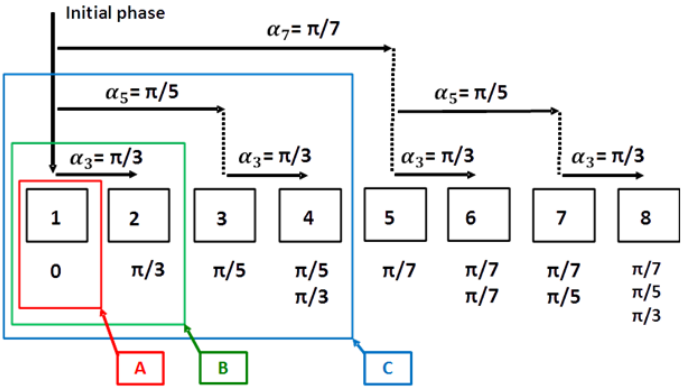

Fig. 5.4. Phase shift calculation algorithm for 3rd, 5th and 7th harmonics cancelling

Table 5.1 shows the results of the phase shifts α_m calculations for one unregulated DC/AC converter (leading or lagging) consisting of 8 modules producing quasi-sinusoidal voltage with cancelled 3rd, 5th and 7th harmonics.

Table 5.1. Calculated total module phase shift (look up table K=3)

Module No	Module code	n-th harminic phase shift in module			Total phase shift	Digital delay in units [9.5 ns]
m	c_m	n=7	n=5	n=3	α_m	
1	000	0	0	0	0	0
2	001	0	0	π/3	π/3	35
3	010	0	π/5	0	π/5	21
4	011	0	π/5	π/3	π/3+ π/5	56
5	100	π/7	0	0	π/7	15
6	101	π/7	0	π/3	π/3+ π/7	50
7	110	π/7	π/5	0	π/7+ π/5	36
8	111	π/7	π/5	π/3	2π/7+ π/5	71

In case of using the sets of digital delay lines Table 5.1 right column provides required delay line output numbers proportional to the required time or phase shift α_m per module, equal to 9.5 ns per unit for 500 kHz operation.

The additional phase shift φ_{ref} between the output voltages *V1* and *V3* shown in Fig. 5.5 and Fig. 5.7 is due to the buildup of the fixed-phase delays:

$$\varphi_{ref} = \frac{1}{2}\sum_{m=1}^{M} \alpha_m \tag{5.7}$$

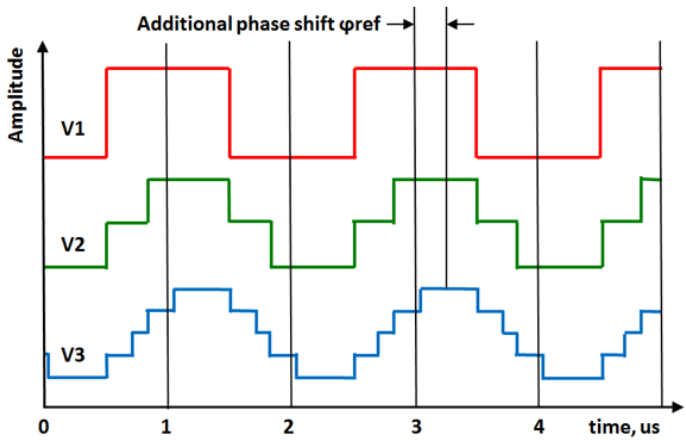

Fig. 5.5. Waveforms of converter voltages: the individual V1, V2 represents the combined phase-shifted voltages with cancelled 3rd harmonic, V3 represents the combined voltage with cancelled 3rd and 5th harmonics

It should be noted that each cancelled harmonic produces some losses in the fundamental one. Each time when a higher harmonic was cancelled, the two combined vectors had to be shifted as shown in Table 5.1, which resulted in a decrease of the amplitude of the output signal of the fundamental harmonic. Finally, after combining the outputs of all the *M* modules with V_1 original values of the fundamental harmonic and the cancelling of the *K* higher harmonics, the value of the fundamental harmonic V_1 decreased down to $V_{1,K}$.

$$V_{1,K} = M \cdot V_1 \cdot \prod_{n=3}^{K} sin\frac{\pi}{2}(1 - \frac{1}{n}) \tag{5.8}$$

where n = 3, 5, 7… and K is the total number of the cancelled harmonics. This decrease of the fundamental harmonic value $V_{1,K}$ was compensated by the proper correction of the combining transformer ratio (Tyshko, 2014). The above

described method produced an output voltage with cancelled harmonics that had a fixed amplitude. However, since this voltage is proportional to the unstable bus voltage, the transmitter needed the addition of the amplitude control based on the Chireix-Doherty outphasing method.

The algorithm of Case B transmitter operation is shown in Fig. 5.6.

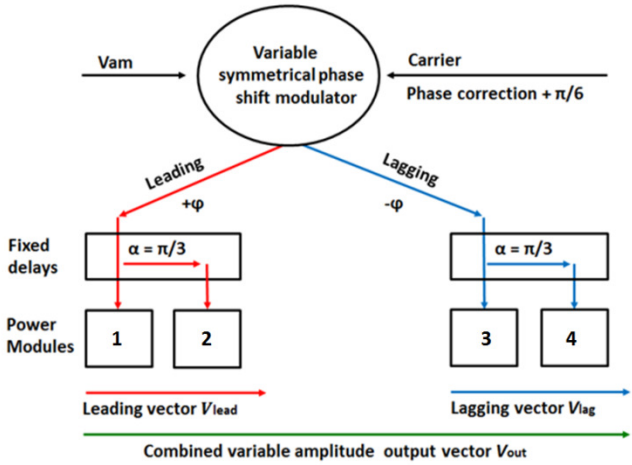

Fig. 5.6. Algorithm of Case B transmitter operation

The phasor diagram in Fig. 5.7 shows how this method works in the Case B transmitter, in which the four module output voltages $\vec{V}_1$ to $\vec{V}_4$ form the leading vector $\vec{V}_{lead}$ (in red), the lagging vector $\vec{V}_{lag}$ (in blue) and the combined output voltage $\vec{V}_{out}$ (in green). The output voltages of modules 1 and 2 have relative fixed phase shift π/3, which cancels the 3rd harmonic from their combined $\vec{V}_{lead}$. The same phase shift π/3 is set between modules 3 and 4, thus forming $\vec{V}_{lag}$ with the cancelled 3rd harmonic. The resulting transmitter output voltage $\vec{V}_{out}$ amplitude can be regulated from zero to $V_B \cdot 4\sin(\pi/3)$ by changing the variable phase shift $+\varphi$ and $-\varphi$ from zero to π/2 (1.3). During the amplitude modulation, the combined output voltage phase stays unchanged and remains equal to the fixed phase buildup $\varphi_{ref} = \pi/6$ (5.7). This phase shift can be corrected by the pre-set phase shift + π/6 of the sine carrier signal.

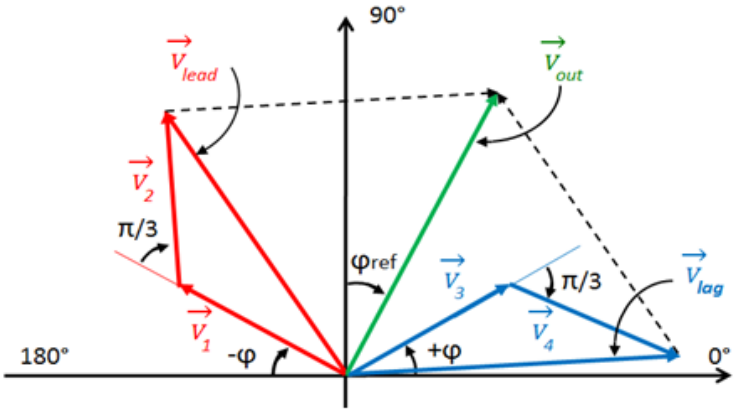

Fig. 5.7. Phasor diagram of Case B transmitter voltages

The algorithm of the Case C transmitter operation is shown in Fig. 5.8. The eight modules form a quazi-sinusoidal voltage with cancalled 3rd and 5th harmonics. The carrier signal corrected phase shift (5.7) is + (π/6 + π/10).

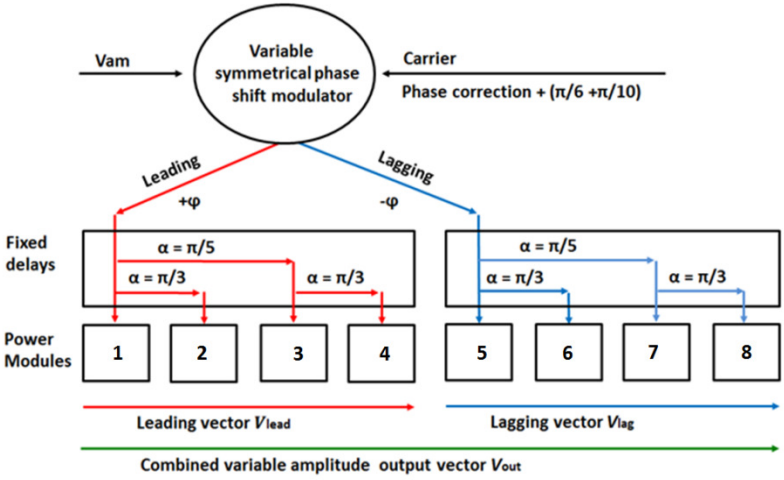

Fig. 5.8. Algorithm of the Case C transmitter operation with cancelled 3rd and 5th harmonics

In the ideal case, any desired level of combined output voltage spectral purity in the multimodule converter can be achieved by means of a simple replication of the above described process of harmonic cancellation, based on the switching at the fundamental frequency and the fixed phase shifts between the modules. In reality, however, the optimal number of cancelled harmonics and the required number of power modules depends upon other criteria, such as improved tool life expectancy, the required harmonic purity and the tool accuracy *vs*. cost and complexity.

5.2. Spectrum of the Output Current

For a comparative analysis, all three transmitters (Cases A, B, C) were operated under the identical loads shown in Fig. 5.1 and utilized 32 MOSFET transistors. The first simulated transmitter (Case A) used 2 modules with the switches consisting of 4 paralleled MOSFETs (see the schematic shown in Fig. 5.1 and the output voltage *V1* shown in Fig. 5.5). The second transmitter (Case B) used 4 modules with 2 paralleled MOSFETs in each and produced output voltage with the suppressed 3rd harmonic shown as *V2*. The third transmitter (Case C) employed 8 modules with a single MOSFET power switch in each and produced output voltage *V3* as shown in Fig. 5.5.

The transmitter output current was measured and the fast Fourier transformation (FFT) analysis was performed using the LTSpice software for the determining the module's output RMS current (total) and of the first three most important higher harmonics (3rd, 5th and 7th). Power dissipated per switch (P_{sw}) is proportional to the MOSFET resistance R_{dson} and the square of the drain RMS current, which can be calculated as the sum of the squares of all harmonics I_n or of the most important 1st to 7th. For practical calculations, the discontineous (∞) was limited to seven (7).

$$P_{\mathrm{sw}} = R_{\mathrm{dson}} \cdot \sum_{n=1}^{\infty} I_n^2. \tag{5.9}$$

The spectrum of the output current is provided in Fig. 5.9 and Table 5.2 for antenna with $Q = 30$ being its average value.

The total power, dissipated by the transmitter, consisting of multiple (2, 4 or 8) modules, and the values of the power per harmonic was calculated for T_j = 25 °C and a 20% duty cycle operation. As seen from Table 5.2, the power dissipation of 6.98 W of transmitter Case A decreased to 1.69W for Case B and to 1.53 W for Case C in comparison to the Case A with removed 3rd and 5th harmonics.

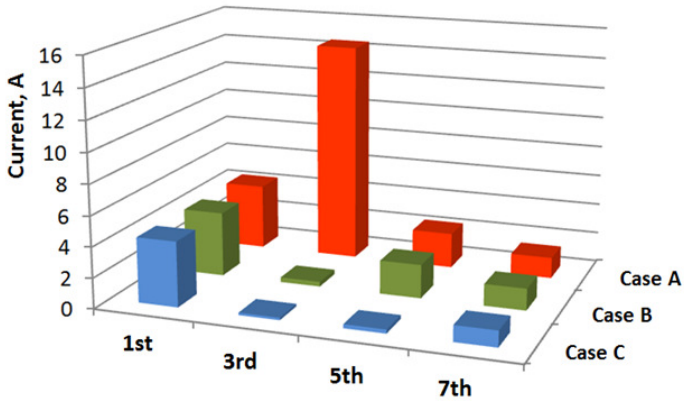

Fig. 5.9. Harmonics distribution for transmitter Cases A, B, C for $Q = 30$

Table 5.2. Current harmonics distribution and MOSFET power dissipation at 25 °C

Harmonics	1st	3rd	5th	7th	Total
Case A, 2 modules					
Harmonic current, A rms	4,39	14,67	2,34	1,44	18,68
2 modules power, W	0,39	4,30	0,11	0,04	6,98
Case B, 4 modules					
Harmonic current, A rms	2,50	0,19	1,28	0,82	4,60
4 modules power, W	0,50	0,00	0,13	0,05	1,67
Case C, 8 modules					
Harmonic current, A rms	1,50	0,06	0,08	0,34	2,19
4 modules power, W	0,72	0,00	0,00	0,04	1,53

Thus it could be concluded that the multimodule NMR transmitter using a combination of the fixed phase shift method for the cancellation of its higher harmonics and the outphasing method for the regulation of its amplitude allows the generation of a sine voltage with cancelled higher harmonics. This has up to 4 times lower power dissipation, related to conduction losses, when the number of modules is changed from 2 to 8.

5.3. Signal to Noise Ratio Improvement by Decreasing the Per Pulse Energy Consumption

The cancellation of the multiple higher harmonics decreases the energy per pulse consumed from the capacitive energy storage. This allows the production of more power trains (experiments) from the same stored energy. This ability to conduct more experiments related to the same formation layer after statistical processing of N_e experiments increases the signal power (P_{signal}) in proportion to the number N_e, and also the noise power (P_{noise}) in proportion to the square root of N_e. The resulting signal to noise ratio (SNR_r) and thus the resulting accuracy of the NMR data thus increases as the square root of the number N_e of the experiments that are conducted (Coates, et al., 1999):

$$SNR_r = \frac{P_{signal}}{P_{noise}} = \sqrt{N_e} * SNR_s \tag{5.11}$$

where SNR_s is the signal to noise ratio for a single experiment. This statement is valid when thermal, non-correlated noise is the dominant factor affecting the NMR signal. Table 5.3 illustrates the effect of changes in per-pulse energy on the resulting SNR tool due to the cancellation of the higher harmonic when operating from typical 80J capacitive storage.

Table 5.3. SNR *vs*. per-pulse energy consumption

Antenna Q=10, highly conductive	Case A	Case B	Case C
Energy delivered to antenna per pulse,J	0,633	0,600	0,596
Energy consumed from storage per pulse, J	0,690	0,637	0,627
Number of pulses	116	126	128
SNR relative to Case A, %	100	104	105
Antenna Q=30, low conductive			
Energy delivered to antenna per pulse,J	0,220	0,212	0,209
Energy consumed from storage per pulse, J	0,259	0,227	0,220
Number of pulses	309	353	363
SNR relative to Case A, %	100	107	108
Antenna Q=100, non conductive			
Energy delivered to antenna per pulse,J	0,067	0,065	0,064
Energy consumed from storage per pulse, J	0,104	0,077	0,072
Number of pulses	768	1046	1105
SNR relative to Case A, %	100	117	120

Taking the SNR of Case A as a 100% reference, the SNR of Cases B and C, depending on the formation conductivity and the resulting antenna losses, increases 17% and 20% respectively.

5.4. Increasing of Nuclear Magnetic Resonance Transmitter Life Expectancy

An additional benefit gained by cancelling the harmonics is the decrease of the power losses in the main transmitter components. Those components are switches *S1 – S8*, consisting of paralleled MOSFETs and power line filter capacitor set C_0 with the equivalent series resistance R_0 shown in Fig. 5.12. Simulation results of the equivalent circuit (Fig. 5.12) demonstrated that the cancellation of the higher harmonics significantly decreases the current flowing through filter capacitor C_0.

Both the leading and the lagging converters' bus currents flow through the bus filter capacitor set C_0 and dissipate the power proportional to the each capacitor's equivalent series resistance R_0 and square of current flowing through each capacitor. This classic approach is valid, however, only when the R_0 provided in the datasheets is the same for all the current harmonics. Experimental data for the X7R capacitors (Fig. 4.4) shows a significant increase in R_0 at the capacitors' mechanical resonant frequencies. Such NMR transmitters need to operate at multiple frequencies and at some of them, the filter current can in fact coincide with the capacitors' resonances. To keep the capacitors' power dissipation at the originally calculated acceptable level (marked in green), a cautious approach is recommended when multiple capacitors (capacitor strings) are used to share the filter ripple current.

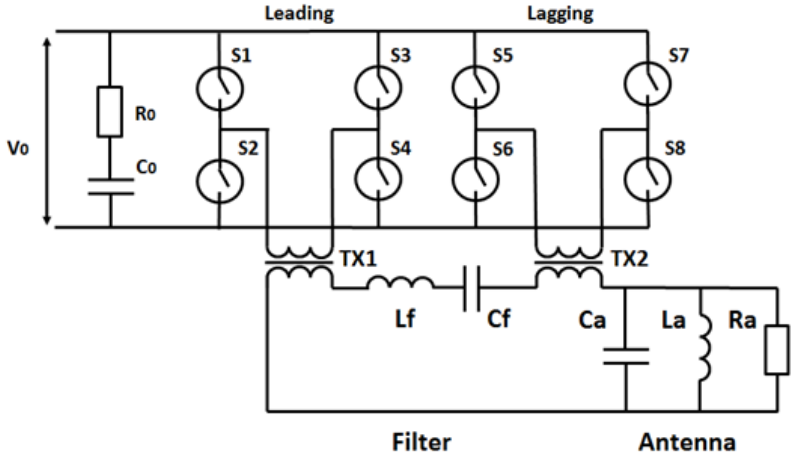

Fig. 5.12. Equivalent schematic of transmitter, filter and antenna

For the investigated capacitors used at 50% of their maximum rated voltage, the series resistance R_0 at 465 kHz increased by 8 times according to the data presented in Fig. 4.4 and Table 4.1. This required the 3 capacitor sets to be connected in parallel. Table 5.4 provides a comparative analysis of power dissipation in filter capacitor string of 12 capacitors having 50mΩ total resistance per pulse unit for the Case A and Case B transmitters operating with 100us Hann pulses. Row 1 shows capacitor current C_0. This is 28.5A for Case A and 17.8A for Case B with the cancelled 3rd harmonic. Row 2 shows the energy dissipated per pulse for Case A, which is 13.37mJ, and for Case B, which is 5.37mJ, respectively. It can be seen from Table 5.4 that reliable production of capacitor C_0 can be obtained for the Case A transmitter using a 3 capacitor string. For Case B, however, a string of only 2 capacitors is needed. Harmonic cancellation is also beneficial for saving space in the transmitter. This is done by decreasing the number of capacitors used in the filter, while maintaining the same reliability.

Table 5.4. Resonant losses in bus filter capacitors for Case A and Case B.

No	Parameters	Case A	Case B
1	Capacitor Filter current, 100µs Hann pulse, A	28.5	17.8
2	Energy dissipated with R_0 = 0.05Ω, out of resonance, mJ	13.37	5.37
3	Energy dissipated at resonance ($8R_0$), mJ	106.7	42.96
4	Energy dissipated by each of 3 capacitors paralleled, mJ	11.88	4.77
5	Energy dissipated by each of 2 capacitors paralleled, mJ	26.74	10.74

To assess the impact of the power dissipation and resulting temperature rise on the life expectancy t_v of the output stage MOSFET transistors, an approach based on the Arrhenius law was used:

$$t_v = C * e^{\frac{E_A}{kT}} \tag{5.12}$$

where T is the absolute temperature, E_A is the apparent activation energy (in general depending on T), C is a constant and k is the Boltzmann constant (Calixto, 2012). In such MOSFETs, the power switch die (junction) temperature T_j exceeds the ambient temperature T_A and the difference ΔT_j is proportional to the switch power dissipation Pj, which is the product of R_{dson}, the square of the RMS drain current I_d (20) and the thermal resistance junction to ambient R_{th}:

$$T_j = T_A + \Delta T_j = T_A + P_j \cdot R_{th} = T_A + R_{th} \cdot R_{dson} \cdot I_d^2. \tag{5.13}$$

It has been pointed out (Bayle, 2010), that the recommended value of the apparent activation energy E_A has increased from 0.35 eV (MIL-HDBK-217F notice 2, 1996) to 0.8 eV (MIL 217 plus, 2007) in just 15 years.

The accelerator factor AF (Calixto, 2012) or the ratio of the stressed tool life expectancy t_{v2} at elevated temperature T_j to the original t_{v1}, defined at temperature T_A, is represented by the expression:

$$AF = e^{\frac{E_A}{k}\left(\frac{1}{T_j} - \frac{1}{T_A}\right)}. \tag{5.14}$$

The accelerator factor AF was calculated using the recommendations of MIL 217 plus, 2007, where the activation energy of the silicon used in transistor E_A = 0.8 eV. The power dissipated at 175 °C ambient temperature and the resulting T_j were calculated for Cases A, B, C in two iterations based on the increase of the IPW90R120 R_{dson} provided in Fig. 3.7 and for the MOSFET drain harmonic currents shown in Table 5.2, Case B, according to the expression (5.13).

The results are shown in Table 5.5, Table 5.6 and Fig. 5.13 for R_{th} 0.2 K/W and 0.5 K/W. It is obvious that the cancellation of the 3rd and 5th harmonics makes it possible to decrease the conduction losses up to 2.3 times for R_{th} = 0.5 K/W.

Table 5.5. MOSFET temperature Tj for 175°C ambient for Cases A, B, C

	R_{th} = 0.2 K/W			R_{th} = 0.5 K/W		
Q	Case A	Case B	Case C	Case A	Case B	Case C
10	188°C	183°C	183°C	213°C	195°C	195°C
30	183°C	177°C	177°C	198°C	180°C	179°C
100	183°C	176°C	176°C	196°C	178°C	177°C

The life expectancy can be calculated by transforming formula (5.14) to $t_v = t_{v1} \cdot AF$, assuming that t_{v1} = 10 years at 175 °C. For R_{th} = 0.5 K/W, the temperature rises ΔT_j decreased from 38 °C to 20 °C and the accelerator factor AF increased from 0.2 to 0.414 for low Q loads. Thus according to data presented in Table 5.6 the life expectancy was increased from 4 years to 9.2 years when transmitter topology was changed from Case A to Case C in which higer harmonics were cancelled. The gain in the life expectancy is increased with the increase of the thermal resistance R_{th} junction to the ambient.

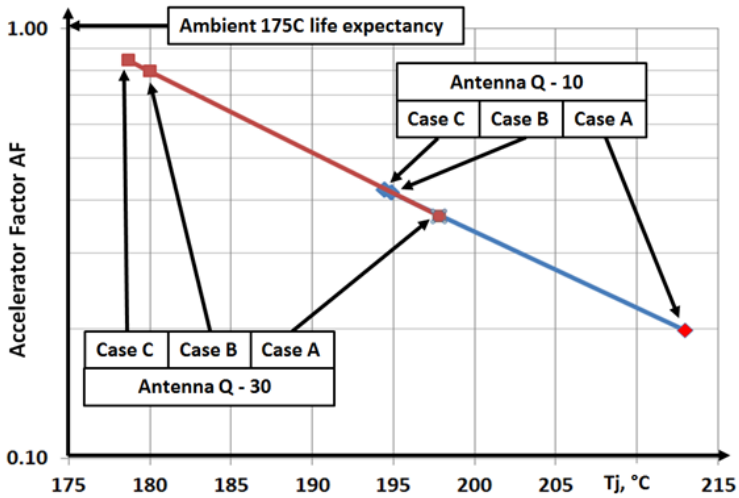

Fig. 5.13. Accelerator Factor AF for R_{th} - 0.5K/W vs. antenna Q = 10, 30 and transmitter topology (Cases A, B, C)

Table 5.6. Accelerator Factor AF for 175C ambient, Cases A, B, C

	R_{th} = 0.2 K/W			R_{th} = 0.5 K/W		
Q	Case A	Case B	Case C	Case A	Case B	Case C
10	0.562	0.709	0.705	0.199	0.422	0.414
30	0.695	0.912	0.932	0.366	0.796	0.844
100	0.711	0.943	0.967	0.400	0.863	0.920

In conclusion it has to be noted that the cancellation of the higher harmonics increases the NMR transmitter's life expectancy up to two times depending on the antenna losses and the transmitter to ambient thermal resistance.

5.5. Test and Evaluation of Transmitter with the Cancelled Third Harmonic

To verify that such third harmonics cancellation in fact works, a conventional NMR transmitter, used in the MRI Prime tool (Halliburton, 2008), was tested in an experimental setup (Fig. 5.14). This transmitter was connected to the potted filter/antenna module and tuned to 377 kHz, with Q = 10. An antenna interface 408 makes multiple antennas 404 for operation as a transmitting or receiving antenna. A RF transmitter 410 is coupled to the antenna interface 408 via a filter

412 to provide a RF pulse to antenna during excitation phase, while a receiver 414 is coupled to the antenna interface via a low-noise amplifier (LNA) 416 to detect echo signals during a measurement phase. The filter 412 passes a first harmonic of the transmit signal while attenuating higher harmonics. The LNA 416 operates as a bandpass filter at the same time it amplifies received signals to minimize any internal loss of signal-to-noise ratio. The receiver 414 down-converts the received signals to a frequency suitable for the data acquisition (DAQ) portion of the digital signal processor (DSP) 418.

The voltage was measured with a differential probe across antenna coil 404 and at the filter 412 input. The echo signals from Low Noise Amplifier 416 and receiver 414 were not processed and antenna interface 408 was simply bypassed. The test setup was connected to the uphole control module via interface 422. The test setup energy storage 424 was connected to the DC power source and the average consumed current was measured for the conventional configuration and after modification, while producing the same 1000 V peak amplitude pulses at the antenna.

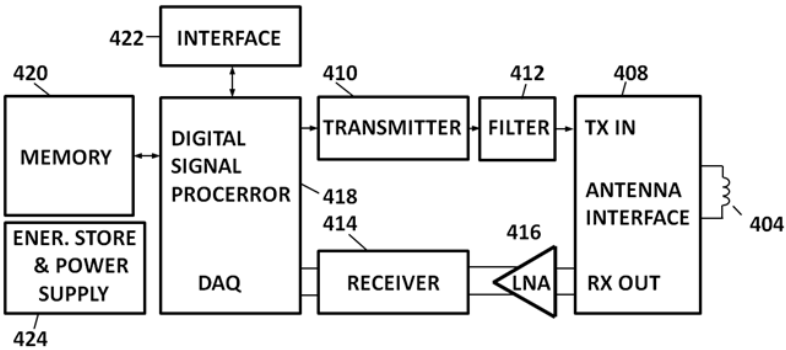

Fig. 5.14. Block diagram of tested NMR tool

Fig. 5.15 represents a more detailed block diagram of this transmitter. The DSP generated signals *I1*, *I2*, *Q1*, *Q2*, defined the excitation pulses, including the pulse envelope and the control codes, which determined the carrier oscillator 512 frequencies. The symmetrical pulse width modulator 502 also included comparators 514, 516, 524, 526 and the logic circuitries 518, 528 producing two 50% duty cycle signals S1 and S2, which operate the four half bridge power stages *P1–P4* within the output transformers 510, 520. The secondary windings of the transformers were connected in series and provided combined output voltage TX exciting load 412, which included the resonant antenna and the series filter. Transmitter output current 420 was measured with a high current AC/DC clip-on

current probe. The spectrum of the output current is presented in Fig. 5.16 (F is frequency).

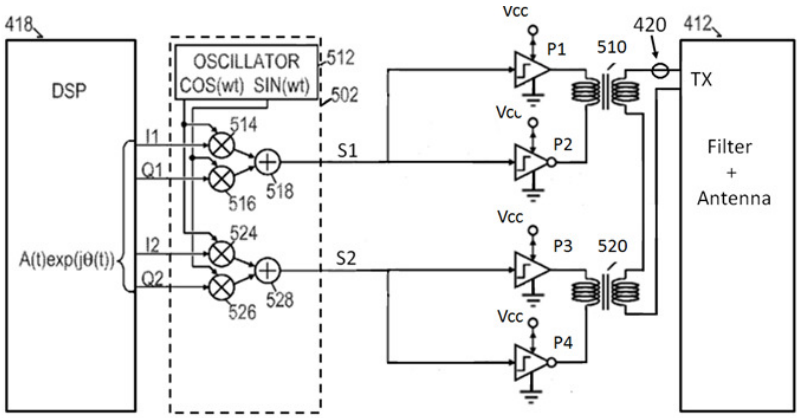

Fig. 5.15. Conventional NMR transmitter with antenna filter

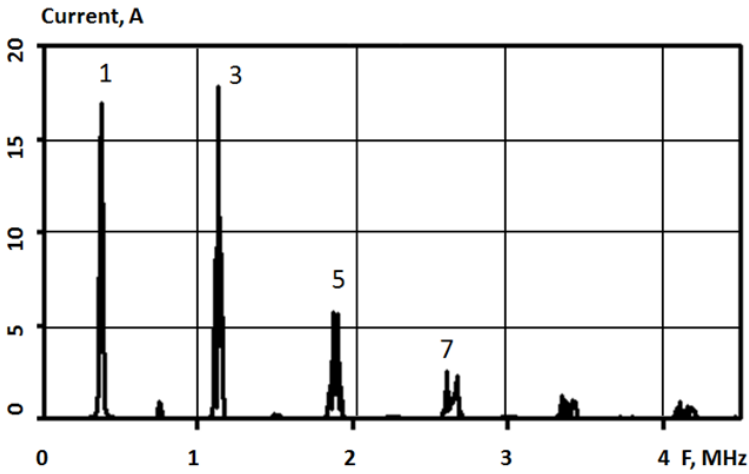

Fig. 5.16. Output spectrum of the Case A transmitter

The operation (simplified) of the symmetrical pulse width modulator is shown in Fig. 5.17, where the harmonic carrier signal *carrier* from oscillator 512 and the two opposite polarity modulation (envelope shaping) voltages V_{am+} and V_{am-} (inverted) turn on and off two triggers *Leading* S1 and *Lagging* S2 with the symmetrical phase shifts $+\varphi$ and $-\varphi$, depending on the modulation voltage.

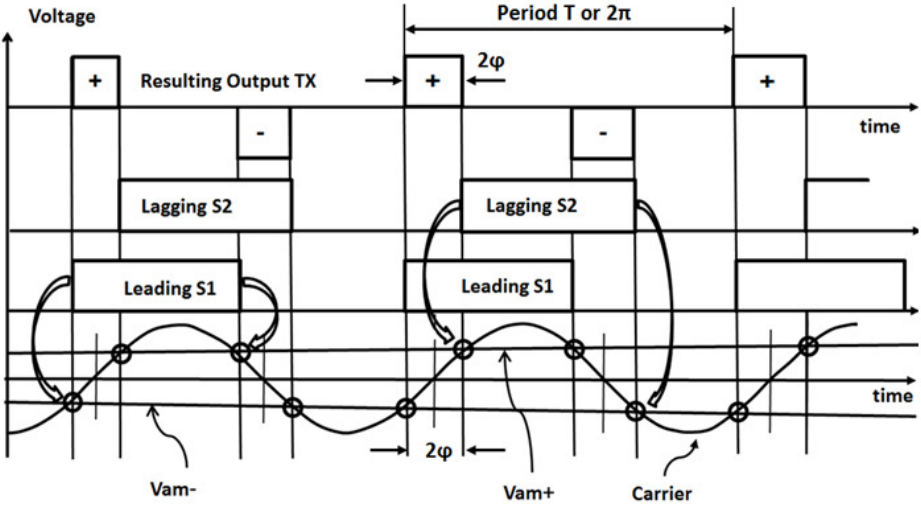

Fig. 5.17. Set of leading and lagging pulses

For zero modulation, the voltage phase shift φ is zero and *S1* and *S2* coincide in time. For maximum modulation, voltage equal to the carrier amplitudes *S1* and *S2* are in opposite phase ($2\varphi = \pi$). The output power stages *P1–P2* produced

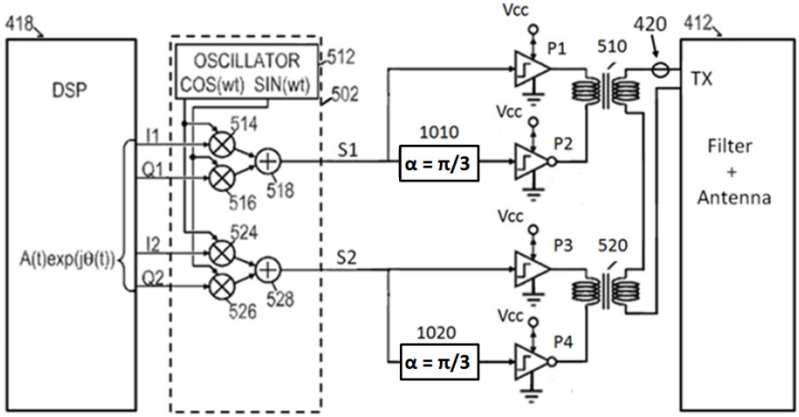

Fig. 5.18. NMR transmitter modification with 2 delay modules (1010, 1020)

50% duty cycle output voltage with leading phase $+\varphi$ and the power stages *P3–P4* produced 50% duty cycle output voltage with the lagging phase $-\varphi$. The

resulting Output voltage TX (Fig. 5.18) is shown in Fig. 5.19 as the Transmitter output.

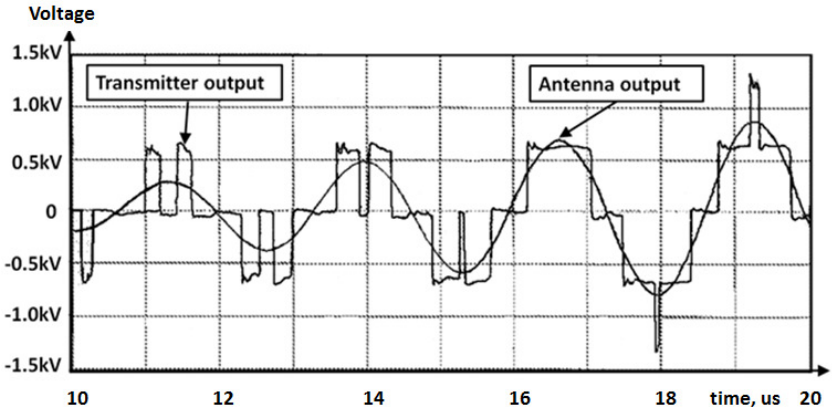

Fig. 5.19. Modified test transmitter (Case B). Output and antenna voltages

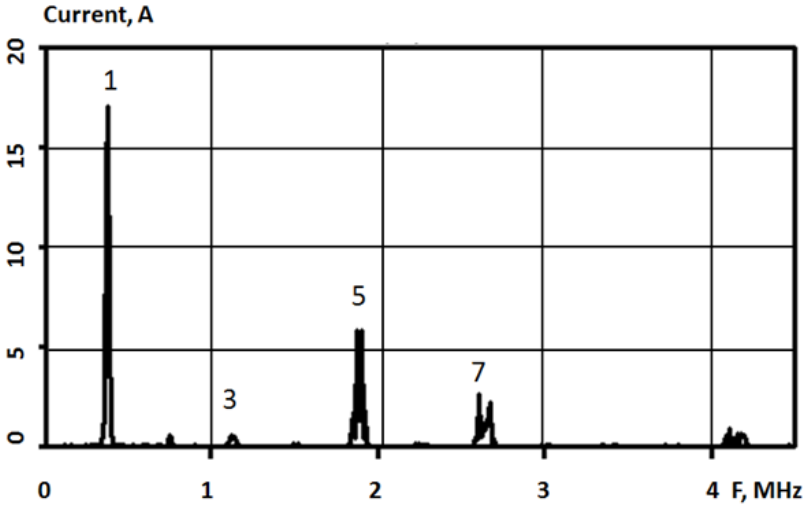

Fig. 5.20. Spectrum of transmitter (Case B) output current

The transmitter modification shown in Fig. 5.18 included the addition of the two fixed delay modules 1010 and 1020 in the control circuitries of the half bridges P2 and P4 and the combining output transformers 510 and 520 were replacement by new ones with increased turn ratios from 1: 1 to 1: 1.15 in order to

compensate for the partial loss of the fundamental harmonic according to expression (5.8).

For cancelling the third harmonic from the output voltage, the delay *Δt* had to be equal to the 1/6 period of operational frequency 377 kHz or 0.442 us. Digital delay lines were used for this purpose. The resulting voltage at the output of each of the two transformers 510 and 520 was similar to *V2* in Fig. 5.5.

The Case B transmitter combined output voltage, measured with differential voltage probes at the input TX of the filter, and the antenna output voltage are shown in Fig. 5.19. Spectrum of transmitter (Case B) output current is shown in Fig. 5.20 (F is frequency). The amplitude of the third harmonic in the transmitter output current was reduced from 17A to less than 0.7A, which indicates that the actual delay in the tested modified transmitter setup was not perfect.

Fig. 5.21 illustrates the variation of harmonics 1, 3, 5 and 7 amplitudes vs. the phase shift between power modules *P1* and *P2* (*P3* and *P4*) according to expressions (5.1) and (5.2).

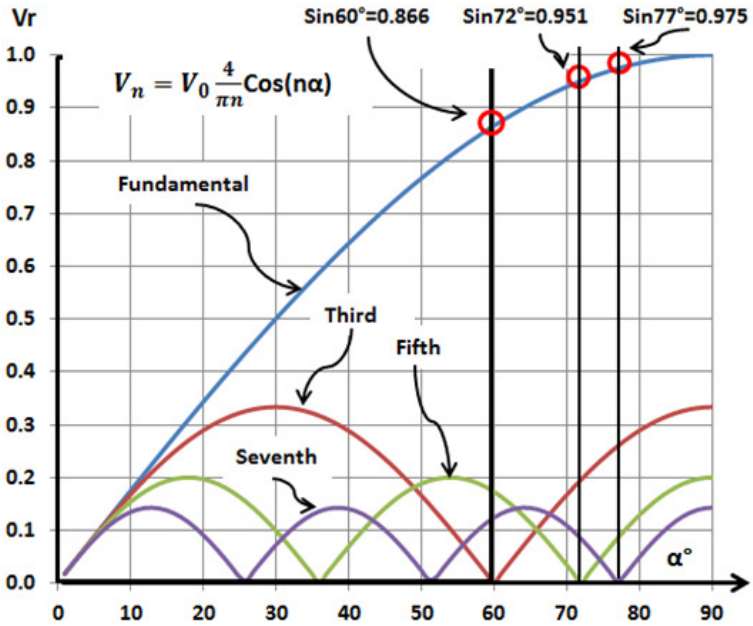

Fig. 5.21. Harmonics relative amplitude change *vs.* phase shift

Test setup shown in Fig. 5.18 had delay circuitries 1010 and 1020 corresponding to a π/3 phase shift, which means 1/6 of the period of the operating frequency. For the 377 kHz operation the period was 2.65 us and the delay had

to be 0.442 us. With an exact delay, the output voltage third harmonic V_3 could be fully eliminated, thus producing a zero third harmonic output current. But the residual 0.7 A, that is 0.041 of the original value, indicates that the actual delay differed from 0.442 us. To assess the error in the delay circuitry, the Fig. 5.21 diagram, describing the changing of the first four harmonics vs. the shift between two 50% rectangular pulses, was used. The third harmonic V_x is zero for shift $\pi/3$ (the first harmonic value drops to 0.866 of maximum). Any deviation α from this angle thus produces a third harmonic relative to the maximum value V_3 value X.

$$X = \frac{V_x}{V_3} = \sin 3\alpha = 0.041 \tag{5.15}$$

The deviation $\alpha = 0.78°$. For period 2.65 us, the mismatching delay was calculated as 5.8 ns. The relative delay error is only 0.013 or 1.3% of the total required delay, which fits manufacturer's tolerance 5% for the digital delay line DS1110 by Maxim.

Finally it could be concluded that cancellation of the third harmonic in the multimodule NMR transmitter was validated by experimentally testing the transmitters based on Case A and Case B topologies. Also it was obtained that the amplitude of the 3rd harmonic was decreased by 96% compared to the value of that in Case A.

5.6. Conclusions of Chapter 5

1. The multimodule NMR transmitter which uses a combination of the fixed phase shift method for the cancellation of output higher harmonics allows the generation of a sine voltage with up to 4 times lower power dissipation, related to conduction losses, when the number of modules is changed from 2 to 8.
2. The resulting SNR of NMR tool, operating from typical 80 J capacitive storage, due to the cancellation of the higher harmonic increases 17% and 20% respectively for SNR of Cases B and C in comparison to the SNR of Case A.
3. The cancellation of the higher harmonics of NMR transmitter with thermal resistance of junction R_{th} = 0.5 K/W decreases the temperature rise ΔT_j from 38 °C to 20 °C and increases the accelerator factor AF from 0.2 to 0.414 for low Q loads.This increase life expectancy from 4 years to 9.2 years even for high Q antenna loads.

4. The effect of third harmonic cancellation in the multimodule NMR transmitter was validated by experimentally. It was obtained that the amplitude of the 3rd harmonic was decreased by 96% in Case B compared to the value of Case A.

General Conclusions

Present study aims at improving of Nuclear Magnetic Resonance (NMR) downhole logging tools for the oil and gas industry. Based on the literature review, the following conclusions can be drawn:

1. The different dielectric parameters of the investigated well fluids induce detuning of internal NMR antenna during NMR downhole logging tools operation. It requires using of additional tuning system which would be able to mitigate the antenna detuning effect. However it increases the complexity of the tool and result in higher costs and less reliability of the NMR downhole logging equipment. For this reason a new NMR antenna detuning mitigation methods, which could to replace the existing ones are necessary.
2. The transmitter output current's higher harmonics produce excessive power dissipation, which increases the transmitter temperature and decreases the tool's reliability. The transmitter design needs to be reanalyzed and changed in order to decrease or to cancel out the higher harmonics eminating from the transmitter output voltage.
3. The high voltage power MOSFETs, used in NMR transmitter operate in a high temperature range exceeding the standard ratings provided by the manufacturers. MOSFET drain-to-source resistance R_{dson}, which defines

the conductive power losses, needs to be investigated at high (up to 200 °C) temperatures in order to create behavioral models of R_{dson} dependence on temperature and drain current.

4. Reasently the mechanisms responsible for failures in the ceramic capacitors due to the electrical fields were an object of intensive studies. The unexpected X7R ceramic capacitors failures used in NMR tools filters requires new analysis as to the actual behavior of such capacitors biased by DC.

In result of NMR tool investigation the following main conclusions were obtained:

1. An *innovative* design has been proposed for improving of NMR antenna by Faraday sheet. It enables significant (less than 1%) decrease in the resonant frequency shift when electrical parameters of formation fluid changes during NMR downhole logging tools operation. This makes it possible to perform measurements without the use of a special antenna tuning system and allows the development of the first commercial in-well NMR fluid analyzer.
2. New experimental data were obtained while investigating silicon MOSFET transistors drain-to-source resistance (R_{dson}) behaviour at high (up to 200 °C) temperatures. This investigation demonstrates that R_{dson} dependence on the temperature is nonlinear and at 200 °C its value increases 3 to 5 times compare to its value at 25 °C, depending on their voltage rating and the values of the drain current. The improved R_{dson} behavioral empirical expression in which the MOSFETs R_{dson} was proposed to be a function of two parameters: drain current I_d and temperature T. This expression was validated in the temperature range from 25 °C to 200 °C.
3. The investigation of X7R capacitors, widely used in NMR downhole logging tools, demonstrated that these capacitors behave as piezoelectric resonators which, when biased with DC voltage such mechanical resonances increase these capacitors' losses at resonant frequencies and the probability of their failure. It was recommended that in order to mitigate overheating and failures of these capacitors the single capacitor has to be replaced with capacitors bank consisting of several capacitors to share AC current.
4. The NMR transmitter conductive losses were investigated based on the analysis of the harmonics content of the transmitter output current. It was found that multimodule NMR transmitter which uses a combination of the fixed phase shift method for the cancellation of output higher harmonics allows the generation of a quazi-sinusoidal voltage with up

to 4 times lower power dissipation, related to conduction losses, when the number of modules is changed from 2 to 8 while maintaining the same number of transistors.

5. The resulting SNR of NMR tool, operating from typical 80 J capacitive storage, due to the cancellation of the higher harmonic increases 17% and 20% respectively for SNR of Cases B and C in comparison to the SNR of Case A.
6. The cancellation of the higher harmonics of NMR transmitter with MOSFETs thermal resistance to ambient R_{th} = 0.5 K/W decreases the temperature rise ΔT_j of these MOSFET from 38 °C to 20 °C and increases life expectancy for low Q loads from 2 to 4 years; for high Q loads this increases life expectancy from 4 years to 9.2 years.
7. The effect of third harmonic cancellation in the multimodule NMR transmitter was validated experimentally. It was obtained that the amplitude of the 3rd harmonic was decreased by 96% in Case B compared to the value of Case A.

References

Aki, A. *Back to the Future with LWD Technologies & Applications.* Kuwait : s.n., 2012. SPWLA.

Akkurt, R.; Bachman, H. N.; Minh, C. C.; Flaum, C.; LaVigne, J.; Leveridge, R.; Carmona, R.; Crary, S.; Decoster, E.; Heaton, N.; Hurliman, M.; Looyestijin, W.; Mardon, D.; White, J. *Advances in Magnetic Resonance.* 20th Anniversary, Winter 2008/2009, Oilfield Review, pp. 4–23.

Akkurt R., Cherry R. *System and methods for NMR signal processing without phase alternated pair staching. 6525534 B2* US, June 15, 2001.

AN9010 Application Note. *Fairchald Semiconductors Application Notes* 2000. https://www.fairchildsemi.com/application-notes/AN/AN-9010.pdf.

Antunes, F. L. M., Braga, H. A. C., Barbi, I., *Application of a Generalized Current Multilevel Cell to Current-Source Inverters,* IEEE Transactions on Industrial Electronics, Vol. 46, No. 1, Feb. 1999, pp. 31–38.

Atherton, Jay W. *Digital driver for fixed power amplifier. Patent US 4,673,887* USA, Jan 3, 1986.

AVX Corporation AT Series High Temperature MLCC – 200C and 250C Rated. June 2015. http://datasheets.avx.com/AT_Series.pdf.

AVX, X7R Dielectric, General Specifications http://datasheets.avx.com/X7RDielectric.pdf.

AVX Advanced Ceramic Capacitors for Power Supply, High Voltage and Tip and Ring Applications. http://catalogs.avx.com/AdvancedCeramicCapacitors.pdf.

Baker, R.; Bannister, L. *Electric power converter. Patent US 3,867,643 A* USA, 1974.

Bayle, F.; Mettas, A. *Temperature Acceleration Models in Reliability Predictions: Justifications and Improvements.* San Jose, CA, USA : Materials of "2010 Reliability and Maintainability Symposium, 2010. 2010 Reliability and Maintainability Symposium. pp. 1–7.

Bhagwat, P.; Stefanovic, V. Generalized structure of a multilevel PWM converter. *IEEE Trasns. Ind. Application.* 1981, Vol. 19, 6.

Blackman, R. B.; Turkey, J. W. The measurement of power spectra from the pint of view of communication engineering - Part 1. *The Bell System Technical Jornal.* January 1958, Vol. 37, 1, pp. 185–282.

Blinchikoff, H.; Zverev, A. *Filtering in the Time and Frequency Domains.* s.l. : J. Wiley & Sons, 1976. ISBN 0-471-95679-8.

Bloch, F. *Nuclear Iduction.*. s.l. : Physical Review Letters, October 1, 1946, Vol. 70, p. 460.

Calixto, E. *Gas and Oil Reliability Engineering: Modeling and Analysis.* s. l. : Gulf Professional Publishing, 2012.

Carrara, G.; Gardella, S.; Marchesoni, M.; Salutari, R.; Scuitto, G. A new multilevel PWM method: A theoretical analysis. *IEEE Transactions on Power Electronics.* July 1992, Vol. 7, pp. 497–505.

Cengelci, E.; Enjeti, P.; Singh, C.; Blaabjerg, F.; Pederson, J. New medium voltage PWM inverter topologies for adjustible speed ac motor drive systems. *Proceedings IEEE APEC' 98.* 1998, Vol. 2, pp. 565–571.

Ceramic Chip Capacitors, KEMET Electronics Corporation. http://www.digikey.com/en/pdf/k/kemet/ceramic-chip-capacitors?redirected=1.

Chireix, H. High Power Outphasing Modulation. *Proceedings of IRE.* 1935, Vol. 23, 11.

Cho, J-H,; Lee, Y-H.; Chun, M-P.; Kim, B-I. *Practical Application of Simulation Technique for the Resonators Using Piezoelectric Ceramics.* Korea : Korea Institute of Ceramic Engineering & Technology. http://cdn.intechopen.com/pdfs-wm/5384.pdf.

Clanton, B. New deepwater drilling rigs extend search for energy. *Houston Chronicle.* April 9, 2010.

Coates, G.; Xiao, L.; Prammer, M. *NMR Logging, Principles and Applications.* s.l. : Halliburton Energy Services, 1999.

Dahidah, M.; Konstantinou, G.; Agelidis, V. A Review of Multilevel Selective Harmonic Elimination PWM: Formulations, Solving Algorithms, Implementation and Applications. *IEEE Transactions on Power Electronics.* 2014, Vol. 99, pp. 1–16.

Darus, R.; Konstantinou, G.; Pou, J.; Ceballos, S.; Agelidis, V. *Comparison of Phase-Shifted and Level-Shifted PWM in the Modular Multilevel Converter.* Hiroshima, Japan : IEEE, 2014. IEEE International Power Electronics Conference (IPEC - ECCE Asia) 2014.

Dent, Paul Wilkinson. *Hybrid Chireix/Doherty amplifiers and methods. Patent US 6,133,788* USA, Apr 2, 1998.

Dineva, P.; Gross, D.; Muller, R.; Rangelov, T. *Dynamic Fracture of Piezoelectric Materials.* s.l. : Springer, 2014. ISBN 978-3-319-03961-9.

Divins, D. *Using Simulation to Estimate MOSFET Junction Temperature in a Circuit Application.* s.l. : International Rectifier, 2007. p. 18.

Doherty, W. H. A New High Efficiency Power Amplifier for Modulated Waves. *Proceedings of IRE.* 1936, Vol. 24, 9.

Doty, F. D. Probe Design and Construction. *Encyclopedia of Magnetic Resonance.* s.l. : John Wiley & Sons, 2007.

Du, Z.; Tolbert, L.; Chiasson, J. *Harmonic Elimination for Multilevel Converter with Programmed PWM Method.* [ed.] IEEE. *IAS.* 2004, pp. 2210–2215.

Energy Production. s.l. : International Energy Agency, 2014.

Final Report, US Army SBIR Phase II. *The influence of temperature on microelectronic device failure mechanisms.* Crofton, MD : Ramsearch Company, 1993.

Fortunato, M. *Temp and voltage variation of ceramic caps, or why your 4.7-uF part becomes 0.33uF.* s.l. : EDN Network, 11 26, 2012, ED Network.

Freedman, R. *Advances in NMR Logging.* s.l. : Sociaty of Petroleum Engineers, January 2006, Jornal of Petroleum Technology, pp. 60–66. SPE 89177.

Harris, F. J. On the use of windows for harmonic analysis with discrete Fourier transform. *Proceedings of the IEEE.* January 1978, Vol. 66, pp. 51–83.

Halliburton Recieves Contract with Estimated Value of $400 MillionFrom BP. *Business Wire.* April 28, 2003.

Halliburton, *Halliburton Wireline and Perforating Services,* p. 3–30, 2008. http://www.halliburton.com/public/lp/contents/Books_and_Catalogs/web/Wireline-and-Perforating-Catalog-2008.pdf

Ilves, K.; Antonopoulos, A.; Norrga, S.; Nee, H. P. A new modulation method for the modular multilevel converter allowing fundamental switching frequency. *Proc. IEEE ICPE (ECCE Asia).* June 2011, pp. 991–998.

Ilves, K.; Harnefors, L.; Norrga, S.; Nee, H-P. Analysis and Operation of Modular Multilevel Converters With Phase-Shifted Carrier PWM. *IEEE Transactions on Power Electronics.* Jan 2015, Vol. 30, 1, pp. 268–296.

IPB60R099 Datasheet. http://www.infineon.com/dgdl/Infineon-IPB60R099CPA-DS-v02_01-en.pdf?fileId=db3a304328c6bd5c0128ee28d90159e0.

IPW90R120C3Datasheet.http://www.infineon.com/dgdl/IPW90R120C3_1.0.pdf?folderId=db3a3043156fd5730115c736bcc70ff2&fileId=db3a3043183a955501185000e1d254f2

Kang, F.; Joung, Y-H. A cascaded Multilevel Inverter Using Bidirectional H-Bridge Modules. *Journal of International Conference on Electrical Machines and Systems.* 2012, Vol. 1, 4, pp. 448–456.

KEMETT502B106AG61107280.http://capacitoredge.kemet.com/capedge2/DataSheet?pn=T502B106M016AG61107280.

Kenyon, B.; Kleinberg, R.; Straley, C.; Gubelin, G.; Morriss, C. *Nuclear Magnetic Resonance Imaging - Technology for the 21st Century.*. Autumn, 1995, Oilfield Review, pp. 19–33.

Kleinberg, R.; Griffin, D.; Fukuhara, M.; Sezginer, A.; Chew W. *Borehole measurement of NMR characteristics of earth formations. 5,055,787* US, 08 27, 1986.

Konstantinou, G.; Pulikanti, S.; Agelidis, V. *Harmonic Elimination Control of a Five-Level DC-AC Cascaded H-Bridge Hybrid Inverter.* s.l. : 2010 2nd IEEE International Symposium on Power Electronics for Distributed Generation Systems, 2010.

Lavrinenko, V. *Piezoelectric Transformers.* Moscow : Energy, 1975.

Lai, J-S.; Peng, F. Multilevel Converters - A New Breed of Power Converters. *IEEE Transactions on Industry Applications.* May/June 1996, Vol. 32, 3, pp. 509–517

Li, B.; Yang, R.; Xu, D.; Wang, G.; Wang, W.; Xu, D. Analysis of the Phase-Shifted Carrier Modulation for Modular Multilevel Converters. *IEEE Transactions on Power Electronics.* Jan 2015, Vol. 30, 1, pp. 297–310.

Li, L.; Czarkowski, D.; Liu, Y.; Pillay, P. Multilevel Selective Harmonic Elimination PWM Technique in Series-Connected Voltage Inverters. *IEEE Transactions on Industry Applications.* Jan/Feb 2000, Vol. 36, 1, pp. 160–170.

Locher, R. *Introduction to Power MOSFETs and Their Applications.* National Semiconductor. 1988. Application Note. AN-558.

Magnetics, Inc. *Powder Cors Catalog.* 2015.

Material Grades, Samarium-Cobalt-Magnets. *Dexter Magnetic Technologies.* https://www.dextermag.com/material-grades/samarium-cobalt-magnets.

Menger, S. *Borehole NMR: Different Problems - Different Solutions.* Hannover, DE : s.n., 2003. LIAG Hannover.

Miller, M. *System for logging a well during the drilling thereof. US 5,280,243* USA, Dec 05, 1990.

Mills, M. P. *Unleashing the North American Energy Colossus: Hydrocarbons Can Fuel Growth and Prosperity.* Manhattan Institute for Policy Research. s.l. : "Power & Growth Initiative, 2012. Report #1.

Mohan, N.; Underland, T. M.; Robbins, W. P. *Power Electronics, Converters, Applications, and Design.* s.l. : Wiley & Sons, 2003.

Multilayer Ceramic Capacitors – Performance Characteristics, EIA Standard for ceramic dielectric capacitors RS-198C. http://www.cde.com/resources/catalogs/ceramperf.pdf.

Nurmi, R.; Standen E. *Carbonates, the inside story.*. Bahrain : s.n., 1997. Middle East Oil Show. SPE paper 37771.

Oil Price History and Analysis. s.l. : Energy Economist Newsletter, 2014.

Patel, H. S.; Hoft, R. G. Generalized Tecniques of Harmonic Elimination and Voltage Control in Thyristor Inverters: Part I - Harmonic Elimination. *IEEE Transactions on Industry Applications.* May 1973, Vols. IA - 9, May, pp. 310–317.

Petroleum Refining Industry. 2008. Application Data Sheet. ADS 2900-11/Rev. B.

PEEK (PolyEtherEtherKetone) Specifications. Boedeker Plastics, Inc.

Perreault, D. J. A New Power Combining and Outphasing Modulation System for High Efficiency Power Amplification. *IEEE Transactions on Circuits and Systems.* Aug 2011, Vol. 58, 8, pp. 1713–1726.

Popova, L.; Pyrhonen, J.; Ma, K.; Blaabjerg, F. *Modular Multilevel Converter solutions with few Sub-Modules for wind power application.* Lapeenranta, Finland : IEEE, 2014. 2014 16th European Conference on Power Electronics and Applications (EPE'14-ECCE Europe).

Prammer, M.; Bouton J.; Masak P.; Drack E.; Tyshko, A. *Magnetic Resonance Fluid Analysis Apparatus and Method. US 6,737,864* USA, March 27, 2002.

Prammer, M.; Bouton, J.; Masak, P.; Drack, E.; Tyshko, A. *Magnetic Resonance Fluid Analysis Apparatus and Method. US 7,164,267* USA, April 23, 2004.

Prammer, M.; Bouton, J.; Masak, P.; Drack, E.; Tyshko, A. *Magnetic Resonance Fluid Analysis Apparatus and Method*. Patent granted *EP1393096* EU, March, 28, 2003.

Rodriguez, J.; Lai, J-S.; Peng, F. Z. Multilevel Inverters: A survey of Topologies, Controls, and Applications. *IEEE Transactions on Industrial Electronics.* August 2002, Vol. 49, 4, pp. 724–738.

Rodriuez, P.; Bellar, M. D.; Munoz-Aguilar, R. S.; Busgues-Monge, S.; Blaabjerg, F. *Multilevel-Clamped Multilevel Converters (MLC).* 3, s.l. : IEEE, 2012, Vol. 27, pp. 1055–1060.

Rodrigues, J.; Bernet, S.; Wu, B.; Pontt, J.; Kouro, S. Multilevel Voltage-Source-Converter Topologies for Industrial Medium-Voltage Drives. *IEEE Transactions on Industrial Electronics.* December 2007, Vol. 54, pp. 2930–2945.

Sharapov, V.; Sotula, Zh.; Kunitskaya, L. *Piezo-Electric, Electro-Acoustic Transducers.* s.l. : Sprigner, 2014.

Sigal R. et al.. *Method and apparatus for improving the vertical resolution of NMR logs. 6541969 B2* US, December 15, 1999.

Singh, M. D.; Khanchandani, K. B. *Power Electronics.* New Delhi : Tata McGraw-Hill, 2001. p. 666.

Taicher, Z.; Shtrikman, S.; Paltiel Z.; Shporer, M. *Nuclear magnetic resonance sensing apparatus and techniques.*Patent *4,717,877* US, 01 05, 1988.

TDK Product Center, Datasheets, Multilayer Ceramic Chip Capacitors. https://product.tdk.com/info/en/ catalog/ datasheets/mlcc/automotive/megacap/en.pdf.

TDK Equivalent Circuit Model Library. https://product.tdk.com/info/tvcl/ecm/mlcc/commercial/midvoltage/c5750/ecm.pdf.

Tichy, J.; Erhart, J.; Kittinger, E.; Privratska, J. *Fundamentals of Piezoelectric Sensorics: Mechanical, Dielectric and Thermodynamical Properties of Piezoelectric Materials.* s.l. Springer, 2010.

Tolbert, L.; Peng, F.; Habetler, T. Multilevel converters for large electric drives. *IEE Transactions on Industrial Applications.* Jan/Feb 1999, Vol. 35, pp. 36–44.

Total Primary Energy Production. s.l. : Index Mundi, 2015.

Trainer, T. *Critique of the proposal for 100% renewable energy electricity supply in Australia.* s.l. : Brave New Climate, 2014.

Tura, V.; Harnagea, C.; Mitoseriu L.; Ricinschi D. *Dielectric and ferroelectric properties of multilayer ceramic capacitors with X7R characteristics.* s.l. : Fizika Solidelor - Fizica Teoretica, 1995–1996, Analele Stiintifice Ale Universitatii “Al. I. Cuza”, Vols. XLI–XLII.

UNIQ PMR Series NMR Spectrometr. http://www.mrr.com/uniq-pmr.htm.

Voltage Coefficient of Capacitors, Comparison and Solutions http://www.niccomp.com/help/VoltageCoefficientofCapacitors-032012-R1.pdf.

Wang, H.; Liserre, M.; Blaabjerg, F. Toward Reliable Power Electronics: Challenges H., Design Tools, and Opportunities. *IEEE Industrial Electronics Magazine.* June 2013, Vol. 7, 2, pp. 17–26.

Watson, J.; Castro, G. *High Temperature Electronics Pose Design and Reliability Challenges.* s.l. : Analog Device, Analog Dialog, 2012. pp. 1–7.

Zakis, J.; Vinnikov, D. *Implementation Possibilities of SMD Capacitors for High Power Applications.*, Tallinn : Tallinn University of Technology, December 2012, Electrical, Control and Communication Engineering, Vol. 1, pp. 18–23.

List of Publications by the Author on the Topic of the Dissertation

Papers in the Reviewed Scientific Journals

Tyshko, A.; Balevicius, S.; Padmanaban, S. *An Increase of a Down-hole Nuclear Magnetic Resonance Tool's Reliability and Accuracy by the Cancellation of a Multi-module DC/AC Converter's Output's Higher Harmonics*. IEEE Access, 2016, Volume 4, pp. 7912–7920.

Tyshko, A. *Excitation of the resonant loads with the multi-vector synthesized sinusoidal voltage decreases conduction losses and improves reliability.* Kiev, Ukraine: Electronics and Communications, Power Electronics Section, 2014, Vol. 19, pp. 37– 42, ISSN 1811-4512.

Tyshko, A. *Analyze MOSFET Parameters Shifts Near Maximum Operating Temperature.* s. l.: Electronic Design, Design Solution, May 2014, ISSN 0013-4872.

Tyshko, A.; Popov, V. *An estimation of conductivity losses for some power MOSFETs at elevated temperature.* Special Edition T2, Kharkov. Ukraine, August 2013, Energy Saving, Power Engineering, Energy Audit, Vol. 8 (114), pp. 19–25. ISSN 2218-1849 (in Russian).

Tyshko, A.; Popov, V. The High Frequency Inverters for NMR Tools Operating in the High Temperature Environment. *Technical Electrodynamics, Power Electronics and*

Energy Efficiency Magazine. Special Edition Vol. 2, 2012, pp. 46–48, ISSN 1607-7970 (in Russian).

Papers in the conference proceedings

Tyshko, A.; Balevicius, S. *Specifics of the X7R Capacitors Application in the High Frequency Inverters.* Kiev, Ukraine : IEEE, 2016, April 19 - 21. 2016 IEEE 36th International Conference on Electronics and Nanotechnology (ELNANO). pp. 267–270.

Tyshko, A. *DC to AC 3 Phase Modular Multilevel Conversion Using Chireix Outphasing Method.* Kiev, Ukraine : IEEE, 2015. Electronics and Nanotechnology (ELNANO), 2015 IEEE 35th International Conference. pp. 539–542.

Tyshko, A. *Multi-Vector Outphasing Provides High Power, Low Harmonics.* [ed.] IEEE Digital Library ELNANO-2014. Kiev, Ukraine : IEEE, 2014. Electronics and Nanotechnology (ELNANO), 2014 IEEE 34th International Conference. pp. 416–420.

Patents

Tyshko, A. *Multi-Vector Outphasing DC to AC Converter and method.* US 20160301327, 04 14, 2014. Patent Application. Published Oct 13, 2016.

Tyshko, A. *Enhanced Transmitter and Method for a Nuclear Magnetic Resonance Logging Tool*. Patent US 9,405,035, Jan 10, 2012, Patent granted Aug 2, 2016.

Prammer, M.; Bouton, J.; Masak, P.; Drack, E.; Tyshko, A. *Magnetic Resonance Fluid Analysis Apparatus and Method*. Patent US 7,164,267, USA, April 23, 2004

Prammer, M.; Bouton, J.; Masak, P.; Drack, E.; Tyshko, A. Magnetic Resonance *Fluid Analysis Apparatus and Method.* Patent granted EP1393096 EU, March, 28, 2003.

Prammer, M.; Bouton J.; Masak P.; Drack E.; Tyshko, A. *Magnetic Resonance Fluid Analysis Apparatus and Method*. Patent US 6,737,864 USA, March 27, 2002.

Summary in Lithuanian

Įvadas

Problemos formulavimas

Negilių lengvųjų naftos ir dujų sausumos telkinių mažėjimas, o taip pat padidėjęs šių vertingų energijos išteklių suvartojimas lėmė didesnes jų kainas pasaulinėje rinkoje. Ketinimai pakeisti iškastinį kurą atsinaujinančiais šaltiniais kol kas susiduria su rimtais sunkumais, todėl iškastinio kuro panaudojimas vis dar išlieka aktualus. Tačiau gręžimo išlaidų padidėjimas, ypač iš platformų jūroje ir iš specialių laivų, reikalauja padidinti gręžimo greitį bei matavimų tikslumą iš perspektyviausių skalūnų ir dujų telkinių. Todėl šioje pramonės srityje labai svarbus uždavinys yra greitai nustatyti angliavandenilių buvimą ir vietą bei ištirti jų savybes, tokias kaip klampumą ar geologinių formacijų poringumą. Klasikinis metodas, vertinant uolienų formacijų mėginius, yra prasmingas tik išimtiniais atvejais, nes trunka ilgą laiką ir yra brangus. Todėl netiesioginių, daugiausia elektrinių bei fizikinių metodų, kurie yra labiau patikimi ir tikslūs, panaudojimas yra labai perspektyvus.

Darbo aktualumas

Neseniai didelė pažanga, tiriant ir vertinant naftos ir dujų telkinių efektyvumą, buvo padaryta taikant branduolinio magnetinio rezonanso (BMR) technologiją. Iš gręžinių ruošinių BMR būdu galima nustatyti ir atpažinti laisvo vandens ir naftos buvimą geologinėse formacijose. Jie taip pat gali būti naudojami ir dujų iš angliavandenilių aptikimui. Šis

metodas yra naudingas, kai kiti metodai neduoda pakankamai tikslios informacijos. Tačiau BMR technologijos taikymas reikalauja unikalių galios elektronikos prietaisų veikiančių aukštoje (iki +175 °C) temperatūroje ir slėgyje, siekiančiame net 2000 atm. Dėl šios priežasties yra didelis BMR įtaisų poreikis, kurie galėtų atlikti tiesioginius geologinių formacijų tyrimus giluminio gręžimo metu su tikslumu ne mažesniu negu tas, kuris anksčiau buvo gaunamas naudojant kitus metodus.

Tyrimo objektas

Disertacinių tyrimų objektas yra BMR antena ir DC/AC keitiklis naudojamas įtaisuose, skirtuose dujų ir naftos žvalgybai giluminiuose gręžiniuose siekiant nustatyti angliavandenilių buvimo vietą ir jų savybes.

Darbo tikslas

Disertacijos tikslas yra apžvelgti BMR metodus, naudojamus vandenilio turinčių medžiagų (angliavandenilių ir vandens) paieškai bei ištirti galimybes patobulinti BMR anteną bei AC/DC keitiklį.

Darbo uždaviniai

Darbo tikslui pasiekti buvo sprendžiami šie *darbo uždaviniai*:

1. Ištirti, kaip naudojant Faradėjaus ekraną, įtaisytą tarp BMR antenos ir geologinės formacijos, galima sumažinti skysčio elektrinių parametrų įtaką BMR antenos rezonansinio dažnio kitimui.
2. Ištirti aukštos įtampos (600–900 V) silicio MOSFET tranzistorių santakos-ištakos varžos jautrumą temperatūros pokyčiams aukštose (iki 200°C) temperatūrose.
3. Ištirti X7R keraminių kondensatorių, naudojamų BMR naftos ir dujų gręžinių tyrimo įtaisų siųstuvų filtruose, netikėto perkaitimo ir gedimo priežastis bei pasiūlyti šių reiškinių įtakos sumažinimo būdus.
4. Ištirti, kaip aukštesniųjų harmonikų pašalinimas daugelio modulių siųstuvuose, naudojamuose BMR naftos ir dujų paieškos įtaisuose, leidžia padidinti įtaisų gyvenimo trukmę ir tikslumą.

Tyrimų metodika

Nagrinėjant darbo objektą taikyti šie metodai:

- teorinė daugelio modulių BMR keitiklio, veikiančio Chireix-Doherty fazavimo principu, amplitudės kontrolės analizė ir sparčioji modulio išėjimo įtampos ir srovės harmonikų Furjė transformacijos analizė, naudojant *LTSpice* programinę įrangą;
- aukštos įtampos (600–900 V) silicio MOSFET tranzistorių santakos-ištakos varžos jautrumo nuo temperatūros ir aukštųjų harmonikų pašalinimo daugelio modulių BMR siųstuve eksperimentinis tyrimas.

Mokslinis naujumas

1. BMR įtaisas naftos ir dujų paieškai, kurio antena turi Faradėjaus ekraną, patalpintą tarp antenos ir geologinės formacijos, pasižymi nauja tokių įtaisų konstrukcija. Šiai konstrukcijai būdingas didesnis antenos rezonansinio dažnio stabilumas kintant geologinės formacijos elektriniams parametrams, įtaisas turi mažesnius matmenis ir geriau tinka esant aukštam aplinkos slėgiui. Tai leidžia šį prietaisą panaudoti atliekant *in-situ* tyrimus giluminių gręžinių uolienose.
2. Naujasis daugelio modulių topologijos DC/AC keitiklis, kuris sudarytas iš kelių identiškų maitinimo modulių, veikiančių 50 % pagrindinio dažnio darbo ciklu, sumažina aukštesniųjų harmonikų sukeliamą nenaudingą galios išsiskyrimą keitiklyje, pagerindamas jo gyvenimo laiką ir tikslumą, kai BMR įtaisas veikia esant temperatūrai iki 175 °C.

Darbo rezultatų praktinė reikšmė

Panaudojus darbe atliktų tyrimų rezultatus, buvo sukurtas BMR įtaisas, skirtas giluminei naftos ir dujų paieškai, kurį sėkmingai panaudojo Halliburton Energy Services kompanija. Tai leido šiai kompanijai pasirašyti trejų metų, 400 milijonų JAV dolerių vertės sutartį su British Petroleum naftos žvalgybai Meksikos įlankoje. Halliburton L&P MRI-Lab(TM) naudoja šią branduolinio magnetinio rezonanso technologiją nuolat stebėti filtrato užterštumo lygį gręžiniuose, siekiant sumažinti laiką, reikalingą gauti švarų mėginį.

Ginamieji teiginiai

1. Faradėjaus ekranas, įrengtas tarp branduolinio magnetinio rezonanso (BMR) antenos ritės ir tiriamo skysto mėginio, sumažina antenos rezonansinio dažnio pokytį (iki 1% lygio), kintant mėginio elektrinėms savybės, iki lygio, kuris leidžia BMR įtaisui, naudojamam naftos ir dujų paieškai giluminiuose gręžiniuose, veikti be specialios elektroninės šio dažnio pokyčio kompensacijos sistemos.
2. Empyrinė aukštos įtampos silicio MOSFET tranzistorių santakos-ištakos varžos priklausomybė nuo temperatūros, kurioje įskaityta santakos srovės įtaka, gerai (koreliacijos koeficientas 0,991-0,999) aprašo silicio MOSFET tranzistorių elgseną temperatūrų intervale nuo 25 °C iki 200 °C.
3. Paveikus keraminius X7R kondensatorius, kurie yra plačiai naudojami BMR siųstuvų filtruose, pastovia įtampa, dėl piezoelektrinio efekto ženkliai (16 kartų esant 100V) išauga šių kondensatorių nuoseklioji ekvivalentinė varža. Dėl ko padidėja X7R kondensatorių galios nuostoliai ir išauga jų sugedimo tikimybė.
4. Daugelio modulių BMR antenos siųstuvas iš silicio MOSFET tranzistorių, naudojantis fiksuotos fazės poslinkio ir simetrinio kintamos fazės postūmio metodus, leidžia siųstuvo išėjimo signale pašalinti aukštesniąsias harmonikas. Modulių skaičiaus padidinimas šiame siųstuve nuo 2 iki

8 padidina įtaiso veikimo resursą nuo 4 iki 10 metų, o signalo-triukšmo santykį 20 %.

Disertacijos struktūra

Darbą sudaro įvadas, penki pagrindiniai skyriai, išvados, literatūros sąrašas, autoriaus publikacijų disertacijos tema sąrašas. Disertacijos apimtis – 98 puslapiai, 61 paveikslas ir 11 lentelių.

1. Literatūros šaltinių apie branduolinio magnetinio rezonanso įtaisus naftos ir dujų žvalgai giluminiuose gręžiniuose apžvalga

Pirmajame disertacijos skyriuje atlikta literatūros šaltinių disertacijos tematika apžvalga. Šis skyrius sudarytas iš penkių poskyrių. Pirmajame poskyryje glaustai aprašyti pagrindiniai būdai, naudojami įvertinant iškastinių angliavandenilių šaltinių dydį bei efektyvumą, pažymima, jog iškastinių angliavandenilių poreikis vis dar yra labai didelis, todėl ypatingą svarbą įgauna šių iškasenų žvalgybos sparta. Antrasis poskyris yra skirtas branduolinio magnetinio rezonanso (BMR) efektui ir jo pritaikymui angliavandenilių paieškai giluminiuose gręžiniuose. Jame pateikiamas BMR efekto aprašymas, BMR įtaisų veikimo principas, signalų gaunamų šio įtaiso pagalba apdorojimas bei duomenų interpretavimas. Trečiajame poskyryje pateikiama BMR įtaiso, skirto dujų ir naftos žvalgybai giluminiuose gręžiniuose, blokinė schema ir veikimo principai. Ketvirtajame – aptariamos „išorinės“ ir „vidinės“ konstrukcijos BMR antenos. Penktajame – aprašytas BMR siųstuvas ir svarbiausios jo dalys, t. y. keitiklių moduliai ir pagrindiniai komponentai – MOSFET tranzistoriai bei X7R tipo kondensatoriai. Šeštasis poskyris apibendrina literatūros šaltinių apžvalgą. Jame pažymima, jog BMR antena gręžinio gilinimo proceso metu gali patekti į įvairias geologinių formacijų sritis, turinčias skirtingus elektrinius parametrus, dėl to keičiasi jos rezonansinis dažnis ir nukenčia tyrimo tikslumas. Šios problemos sprendimui naudojama papildoma elektroninė sistema, kurios valdymas yra atliekamas iš įtaiso gręžinio paviršiuje. Tai padidina BMR įtaiso, skirto dujų ir naftos žvalgybai giluminiuose gręžiniuose, kainą ir gabaritus. Atkreipiamas dėmesys, jog BMR keitiklio aukštesniųjų harmonikų indėlis keitiklio išėjime yra didesnis, negu pagrindinės harmonikos, naudojamos BMR antenos sužadinimui. Tai padidina nenaudingą galios išsiskyrimą keitiklyje ir sumažina šio keitiklio veikimo resursą. Pažymėta, jog efektyvus būdas patobulinti BMR keitiklį yra šių aukštesniųjų harmonikų pašalinimas, modifikuojant keitiklio elektroninę schemą. Tačiau šio tikslo įgyvendinimui būtina gauti papildomų žinių apie silicio MOSFET tranzistorių veikimą aukštose (iki 200 °C) temperatūrose ir atlikti didelio sukaupiamo energijos tankio X7R tipo keramikinių kondensatorių, naudojamų BMR įtaiso filtruose, spektrinių nuostolių analizę.

2. Patobulinta „vidinė“ BMR antena su Faradėjaus ekranu

Antrajame darbo skyriuje pateiktas autoriaus pasiūlytas metodas, leidžiantis sumažinti „vidinės“ BMR antenos rezonansinio dažnio kitimą, kintant gręžinio geologinių formacijų elektrinėms savybėms. Šis skyrius sudarytas iš dviejų poskyrių: pirmajame – ištirta kaip BMR antenos rezonansinis dažnis priklauso nuo įvairių aplinkų, turinčių skirtingą dielektrinę skvarbą, antrajame – nagrinėjama BMR antenos konstrukcija, turinti papildomą Faradėjaus ekraną, patalpintą tarp BMR antenos ir tiriamos geologinės formacijos.

Geologinės formacijos įtaka BMR antenos rezonansiniam dažniui buvo tyrinėjama, naudojant įrangą, kuri buvo sudaryta iš BMR antenos patalpintos į indą, užpildytą aplinka (skysčiu ar dujomis) imituojančia geologinę formaciją, sinusoidinių signalų generatoriaus, veikiančio BMR antenos rezonansiniu dažniu, 5 V maitinimo šaltinio ir 400 MHz dažnių ruožo oscilografo skirto matuoti sistemos geologinė formacija-BMR antena rezonansinį dažnį. Geologinės formacijos dielektrines savybes atspindėjo indo, užpildyto įvairiomis medžiagomis, kurios dažniausiai aptinkamos naftos paieškos gręžinyje, elektrinė talpa *C1*. Buvo ištirtas ryšys tarp svyravimo kontūro, sudaryto iš BMR antenos (induktyvumas $L1$ = 1 μH) ir indo su geologinės formacijos imitacija, rezonansinio dažnio (f_R) ir *C1* vertės. Tyrimui buvo naudojamos šių geologinių formacijų imitacijos: oras (be skysčio), vanduo, nafta, mišinys sudarytas iš 50% naftos ir 50% vandens, ir didelio elektrinio laidumo sūrus vanduo. Tyrimų rezultatai pateikti S.2.1 lentelėje.

S.2.1 lentelė. (*L1*-*C1*) kontūro rezonansinio dažnio ir *C1* talpos vertės

C1 elektrinės talpos indo užpildas	Rezonansinis dažnis f_R, MHz	Talpa *C1*, pF
Oras	65,7	5,8
Nafta	58,7	7,3
Mišinys: 50 % naftos ir 50 % vandens	47,1	11,3
Distiliuotas vanduo	40,4	15,4
Sūrus didelio elektrinio laidumo vanduo	40,0	15,7

Kaip matyti iš šios lentelės, kintant geologinės formacijos elektrinėms savybės, papildoma (parazitinė) BMR antenos *LC* kontūro talpa kito net 3 kartus. Dėl to rezonansinis dažnis pakito net 40 %. Šio tyrimo rezultatai buvo panaudoti BMR antenos konstrukcijos tobulinimui papildomai įvedant Faradėjaus ekraną.

Geologinės formacijos įtaka BMR antenos parazitinei talpai buvo sumažinta, patalpinant šią anteną į tuščiavidurį varinį cilindrą. Tokios antenos konstrukcijos schematinis brėžinys pateiktas 1S paveiksle. Šiuo atveju BMR antenos spinduliavimo sukurtas elektrinis laukas neprasiskverbia į geologinę formaciją, esančią statmenoje antenos ašies kryptyje, o pagrindinė informacija gaunama tik iš srities, esančios antenos solenoido vidinėje ertmėje. Kaip parodyta S.2.2 lentelėje, tokiu atveju stebimas labai silpnas f_R ir *C1* kitimas, kintant geologinėms formacijoms.

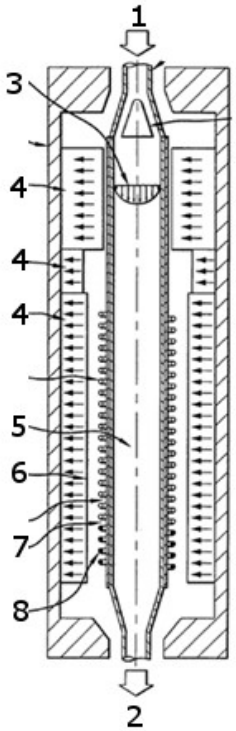

S 2.1 pav. BMR antenos su Faradėjaus ekranu konstrukcijos schematinis brėžinys. 1–2 skysčių įėjimas ir išėjimas, 3 – skysčių srautas, 4 – pastovieji magnetai, 5 – siųstuvo antena (solenoidas), 6 – matavimo kamera, 7 – Faradėjaus ekranas, 8 – siųstuvo-imtuvo antena

S. 2.2 lentelė. f_R ir *C1* kitimas BMR antenoje su Faradėjaus ekranu

C1 elektrinės talpos indo užpildas	Rezonansinis dažnis f_R [MHz]	Talpa *C1* [pF]
Oras	39	16,5
Nafta	38,4	17,1
Mišinys: 50 % naftos ir 50 % vandens	38,2	17,2
Distiliuotas vanduo	38,1	17,3
Sūrus didelio elektrinio laidumo vanduo	38,0	17,4

BMR įtaiso, skirto dujų ir naftos žvalgybai giluminiuose gręžiniuose, prototipas su patobulinta BMR antena, panaudojus Faradėjaus ekraną, buvo sėkmingai išbandytas Halliburton L&P MRILab(TM) kompanijos eksploatuojamuose naftos ir dujų telkiniuose. Bandymų rezultatai pateikti šio skyriaus antrajame poskyryje.

3. Silicio MOSFET tranzistorių ištakos-santakos varžos savybės aukštose temperatūrose

Siekiant sukurti DC/AC keitiklį, kuris galėtų būti sėkmingai panaudojamas maitinti BMR anteną ir veiktų aukštose (iki 175 °C) temperatūrose, buvo atlikti tyrimai siekiant nustatyti, kaip aukštos įtampos silicio MOSFET tranzistorių, kurie yra naudojami BMR keitikliuose, ištakos-santakos varža (R_{dson}) priklauso nuo temperatūros, kai pastaroji siekia net 200 °C.

Šiam tikslui buvo atlikta komercinių silicio MOSFET tranzistorių duomenų analizė, kuri parodė, jog 50–150 °C temperatūrų ruože R_{dson} eksponentiškai priklauso nuo temperatūros, o šios eksponentės rodiklis kinta nuo 1,2 (žemos įtampos tranzistoriams) iki 3 (aukštos įtampos tranzistoriams). Buvo gauta, jog šis rodiklis aukštos įtampos 600–900 V silicio MOSFET tranzistoriams, kurie geriausiai tinka BMR keitikliams, yra 2,3.

Siekiant eksperimentiškai nustatyti, kaip 600–900 V silicio MOSFET tranzistorių R_{dson} priklauso nuo temperatūros aukštose (iki 200 °C) temperatūrose, buvo sukurta tyrimo aparatūra, kurios blokinė schema pateikta S 3.1 paveiksle. Ši aparatūra leido ištirti kaip R_{dson} priklauso nuo temperatūros, vienu metu matuojant santakos-ištakos įtampą (V_d) ir santakos srovę (I_d).

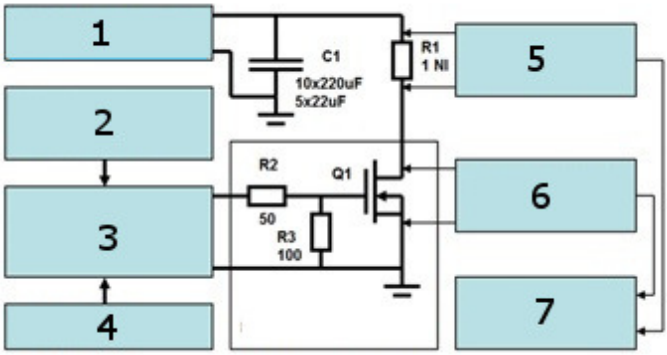

S.3.1 pav. Įtaiso, skirto silicio MOSFET tranzistorių santakos-ištakos varžos priklausomybės nuo temperatūros tyrimui, blokinė schema. 1 – pastovios įtampos šaltinis DC Lab PS 60B TENMA 72-6615, 2 – impulsų generatorius Tektronix AFG3102, 3 – impulsų stiprintuvas IXD 0409, 4 – pastovios įtampos šaltinis DC Lab PS 15B TENMA 72-6615, 5 ir 6 – diferencialiniai stiprintuvai Pomona 6731, 7 – oscilografas Tektronix TPS2024

Buvo nustatyta, jog santykinai žemose (25–100 °C) temperatūrose, esant pastoviai MOSFET tranzistoriaus temperatūrai, R_{dson} tiesiškai priklauso nuo I_d vertės, o R_{dson} priklausomybės nuo I_d kreivės statumas $\Delta R_{dson}/\Delta I_d$ yra tuo didesnis, kuo aukštesnė temperatūra, tačiau aukštose (iki 200 °C) temperatūrose R_{dson} nuo I_d priklausomybė tampa ryškiai netiesinė.

Buvo gauta, jog R_{dson} priklausomybę nuo I_d ir T plačiame temperatūrų ruože gerai aprašo empyrinė formulė (1):

$$R_{dson}(T, I_d) = R_{dson,It}\left[1 + a\left(\frac{I_d}{I_t} - 1\right)\right] \cdot \left(\frac{T}{300}\right)^{b+\frac{cI_d}{I_t}}, \quad \text{(S.3.1)}$$

čia $R_{dson,It}$ yra MOSFET tranzistoriaus santakos-ištakos varža kai tranzistorius yra 25 °C temperatūroje esant standartinei santakos srovei (I_t), *a, b* ir *c* yra empyrinės konstantos.

S.3.2 paveikslas demonstruoja tipiškas santykio $R_{dson}/R_{dson,It}$ priklausomybes nuo temperatūros, esant skirtingoms santakos srovių I_d vertėms. Ištisinės linijos gautos naudojant formulę (1), kuri buvo panaudota atliekant BMR keitiklio modeliavimą.

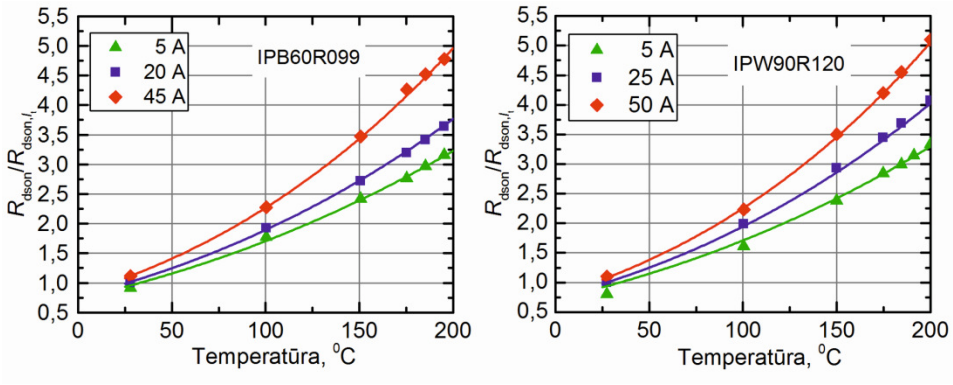

S.3.2 pav. Dviejų skirtingų MOSFET tranzistorių normuotos santakos-ištakos varžos ($R_{dson}/R_{dson,It}$) priklausomybės nuo temperatūros, esant skirtingoms I_d vertėms. Normuota į $R_{dson,It}$ vertę, esant standartinei tranzistoriaus srovei 20 A (a) bei 25 A (b), esant 25 °C temperatūrai. Matavimų duomenys atvaizduoti taškais – ištisinė linija gauta naudojant formulę (1)

4. X7R keraminių kondensatorių tyrimas

Šiame skyriuje pateikiami daugiasluoksnių keraminių X7R tipo kondensatorių, kurie naudojami didelės galios BMR antenos maitinimo įtaisų filtruose, tyrimai. Šių tyrimų tikslas – surasti būdus sumažinti galios nuostolius šiuose prietaisuose. Buvo ištirta kaip kondensatoriaus nuoseklioji ekvivalentinė varža (NEV) priklauso nuo pastoviosios įtampos prijungtos prie šio kondensatoriaus (V_{DC}), kai ši įtampa kito nuo 0 V iki 100 V, o kondensatoriaus veikimo dažnio diapazonas buvo iki 0,1 MHz.Tyrimų aparatūros blokinė schema pavaizduota S4.1 paveiksle.

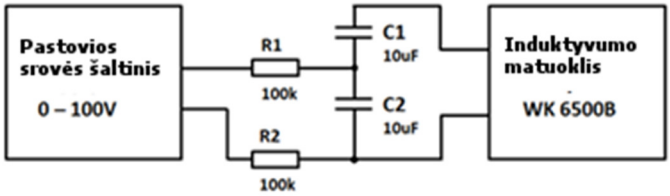

S.4.1 pav. X7R kondensatorių impedanso tyrimo aparatūros blokinė schema

Aparatūrą sudaro pastovios (iki 100V) įtampos šaltinis, elektrinė schema su tiriamais kondensatoriais (*C*1 ir *C*2) ir kondensatorių impedanso matuoklis (WK 6500B).

Tyrimams buvo panaudoti daugiasluoksniai X7R (CKG57NX7R2A106M500JH) tipo keraminiai kondensatoriai, kurių talpa buvo 10 µF, o NEV 3.4 mΩ, esant 100 kHz dažniui. Maksimali pastovi įtampa – 100 V. Šie kondensatoriai buvo pasirinkti dėl to, kad jie yra plačiai naudojami BMR siųstuvų keitikliuose.

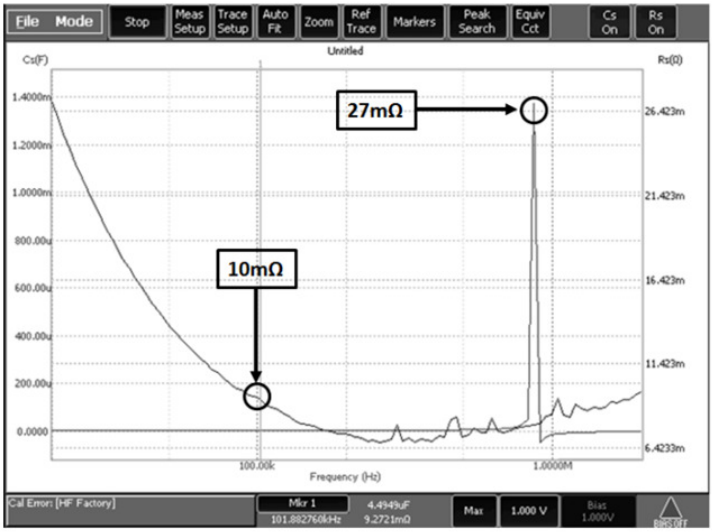

S.4.2 pav. X7R (CKG57NX7R2A106M500JH) kondensatoriaus nuosekliosios ekvivalentinės varžos (NEV) priklausomybė nuo dažnio, kai $V_{DC} = 0$

Tipiška šiems kondensatoriams NEV priklausomybė nuo dažnio, kai $V_{DC} = 0$, parodyta S4.2 paveiksle. Kaip matyti iš šio paveikslo, NEV spektrui šiuo atveju yra būdinga tik viena smailė atitinkanti 27 mΩ vertės NEV.

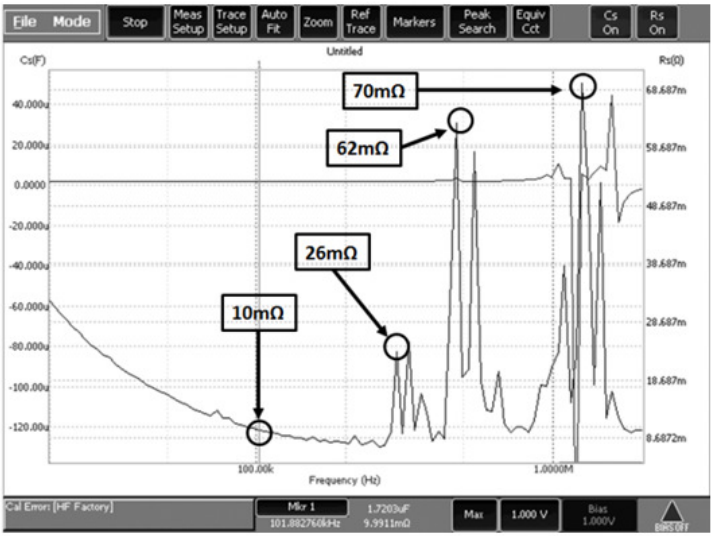

S.4.3 pav. X7R (CKG57NX7R2A106M500JH) kondensatoriaus nuosekliosios ekvivalentinės varžos (NEV) priklausomybė nuo dažnio, kai V_{DC}=50 V

Paveikus kondensatorius pastovia įtampa, jų talpa ženkliai pasikeitė. Tai pasireiškė papildomų smailių atsiradimu NEV spektre (žr. 6S pav.). Kai V_{DC} = 50 V, šiame spektre atsiranda smailės, atitinkančios 316 kHz, 398 kHz, 465 kHz ir 1 MHz dažnį. NEV, išmatuotos esant 465 kH dažniui, vertė padidėjo nuo 8 mΩ, kai V_{DC} = 0 V, iki 24 mΩ, kai V_{DC} = 20 V, iki 62 mΩ, kai V_{DC} = 50 V, ir iki 126 mΩ, kai V_{DC} = 90 V.

Buvo padaryta išvada, kad tokie plačiai naudojami X7R kondensatoriai elgiasi kaip pjezoelektriniai rezonatoriai, jeigu yra paveikiami pastovios įtampos. Toks mechaninis rezonansas padidina šių kondensatorių galios nuostolius ir jų gedimo tikimybę. Todėl rekomenduojama BMR antenos maitinimo sistemos filtruose naudoti kondensatorių baterijas, sudarytas iš tokios pačios talpos kondensatorių.

5. Branduolinio magnetinio rezonanso siųstuvas neturintis aukštesniųjų harmonikų

Šiame skyriuje aprašoma nauja BMR antenos siųstuvo konstrukcija, veikianti esant 175 °C aplinkos temperatūrai. Jis sudarytas iš kelių modulių, kurie sujungia kelis vienodos galios modulių „meandro“ formos signalus. Tai leidžia generuoti signalą artimą sinusiniam, t.y. su mažu papildomų harmonikų kiekiu ir realizuoti efektyvų amplitudės valdymą. Tai pasiekiama, sukuriant pastovų fazių postūmį tarp modulių. Amplitudės valdymas buvo pasiektas, naudojant Chireix-Doherty moduliacijos principą. Parodyta,

jog palyginti su dviejų modulių siųstuvu, tokiame daugelio modulių BMR siųstuve iki 20 % padidėja signalo-triukšmo santykis (STS) ir padidėja įtaiso tarnavimo trukmė.

Skyrių sudaro penki poskyriai ir išvados. Pirmajame nagrinėjama daugelio modulių BMR siųstuvo topologija. Jo blokinė schema pavaizduota S5.1 paveiksle. Ji sudaryta iš kelių siųstuvų: elementaraus siųstuvo (A tipas) turinčio tik 2 keitiklius (modulius), B tipo, turinčio 4 modulius ir C tipo su 8 moduliais. Nors daugelio modulių BMR siųstuvas gali turėti *n* modulių, šioje disertacijoje buvo nagrinėjami tik A, B, ir C tipo siųstuvai, nes siųstuvai su didesniu kiekiu modulių ženkliai nepagerina aukštesniųjų harmonikų panaikinimo efekto.

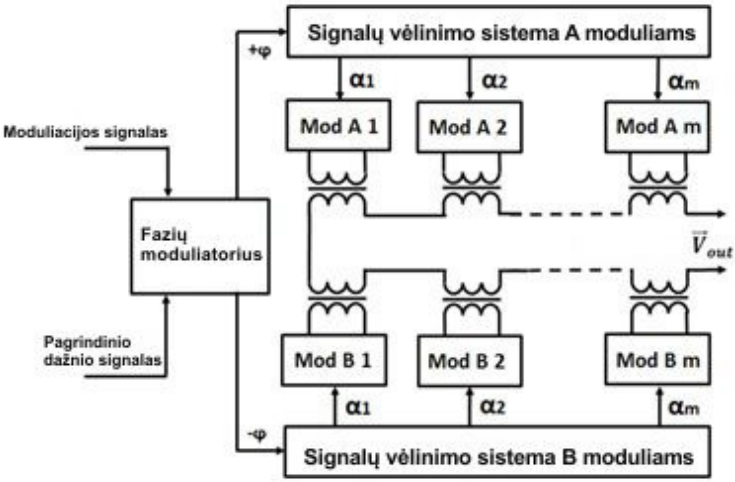

S.5.1 pav. Daugelio modulių BMR siųstuvo blokinė schema

Daugelio modulių siųstuvo, kurio išėjime nėra aukštesniųjų harmonikų, veikimas yra paremtas atskirų A tipo siųstuvų išėjimo signalų sinchronizavimu, naudojant daugelio pakopų uždelsimo sistemą. Šios sistemos veikimo algoritmas siųstuvui, kurio išėjime nėra 7-tos harmonikos, pateiktas S5.2 paveiksle. A tipo siųstuvo fazė $\varphi = 0°$, todėl jo išėjime yra visos harmonikos, B tipo siųstuvo fazė $\varphi = \pi/3°$ ir todėl šio siųstuvo išėjime nėra 3-osios harmonikos. C tipo siųstuvo topologija yra tokia, kad 3-asis elementarusis siųstuvas turi $\varphi = \pi/5°$ fazę, o 4-ojo fazė atžvilgiu 3-ojo yra $\varphi = \pi/3°$. Todėl C tipo siųstuvo išėjime nėra 3-osios ir 5-osios harmonikos.

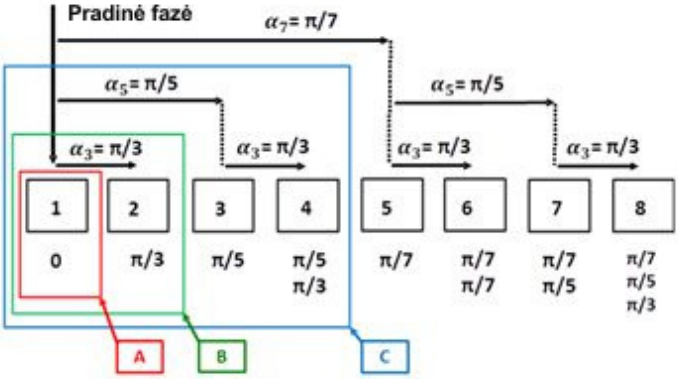

S.5.2 pav. Fazių postūmio algoritmas 3-čios, 5-tos ir 7-tos harmonikos panaikinimui

Antrajame poskyryje aprašomi A, B, ir C tipo BMR siųstuvų išėjimo signalo harmonikų spektrai. Siųstuvų išėjimų srovė buvo modeliuojama. 3S lentelė rodo, sparčiosios Furjė transformacijos analizės būdu (*LTSpice* programa) gautų, pirmųjų trijų svarbiausių aukštųjų harmonikų (3-ios, 5-os ir 7-os) efektinės srovės vertės.

S.5.1 lentelė. A, B ir C tipo siųstuvų srovės harmonikos ir MOSFET tranzistoriuose išsiskirianti galia

Harmonikos	1-moji	3-čioji	5-toji	7-toji	Visos
A tipas, 2 moduliai					
Harmonikos srovės efektyvioji vertė, A	4,39	14,67	2,34	1,44	18,68
2 modulių galia, W	0,39	4,30	0,11	0,04	6,98
B tipas, 4 moduliai					
Harmonikos srovės efektyvioji vertė, A	2,50	0,19	1,28	0,82	4,60
4 modulių galia, W	0,50	0,00	0,13	0,05	1,67
C tipas, 8 moduliai					
Harmonikos srovės efektyvioji vertė, A	1,50	0,06	0,08	0,34	2,19
8 modulių galia, W	0,72	0,00	0,00	0,04	1,53

Kaip matyti iš S5.1 lentelės, galios sklaida nuo 6,98 W A tipo siųstuvo atveju sumažėjo iki 1,69 W B tipo siųstuvui ir iki 1,53 W C tipui, kuriame buvo pašalinta 3-ji ir 5-ji harmonikos.

Trečiajame poskyryje parodyta kaip aukštesniųjų harmonikų panaikinimas sumažina vieno impulso metu iš talpuminio energijos šaltinio sunaudotą energiją (S5.2 lentelė). Tai leidžia padidinti impulsų skaičių matavimo impulsų serijoje, dėl ko padidėja signal-triukšmo santykis (STS).

S.5.2 lentelė. STS ir matavimo impulsų kiekis skirtingiems siųstuvų tipams

Antenos kokybė Q=10	A-tipas	B-tipas	C-tipas
Energija suteikiama antenai vieno impulso metu	0,633	0,600	0,596
Energija sunaudojama iš šaltinio vieno impulso metu	0,690	0,637	0,627
Sugeneruotų impulsų skaičius	116	126	128
STS A-tipo siųstuvo atžvilgiu, %	100	104	105
Antenos kokybė Q=30			
Energija suteikiama antenai vieno impulso metu	0,220	0,212	0,209
Energija sunaudojama iš šaltinio vieno impulso metu	0,259	0,227	0,220
Sugeneruotų impulsų skaičius	309	353	363
STS A-tipo siųstuvo atžvilgiu, %	100	107	108
Antenos kokybė Q=100			
Energija suteikiama antenai vieno impulso metu	0,067	0,065	0,064
Energija sunaudojama iš šaltinio vieno impulso metu	0,104	0,077	0,072
Sugeneruotų impulsų skaičius	768	1046	1105
STS A-tipo siųstuvo atžvilgiu,%	100	117	120

Ketvirtame poskyryje nagrinėjama kaip aukštesniųjų harmonikų panaikinimas BMR siųstuvo išėjime padidina šio įtaiso darbo resursą. Skaitmeninio modeliavimo rezultatai parodė, kad aukštesniųjų harmonikų panaikinimas gerokai sumažina srovės, tekančios per filtro (X7R tipo) kondensatorių, vertę. S5.3 lentelė rodo kaip pasikeičia rezonansiniai galios nuostoliai BMR siųstuvo filtro kondensatoriuje A ir B tipo siųstuvuose. Kaip matyti iš šios lentelės, patikimam filtro kondensatoriaus darbui, A tipo siųstuvo atveju reikia, kad filras būtų pagamintas iš 3-jų X7R kondensatorių sujungtų lygigrečiai, tačiau B tipo atveju užtenka 2-jų tokių kondensatorių. Aukštesniųjų harmonikų panaikinimas leidžia sumažinti ir kondensatorių skaičių filter, dėl to sumažėja BMR siųstuvo matmenys.

Taip pat šiame poskyryje pateikiami daugelio modulių BMR siųstuvo DC/AC keitiklių veikimo resurso tyrimai. Atlikti skaičiavimai parodantys kokia galia išsiskiria IPW90R120 tipo MOSFET tranzistoriuose A, B, ir C tipo siųstuvų atveju, kai aplinkos temperatūra lygi 175 °C. Įvertintas šių tranzistorių temperatūros padidėjimas (ΔT_j), kuris panaudotas DC/AC keitiklių veikimo resurso trukmės (t_{v1}) įvertinimui. Parodyta, jog t_{v1} išauga nuo 4 metų iki 9,2 metų, kai siųstuvo topologija kinta nuo A iki C tipo.

Penktajame poskyryje pateikiami daugelio modulių siųstuvo eksperimentinio išbandymo rezultatai panaudotojus įtaisą, kurio schema parodyta S5.3 paveiksle.

S5.3 Lentelė. Rezonansiniai galios nuostoliai BMR siųstuvo filtro kondensatoriuje A ir B tipo siųstuvuose

Nr.	Parametras	A-tipas	B-tipas
1	Srovė tekanti per filtrą (A), kai impulso trukmė 100 μs,	28,5	17,8
2	Energija (mJ), išsiskirianti ne rezonanso atveju, kai kondensatoriaus ekvivalentinė nuoseklioji varža R_0=50 mΩ	13,37	5,37
3	Energija (mJ), išsiskirianti rezonanso atveju, kai kondensatoriaus ekvivalentinė nuoseklioji varža $8R_0$	106,96	42,96
4	Energija (mJ), išsiskirianti kai filtro kondensatorių schemą sudaro 3 kondensatoriai	11,98	4,77
5	Energija (mJ), išsiskirianti kai filtro kondensatorių schemą sudaro 2 kondensatoriai	26,74	10,74

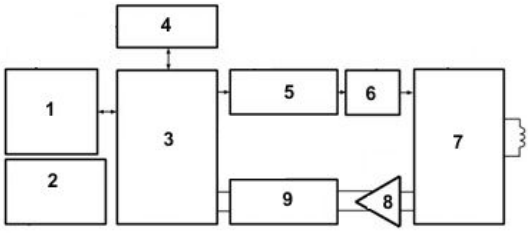

S.5.3 pav. BMR siųstuvo bandymo aparatūros blokinė schema ir signalų perdavimo keliai. 1 – RAM, 2 – pastovios įtampos šaltinis ir kondensatorių baterija, 3 – procesorius, 4 – aparatinė sąsaja, 5 – BMR siųstuvas, 6 – filtras, 7 – BMR antena ir jos sąsaja, 8 –žemo triukšmo signalų stiprintuvas, 9 – imtuvas

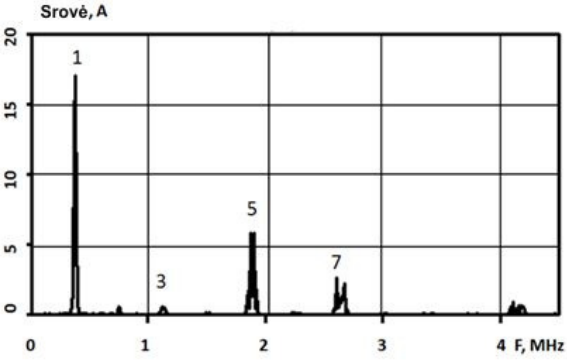

S.5.4 pav. B-tipo topologijos BMR siųstuvo išėjimo srovės spektras

S5.4 paveiksle pateikti šių bandymų rezultatai, rodantys jog daugelio modulių BMR siųstuvo išėjime yra ženkliai (iki 96%) sumažinta 3-sios harmonikos įtaka.

Bendrosios išvados

Remiantis literatūros apžvalga buvo padarytos šios pagrindinės išvados:

1. Skirtingi tiriamų gręžinio skysčių dielektriniai parametrai sukelia BMR antenos rezonansinio dažnio poslinkį. Todėl siekiant sumažinti šio dažnio pokytį, reikia panaudoti papildomą pakankamai sudėtingą rezonansinio dažnio paderinimo sistemą. Dėl to BMR įtaisas padidėja, jo kaina išauga bei sumažėja įtaiso patikimumas. Dėl šios priežasties reikia ištirti galimybes sukurti naują BMR anteną, kurioje šie trūkumai būtų pašalinti.
2. BMR siųstuvo išėjimo srovėje aukštosios harmonikos išskiria papildomus galios nuostolius, o tai padidina BMR siųstuvo temperatūrą ir sumažina įtaiso patikimumą. Todėl tikslinga sukurti tokią siųstuvo topologiją, kuri leistų panaikinti arba bent jau ženkliai sumažintų aukštesniųjų harmonikų dalį siųstuvo išėjimo įtampoje.
3. Aukštos įtampos MOSFET tranzistoriai, naudojami BMR siųstuve, privalo veikti plačiame temperatūrų (T) intervale, kuris yra didesnis negu leidžiamas pagal šių tranzistorių gamintojų standartus. MOSFET santakos-ištakos varža (R_{dson}), kuri apsprendžia energijos nuostolius tranzistoriuje, turi būti tirta aukštose (iki +200 °C) temperatūrose. Tokie tyrimai pasitarnautų R_{dson} nuo T ir santakos-ištakos srovės (I_d) priklausomybės aukštose temperatūrose nustatymui.
4. Pastaruoju metu buvo intensyviai tiriami procesų, iššaukiančių keramikos kondensatorių gedimus dėl elektrinių laukų poveikio, mechanizmai. X7R tipo keramikos kondensatorių, plačiai naudojamų BMR įtaisų filtruose, gedimai reikalauja papildomų tyrimų, tokių kaip kondensatorių savybių pokytis, paveikus juos pastovia elektrine įtampa.

Apibendrinant tyrimų rezultatus buvo padarytos šios išvados:

1. Disertacijoje buvo pasiūlyta nauja BMR antenos konstrukcija su papildomu Faradėjaus ekranu. Tai leido (iki 1 %) sumažinti BMR antenos rezonansinio dažnio kitimą, kintant giluminiame gręžinyje aptinkamų medžiagų (skysčių) elektriniams parametrams. Tai sudarė sąlygas atlikti matavimus, nenaudojant specialios antenos derinimo sistemos, ir sukurti pirmą komercinį gręžinio skysčių BMR analizatorių, veikantį realiame laike (*in-situ*).
2. Nauji eksperimentiniai duomenys buvo gauti, tiriant silicio MOSFET tranzistorių santakos-ištakos varžos (R_{dson}) savybes aukštose (iki 200 °C) temperatūrose. Šis tyrimas parodė, kad R_{dson} priklausomybė nuo temperatūros yra netiesinė ir R_{dson} vertė, priklausomai nuo santakos-ištakos srovės I_d, gali būti 3–5 kartus didesnė už tą, kuri teka, kai MOSFET tranzistoriaus temperatūra yra 25 °C. Pasiūlyta nauja empyrinė formulė, aprašanti R_{dson} priklausomybę nuo temperatūros, kurioje įskaityta ir I_d įtaka. Eksperimentiškai parodyta, jog ši

formulė gerai aprašo R_{dson} priklausomybes nuo T ir I_d silicio MOSFET tranzistoriams temperatūrų intervale nuo 25 °C iki 200 °C.

3. Nustatyta, jog plačiai naudojamų BMR siųstuvų filtruose keraminių X7R kondensatorių galios nuostoliai išauga, paveikus šiuos kondensatorius pastovia elektros įtampa. Tai yra išdava sustiprėjusio pjezoelektrinio efekto, kuris padidina X7R kondensatorių sugedimo tikimybę. Darbe pasiūlyta sumažinti jų perkaitimą, panaudojus schemą, sudarytą iš kelių lygiagrečiai sujungtų vienodų kondensatorių.
4. Tyrimai parodė, kad daugelio modulių BMR siųstuvas, kuris naudoja fiksuoto fazės poslinkio metodą sumažinti aukštesniųjų harmonikų įtaką siųstuvo sinusiniame išėjimo signale, leidžia iki 4 kartų sumažinti elektros energijos nuostolius, kai modulių skaičius padidėja nuo 2 iki 8.
5. Signalo-triukšmo santykis BMR įtaise, veikiančiame su tipiškos 80 J energijos talpuminiu šaltiniu, dėl aukštesniųjų harmonikų įtakos sumažėja B ir C tipo BMR siųstuvų atveju atitinkamai iki 17 % ir 20 %, lyginant su signalo-triukšmo santykiu A tipo siųstuve.
6. Aukštesniųjų harmonikų BMR siųstuve, kurių MOSFET tranzistorių šiluminė varža R_{th} = 0,5 K/W, panaikinimas sumažina MOSFET tranzistorių temperatūros padidėjimą ΔT_j nuo 38 °C iki 20 °C ir padidina įtaiso resursą nuo 4 metų iki 9,2 metų.
7. Trečiosios harmonikos panaikinimo poveikis daugelio modulių BMR siųstuve buvo patvirtintas eksperimentiškai. Buvo gauta, kad 3-osios harmonikos amplitudė sumažėja 96 % B tipo siųstuve lyginant su A tipo siųstuvu.

Annexes[1]

Annex A. Agreement of co-authors to provide published material in the doctoral disertation
Annex B. Copies of scientific publications by the autor on the topic of the dissertation.

[1] The annexes are supplied in the enclosed compact disk.

Alexey A TYSHKO

DEVELOPMENT OF NUCLEAR MAGNETIC RESONANCE DOWNHOLE LOGGING TOOLS FOR HYDROCARBONES SEARCH

Doctoral Dissertation

Technological Sciences,
Electrical and Electronics Engineering (01T)

Alexey A TYSHKO

BRANDUOLINIO MAGNETINIO REZONANSO ĮTAISO ANGLIAVANDENILIŲ ŽVALGAI GILUMINIUOSE GRĘŽINIUOSE KŪRIMAS

Daktaro disertacija

Technologijos mokslai,
Elektros ir elektronikos inžinerija (01T)

2016 12 23. 11,0 sp. l. Tiražas 20 egz.
Vilniaus Gedimino technikos universiteto
leidykla „Technika“,
Saulėtekio al. 11, 10223 Vilnius,
http://leidykla.vgtu.lt
Spausdino BĮ UAB „Baltijos kopija“,
Kareivių g. 13B, 09109 Vilnius